

Low-noise GaAs Quantum Dots

Inauguraldissertation

zur
Erlangung der Würde eines Doktors der Philosophie
vorgelegt der
Philosophisch-Naturwissenschaftlichen Fakultät
der Universität Basel

von

Liang Zhai

Basel, 2022

Originaldokument gespeichert auf dem Dokumentenserver der Universität Basel
<http://edoc.unibas.ch>



This work is licensed under a Creative Commons Attribution-NonCommercial-NoDerivatives 4.0 International License.

The complete text may be reviewed here:

<http://creativecommons.org/licenses/by-nc-nd/4.0/>

Genehmigt von der Philosophisch-Naturwissenschaftlichen Fakultät

auf Antrag von

Prof. Dr. Richard J. Warburton

Prof. Dr. Philipp Treutlein

Prof. Dr. Chaoyang Lu

Basel, den 16. November 2021

Prof. Dr. Marcel Mayor
Dekan



Creative Commons License Deed

Attribution-NonCommercial-NoDerivatives 4.0 International

This is a human-readable summary of (and not a substitute for) the license.

You are free to:



Share — copy and redistribute the material in any medium or format

The licensor cannot revoke these freedoms as long as you follow the license terms.

Under the following terms:



Attribution — You must give appropriate credit, provide a link to the license, and indicate if changes were made. You may do so in any reasonable manner, but not in any way that suggests the licensor endorses you or your use.



NonCommercial — You may not use the material for commercial purposes.



NoDerivatives — If you remix, transform, or build upon the material, you may not distribute the modified material.

No additional restrictions — You may not apply legal terms or technological measures that legally restrict others from doing anything the license permits.

Notices:

You do not have to comply with the license for elements of the material in the public domain or where your use is permitted by an applicable exception or limitation.

No warranties are given. The license may not give you all of the permissions necessary for your intended use. For example, other rights such as publicity, privacy, or moral rights may limit how you use the material.

Preface

Self-assembled quantum dots have been an active field of study in semiconductor physics for more than three decades. Amid the rising of photonic quantum technologies, a strong drive of the field is the promising potential of quantum dots as practical single-photon sources. Among different types of self-assembled quantum dots, InGaAs quantum dots have been the system of largest prevalence. In the past decade, there have been growing interests in GaAs quantum dots, a relatively new system compared to their InGaAs counterpart. The main advantages of the GaAs quantum dots are: first, a convenient emission wavelength; second, removal of the growth-induced strain. In this thesis, we focus on improving the optical properties of GaAs quantum dots. GaAs quantum dots in the bulk usually suffer from noise in the semiconductor environment. Here, low level of noise has been achieved with the help of an *n-i-p* diode structure. From the low-noise GaAs quantum dots, we create high-quality single-photons – fast, pure and highly indistinguishable. We further demonstrate that the high-quality single-photons from separate GaAs quantum dots have a high degree of mutual indistinguishability – the photons emitted by different quantum dots are close to identical. Our studies pave the way to employing multiple GaAs quantum dots for complex photonic quantum applications.

This thesis is outlined as follows:

The first chapter serves as an introductory purpose. It introduces the development of self-assembled quantum dots. It compares two leading workhorses – InGaAs quantum dots and GaAs quantum dots – from their growth procedures to their perspectives for quantum technologies. It also introduces some relevant concepts which are being discussed in the following chapters.

In Chapter 2, we discuss a method to modify the quantum dot emission wavelength. A strain-amplification device is presented, which is capable of inducing large strain to a relatively thick semiconductor sample. With such a device, wavelength tuning of a

quantum dot is demonstrated over a range that is nearly three orders of magnitude larger than the emission linewidth. This wavelength tuning method maintains the narrow linewidth and single-photon nature of the quantum dot emission. It enables the tuning of GaAs quantum dot emission into resonance with rubidium quantum memory.

In Chapter 3, we tackle the noise issue in GaAs quantum dots. The relatively noisy environment, which leads to broad linewidth and blinking in the emission, strongly hinders GaAs quantum dots for practical applications. To reduce the noise, a novel *n-i-p* heterostructure is specially designed for GaAs quantum dots at cryogenic temperature. With the assist of the heterostructure the noise is suppressed: the quantum dot emission linewidth is very close to the lifetime limit; blinking in the emission is removed. The electron spin properties are also studied in GaAs quantum dots. The electron spin of the low-noise GaAs dots has a relatively long lifetime – a prerequisite for single-spin experiments.

In Chapter 4, we focus on the radiative Auger process in low-noise GaAs quantum dots. The radiative Auger process has been observed in the emission of quantum dots as red-shift photons under resonant excitation. The resonant transition and radiative Auger transition form a Λ -scheme. An observation of electromagnetically-induced transparency type dip in the Λ -scheme reveals that the radiative Auger process not only takes place in the emission but also is optically addressable.

In Chapter 5, we experimentally study the electron-nuclear spin interaction in low-noise GaAs quantum dots. The lineshape of a trion spectrum under one-laser resonant excitation (in a high magnetic field) resembles a typical Lorentzian shape. Such a Lorentzian lineshape infers that the noncollinear interaction between electron and nuclear spins are strongly suppressed. In a two-laser experiment, the electron-nuclear spin interaction leads to nuclear-spin polarisation in the recovery plateau of a negative trion. The nuclear spins affect the blue- and red-Zeeman transitions differently. On the blue-Zeeman branch, nuclear spins tend to lock the quantum dot into the coherent population trapping resonance. In contrast, on the red-Zeeman branch, the coherence population trapping resonance is avoided.

In Chapter 6, we focus on demonstrating the quantum interference of single-photons from low-noise GaAs quantum dots. First, the creation of highly pure and indistinguishable photons is achieved from a single GaAs quantum dots. A Hong-Ou-Mandel

interference visibility of 98% is demonstrated for long-delayed ($1 \mu\text{s}$) photons, the very first time for GaAs quantum dots. Second, we interface single-photons from two separate GaAs quantum dots on a symmetric beamsplitter: the mutual indistinguishability is close to unity. This near-unity two-photon interference visibility suggests that multiple GaAs quantum dots – not only one – can be used as single-photon sources in photonics quantum technologies. An optical controlled-not gate with two GaAs-quantum-dot single-photon sources is subsequently demonstrated. The successful operation of the controlled-not gate marks the first step towards employing low-noise GaAs quantum dots for practical applications.

Contents

Preface

1	Introduction	1
1.1	Self-assembled Quantum Dots in III-V semiconductors	1
1.1.1	Growth of Self-assembled Quantum Dots	1
1.1.2	GaAs Quantum Dots in AlGaAs	3
1.2	Radiative Auger process in Quantum Dots	5
1.3	Hyperfine Interactions with Nuclear Spins	6
2	Large-range Strain Tuning of GaAs Quantum Dots	9
2.1	Background	10
2.2	Sample Growth and Strain Amplification Device	11
2.3	Strain Tuning of GaAs Quantum Dots in a Bulky Sample	13
2.4	Narrow-Linewidth and Single-Photon Characteristics During Strain-Tuning	15
2.5	Summary	17
3	Low-Noise GaAs Quantum Dots in an $n-i-p$ Diode	18
3.1	Background	19
3.2	Sample Design and Characterisation	20
3.3	Resonance Fluorescence from GaAs QDs	22
3.4	Blinking-Free Single-Photon Emission	25
3.5	High-Fidelity Spin Initialisation	26
3.6	Summary	28
3.7	Methods	28
4	Driving the Radiative Auger Transition in GaAs Quantum Dots	38
4.1	Background	39
4.2	Inverting the Radiative Auger Process	41
4.3	Autler-Townes Splitting in Radiative Auger Emission	42
4.4	Driving Radiative Auger Transition in a Two-Colour Experiment	43
4.5	Summary	45

4.6	Methods	46
4.6.1	A three-level model for quantum optics simulations	46
4.6.2	Experimental techniques	48
4.6.3	Time-resolved correlation measurements	49
4.6.4	Magnetic Field Dispersion of the Emission	51
4.6.5	Further Measurements of Autler-Townes splitting	51
5	Nuclear-Spin Polarisation in Low-Noise GaAs Quantum Dots	53
5.1	Background	53
5.2	One-Colour Experiment: Suppressed Quadrupolar Interaction	54
5.3	Two-Colour Experiment: Dynamic Nuclear-Spin Polarisation	57
5.4	Nuclear-Spin Assisted Coherent Population Trapping	58
5.5	Summary	60
5.6	Methods	61
6	Quantum Interference of Identical Photons from Remote Quantum Dots	64
6.1	Background	65
6.2	Indistinguishable Photons from Single GaAs Quantum Dots	66
6.3	Two-Photon Interference from Distant Emitters	68
6.4	A Quantum Logical Gate Linking Remote Single-Photon Sources	71
6.5	Summary	73
6.6	Methods	74
7	Conclusions and Outlook	78
A	Details on	
	“Quantum Interference of Identical Photons from Remote Quantum Dots”	81
A.1	Heterostructure Design and Characterisation	81
A.2	Hong-Ou-Mandel Interference from Single GaAs Quantum Dots	83
A.3	Hong-Ou-Mandel Interference from Two Remote Quantum Dots	86
A.3.1	Theoretical Modelling of Two-QD HOM Visibility	90
A.3.2	Limitations on Two-QD HOM Visibilities	94
A.3.3	Effect of Temporal Post-Selection	97
A.3.4	Effect of Purcell Enhancement	98
A.4	Optical Controlled-Not Circuit with Remote-Quantum-Dot Photons	99
A.4.1	Alignment of Controlled-Not Setup	100
A.4.2	Operations of Controlled-Not Gate	101

A.5 Density Matrix Reconstruction of Bell State	102
---	-----

Acknowledgments	105
------------------------	------------

Chapter 1

Introduction

1.1 Self-assembled Quantum Dots in III-V semiconductors

Quantum dots (QDs) are semiconductor structures of nanometre in size, where the charge carriers experience quantum confinement in all three spatial dimensions. Due to the quantum confinement, QDs exhibit discrete energy levels, hence the term “artificial atoms”. Quantum dots can be fabricated by various methods: some are formed by colloidal synthesis¹ (e.g. colloidal core-shell QDs), some are defined by lithographically patterned gate electrodes², and some are grown using epitaxy methods³ such as molecular-beam epitaxy⁴ (MBE). The last type of QDs is usually referred to as self-assembled quantum dots.

In the course of this dissertation, we restrict ourselves to self-assembled QDs in III-V semiconductors.

1.1.1 Growth of Self-assembled Quantum Dots

The self-assembly of QDs emerged in the early 1990s. There are predominantly two bottom-up epitaxy methods for the self-assembly of III-V semiconductor QDs. The Stranski–Krastanov (SK) growth mode^{5,6} takes advantage of the strain during the deposition of a thin film on a lattice-mismatched substrate. As the growth continues beyond a certain thin-film thickness (usually called “wetting-layer”), three-dimensional (3D) islands (QDs) are formed so that the accumulated strain can be relaxed. The robustness and simplicity of SK growth led to its large prevalence. For example, InAs QDs grown on a GaAs matrix^{7–11} (InGaAs QDs) have benefited from almost three decades of developments. They have been a well-established platform for creating high-quality single-photons and for hosting single spins.

Techniques including droplet epitaxy^{12,13}(DE) and its recent evolution, local droplet etching^{14,15}(LDE), represent alternatives for the self-assembled QD growth. Both tech-

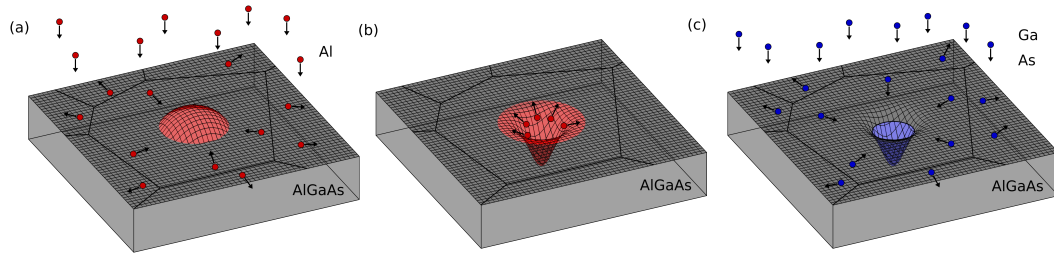


Fig. 1.1. **Illustration of the local droplet etching technique for GaAs QDs growth.** (a) The local droplet etching (LDE) technique is employed to grow GaAs QDs on an AlGaAs matrix. At first, aluminium is deposited at a reduced arsenic pressure. The aluminium forms nano-droplets on the AlGaAs matrix. (b) The matrix material beneath the nano-droplets is unstable in a group-V depleted ambience and subsequently evolves into nano-holes. The sample is annealed at a high temperature to facilitate the nano-hole etching. (c) Gallium and arsenic are deposited to fill the nano-holes. The filled nano-holes are capped with an additional AlGaAs barrier to form optically active QDs. The figures are adapted from Ref. 17. Details of the growth of an exemplary GaAs QD sample can be found in Chapter 2.2.

niques exploit the formation of metal nano-droplets (e.g. Al, Ga, etc) on a stable semiconductor surface. Compared to the SK growth mode (which relies on lattice-mismatched materials), the droplet methods offer the possibility for the QD self-assembly on materials with similar lattice constants (e.g. GaAs and AlGaAs). Thus, the droplet QDs can be made almost “strain-free”, leading usually to a better-controlled QD shape^{14–16}.

DE and LDE methods exploit the metal nano-droplets in different ways. The former crystallises the droplets in a group V atmosphere to form QDs. However, during the droplet crystallisation, the substrate temperature ($\sim 150 - 300^\circ\text{C}$) is lower compared to that in the SK techniques. This could lead to relatively poor materials and optical properties due to higher impurities. This problem is overcome in the LDE technique. In the LDE, the nano-droplets (e.g. Al, for the growth of GaAs QDs) initialise a local hole-drilling process beneath (local etching) in a group-V (e.g. As) depleted ambience and relatively high substrate temperatures; the nano-holes are filled with QD materials (e.g. Ga and As) and capped with barrier matrix (e.g. $\text{Al}_x\text{Ga}_{1-x}\text{As}$) to form optically active QDs. The LDE growth process for GaAs QDs is depicted in Fig. 1.1. In the following chapters, GaAs QDs on an $\text{Al}_x\text{Ga}_{1-x}\text{As}$ matrix (GaAs QDs) are all grown by the LDE technique.

1.1.2 GaAs Quantum Dots in AlGaAs

During the developments of self-assembled QDs, the most well-established platform in III-V semiconductors is arguably InGaAs QDs. InGaAs QDs are promising candidates as single-photon sources – a central building block for photonic quantum technologies. High-quality single-photons – fast, pure, and coherent – can be created by individual InGaAs QDs^{7,9,11,18}. The creation of single-photons can be deterministic, e.g. exploiting short resonant laser pulses. The QDs can be integrated in various nanophotonic structures, e.g. on-chip waveguides and photonic crystal cavities⁸, micropillars^{7,18} and tunable micro-cavities¹¹, allowing a high extraction efficiency of single-photons. These features enable the usage of QD single-photons in practical quantum photonics applications, such as boson sampling^{19,20}, and quantum key distribution^{21,22}. InGaAs QDs act also as hosts for single-spins. Single-spins can act as stationary qubits for quantum networks and quantum information processing. The electron and hole spins in InGaAs QDs have been initialised and manipulated with high fidelity^{3,23}. Techniques to determine and prolong spin coherence time are available^{24,25}. Spins can be entangled with the flying photons, a route to the creation of photonic cluster states²⁶. Interfacing photons from two separate QDs allows the entanglement of remote spins to be demonstrated²⁷. Furthermore, integrated photonics and phononics on InGaAs QDs platforms are studied in various nanostructures. Coupling the QDs to a waveguide or a cavity mode allows few-photon non-linearity^{8,28}, chiral light-matter interaction²⁹, and optomechanics^{30,31}, etc to be explored.

The GaAs QDs grown by LDE method only started to attract increasing attention a decade ago. However, they have already shown promising potential as non-classical light sources for both single-photons and entangled photon pairs. To generate entangled photon pairs, the biexciton cascade is involved. Decaying from the biexciton-state to the empty state, there are two relaxation paths: one path sees two photons emitted consecutively in H -polarisation; in the other path two V -polarisation photons are created. The two relaxation paths are similar, thus the which-path information could be erased and the emitted photon pairs are in a maximally entangled state, i.e. $|\Psi\rangle = (|HH\rangle + e^{iSt/\hbar}|VV\rangle)/\sqrt{2}$. The relative phase in the entanglement is determined by the fine-structure splitting \mathcal{S} . The smaller the fine-structure splitting \mathcal{S} , the higher the achievable entanglement fidelity. Compared to InGaAs QDs, GaAs QDs usually have a more symmetric shape, owing to the negligible lattice mismatch ($< 0.1\%$) between the dots and substrate materials. Therefore, the fine-structure splitting is typically smaller in GaAs QDs ($< 1 - 2$ GHz) than in InGaAs QDs. This motivates the developments of GaAs QDs for entangled-photon generation. Many efforts have been spent on improving

the QD symmetry during the growth processes^{15,16,32}. Post-growth techniques to reduce the effective fine-structure splitting (e.g. applying magnetic, electric or strain fields to QDs) have also been developed^{33,34}.

For single-photon creation, GaAs QDs benefit from the experience of InGaAs dots. Nano-engineering techniques are mostly transferable thanks to the similarity in materials. Experimental methods designed for InGaAs QDs can be mostly adopted to GaAs QDs as well. There are advantages of using GaAs QDs as single-photon sources in applications. First, GaAs QDs emit close to the red part of the spectrum, i.e. 750–800 nm. This wavelength range is precluded by the InGaAs QDs, whose emission band lies at near-infrared (900–1000 nm). The near-red wavelength is an important band: it coincides with the peak sensitivity of silicon detectors, facilitating efficient counting of the QD single-photons; it covers the D₁ and D₂ transitions of rubidium atoms, a stationary quantum memory system. The coverage of rubidium frequency opens up the perspective of storing QD single-photons in a stationary quantum memory³⁵, a step towards building a quantum node in the quantum network. Second, GaAs QDs are typically larger in size. The larger QDs size leads to a shorter radiative decay rate (typically 3-5 times shorter than InGaAs QDs). A shorter lifetime τ_r benefits the photon indistinguishability \mathcal{I} of individual emitters. At a short delay, the visibility of two-photon interference from a single emitter (which is defined as the indistinguishability \mathcal{I}) could be estimated^{9,36} by $\mathcal{I} = \frac{1}{\Delta_H} \cdot \frac{1}{2\tau_r}$. Here, $1/\Delta_H$ is the pure dephasing time characterising the homogeneous linewidth broadening. Assuming Δ_H is the same, faster radiative decay naturally leads to more coherent single-photons. The radiative decay can also be modified via Purcell enhancement by coupling the QDs into various nanophotonic structures.

Like InGaAs QDs, GaAs QDs also host single-spins. Only recently has the electron spin in GaAs QDs been initialised with high fidelity³⁷. The electron-spin properties in GaAs QDs are, therefore, still waiting to be explored. There are reasons to be optimistic. The electron spin in a QD interacts with a large number ($10^4 - 10^5$) of nuclear spins, which in turn add to the electron-spin's decoherence. In GaAs QDs, the nuclear spins are more homogeneous (all nuclei has a nuclear spin $I = 3/2$). There is no indium that poses a nuclear spin $I = 9/2$. Moreover, electron-spins in InGaAs QDs are affected by nuclear quadrupolar effects owing to their large built-in strain. In GaAs QDs, the build-in strain is negligible. Thus, the quadrupolar interaction is expected to be strongly suppressed. Both of these factors could infer a much longer electron spin coherence time in GaAs QDs.

1.2 Radiative Auger process in Quantum Dots

In this section, the radiative Auger process in the emission of a QD will be introduced. This is relevant to the experimental results in Chapter 4.

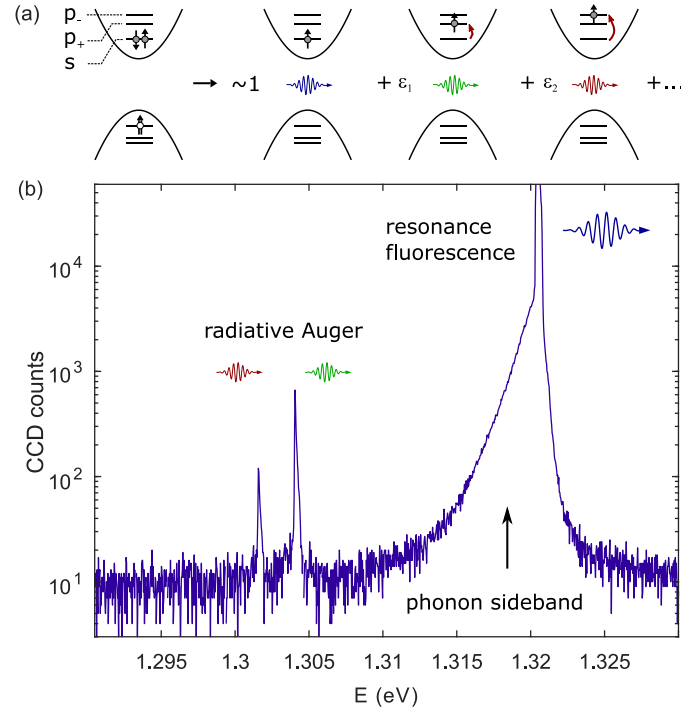


Fig. 1.2. **Illustration of the radiative Auger process from a negative trion.** (a) The relaxation paths of a negative trion. Most likely, the relaxation takes place together with a typical electron-hole recombination: a photon is created at the same frequency of the resonant laser. However, there exists also a small probability ϵ that the radiative Auger process takes place and the emitted photon is red-shifted. The corresponding energy is transferred to the remaining electron of the negative trion, causing the electron to be excited to a higher shell (e.g. p_- or p_+ shell). (b) Emission spectrum of a negative trion under resonant excitation (InGaAs QDs). The strong peak at $E = 1.321$ eV is the resonance fluorescence, which is surrounded by a broad acoustic phonon sideband. Red-shifted by ~ 18 meV there are two additional emission lines, stemming from the radiative Auger process. The figures are adapted from Ref. 38.

A negative trion (X^{1-}) in a QD consists of an electron-hole pair and an additional electron in the conduction band. In a negative trion, the relaxation process to the ground state typically means the electron-hole pair recombines and a photon is emitted; the additional electron in the conduction band remains unaffected. This process takes place in the resonance fluorescence. After being created by a resonant laser, the trion creates

a photon at the laser frequency and the additional electron remains in the conduction band s-shell. Besides the resonance fluorescence, there exists another photon-creating relaxation process – the radiative Auger process^{38,39}. In the radiative Auger process, the “additional” electron is excited from its initial state to a higher level (e.g. from the conduction band s-shell to p-shell). This excitation process takes away part of the energy (but only a small fraction) from the photon, leading to red-shifted emission. The resonance fluorescence and the radiative Auger processes are illustrated in Fig. 1.2(a).

An typical spectrum of the negative trion is presented in Fig. 1.2(b). Along with the resonance fluorescence emission peak, two additional peaks can be found at lower energy. These are the radiative Auger emission with the additional electron being promoted to the p-shells (the degeneracy of the p-shells are lifted due to the asymmetry of the QD). The separation between resonance fluorescence and radiative Auger emission corresponds to the single-particle splittings. These single-particle splittings are otherwise hard to access by optical means as particles are excited typically in pairs, as excitons³⁸. The intensity of the radiative Auger emission in GaAs QDs is typically 10-100 times weaker than the main resonance fluorescence emission.

1.3 Hyperfine Interactions with Nuclear Spins

In this section, hyperfine interactions between an electron-spin and nuclear spins will be briefly described. This information helps the understanding of Chapter 5.

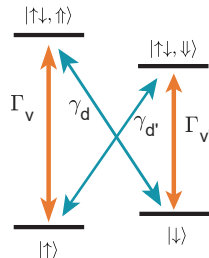


Fig. 1.3. **Level scheme of a negative trion in a magnetic field along the growth direction.** The orange arrows indicate the dipole-allowed vertical transitions. The blue arrows represent the diagonal transitions which are “forbidden” according to the selection rules for pure heavy-hole states.

In the conduction band, the s-shell electron-states are doubly degenerate, i.e. $|S, m_s\rangle = |1/2, \pm 1/2\rangle$ (denoted as $|\uparrow\rangle$ and $|\downarrow\rangle$). In the valance band, the heavy- and light-hole states have an total angular momentum of $J = 3/2$. For the heavy-hole states, the projected angular momentum in the growth direction is $j_z = \pm 3/2$, while for the light-hole states, it is $j_z = \pm 1/2$. We use $|\uparrow\rangle$ and $|\downarrow\rangle$ symbols for the holes. In a magnetic

field along the growth direction, the level diagram³ of a negative trion is shown in Fig. 1.3 (assuming a negative electron g -factor). The ground states $|\uparrow\rangle$ and $|\downarrow\rangle$ are split by the electron Zeeman energy; while the excited states $|\uparrow\downarrow, \uparrow\rangle$ $|\uparrow\downarrow, \downarrow\rangle$ are split by the hole Zeeman energy. Assuming the hole states have a pure heavy-hole character, only vertical transitions $\Gamma_{v(\prime)}$ are allowed according to the optical selection rules:

$$\begin{aligned} |\uparrow\rangle &\xleftrightarrow{\sigma^+} |\uparrow\downarrow, \uparrow\rangle, \\ |\downarrow\rangle &\xleftrightarrow{\sigma^-} |\uparrow\downarrow, \downarrow\rangle. \end{aligned}$$

Diagonal transitions are dipole-forbidden for pure heavy-hole states. In reality, the diagonal transitions characterised by rates $\gamma_{d(\prime)}$ can be (weakly) permitted through a heavy-light-hole admixture.

In QDs, hyperfine interactions of a conduction-band electron with nuclear spins are important for experiments involving optical electron-spin manipulation. The strength of hyperfine interactions is stronger in QDs than in the bulk, owing to the fact that the electron wave-function is strongly localised over $10^4 - 10^5$ nuclei – a number too small for efficient cancellation of the total nuclear spin by averaging⁴⁰. An electron spin \hat{S} interacts with nuclear spins \hat{I}^j (where j denotes the position \mathbf{r}_j) predominately by the Fermi-contact hyperfine interaction, which reads:

$$\hat{H}_{hf}^{fc} = v_0 \sum_{j=1}^N A^j |\psi(\mathbf{r}_j)|^2 \left(\hat{I}_z^j \hat{S}_z + \frac{1}{2} (\hat{I}_+^j \hat{S}_- + \hat{I}_-^j \hat{S}_+) \right), \quad (1.1)$$

with v_0 , $\psi(\mathbf{r}_j)$ denoting the unit cell volume and normalised electron envelope function, respectively. A^j is the isotope-specific constant of the hyperfine coupling coefficient. In a mean-field approach, the nuclear spins effectively create a magnetic field $B_n = v_0 \sum_j A^j |\psi(\mathbf{r}_j)|^2 \langle \hat{I}^j \rangle / g_e \mu_B$ which is experienced by the electron spin. This magnetic field is called the Overhauser field, which is usually related to a frequency shift, the Overhauser shift ω_{os} , via $\hbar\omega_{os} = g_e \mu_B B_n$. For fully polarised nuclei in GaAs, the maximum Overhauser field⁴⁰ corresponds to $\hbar\omega_{os}^{\max} = 135 \mu\text{eV}$. As indicated by the term $(\hat{I}_+^j \hat{S}_- + \hat{I}_-^j \hat{S}_+)$, the Fermi-contact interaction allows for spin transfer by a flip-flop process between an electron-spin and a nuclear-spin.

In a strained environment, e.g. InGaAs QDs, the strain induces a large electric field gradient which couples to the quadrupole moment of all nuclei. Such a coupling leads

to a quadrupolar interaction between an electron-spin and nuclear spins,

$$\hat{H}_Q = B_Q \left[\hat{I}_z^2 \cos^2 \theta - \frac{I(I+1)}{3} + (\hat{I}_z \hat{I}_x + \hat{I}_x \hat{I}_z) \sin \theta \cos \theta \right]. \quad (1.2)$$

Here, B_Q is an effective magnetic field representing the strength of the quadrupolar interaction, and θ is the angle between the quadrupolar axis tilted by strain and the growth axis. Assuming a small angle θ and a large nuclear Zeeman energy ($B_z^n > B_Q$), the term $\propto (\hat{I}_z \hat{I}_x + \hat{I}_x \hat{I}_z)$ in Eq. 1.2 can be rewritten by applying Schrieffer-Wolff (SW) transformation^{40,41}:

$$\hat{H}_{hf}^Q = \sum_{j=1}^N A_{nc}^j \hat{S} [\hat{I}_x^j \hat{I}_z^j + \hat{I}_z^j \hat{I}_x^j], \quad (1.3)$$

with $A_{nc}^j = A^j B_Q^j \sin(2\theta_j) / \omega_z^n$ being the noncollinear coupling constant. The effective hyperfine interaction Hamiltonian after the transformation reads $\hat{H}_{hf} = \hat{H}_{hf}^{fc} + \hat{H}_{hf}^Q$. The quadrupolar interaction \hat{H}_{hf}^Q allows a nuclear-spin flip without the need of flipping the electron-spin. It provides an explanation for bidirectional nuclear spin polarisation under resonant excitation in a high magnetic field, which leads to flat-top and triangle-shaped spectrum known as “dragging” and “anti-dragging”, respectively^{41,42}.

Chapter 2

Large-range Strain Tuning of GaAs Quantum Dots

This chapter is adapted from:

Liang Zhai, Matthias. C. Löbl, Jan-Philipp Jahn, Yongheng Huo, Philipp Treutlein, Oliver G. Schmidt, Armando Rastelli, and Richard J. Warburton,
Large-range frequency tuning of a narrow-linewidth quantum emitter,
Applied Physics Letters 117, 083106 (2020).

A hybrid system of a semiconductor quantum dot single-photon source and a rubidium quantum memory represents a promising architecture for photonic quantum repeaters. Realising such a hybrid system requires a match between the emission frequency of a quantum dot and the transition frequency of rubidium atoms. In this chapter, we demonstrate bidirectional frequency tuning of a narrow-linewidth (close-to-transform-limited) emission from a GaAs quantum dot. The frequency tuning is based on a piezoelectric strain-amplification device, which can apply significant stress to a thick bulky device. The induced strain shifts the emission frequency of the quantum dot over a total range of 1.15 THz, about three orders of magnitude larger than its spectral linewidth. Throughout the whole tuning process, both the spectral properties of the quantum dot and its single-photon emission characteristic are preserved. Our results show that external stress can be used as a promising tool for reversible frequency tuning of high-quality quantum dots. They pave the way towards the realisation of a quantum dot – rubidium atoms interface for future quantum networks.

2.1 Background

Semiconductor quantum dots (QDs) are promising sources of quantum light as they generate single-photons and entangled-photon pairs on demand with high purity and indistinguishability^{7,9,10,33,36,43–45}. To integrate the QD-based single-photon sources into long-distance photonic quantum networks, it is imperative that the single-photons all have the same frequency. This condition cannot be easily met in the growth processes – there is a spread of quantum dot size and composition leading to different emission frequencies^{17,46}. Instead, frequency tuning of individual quantum dots is required. GaAs QDs^{32,36,37,47–49} emit near the red part of the spectrum, covering the frequencies of rubidium D₁ and D₂ lines^{37,48,50}. Thanks to the convenient emission range, a hybrid system^{35,51,52}, GaAs QDs as single-photon sources and Rb-ensembles as memory elements, can be conceived. Implementing such a hybrid system hinges on both QD frequency tuning and narrow QD linewidths⁵².

Different methods have been developed for the frequency tuning of QDs. Applying an electric field to a QD integrated in a diode structure can adjust its emission frequency via the quantum confined Stark effect^{8,37,53}. Despite many successful implements on the InGaAs QD platform^{9,53,54}, this charge tuning method is much less investigated on GaAs QDs^{37,55,56}. Furthermore, the tuning range of the Stark effect is limited when the QD is in tunnel contact with a metallic gate (Coulomb blockade regime). For InGaAs QDs, below 0.15 THz range³ are typically achieved; for GaAs QDs, the largest tuning reported so far is ~ 0.24 THz³⁷. Another approach is to shift the emission frequency by applying an external stress^{33,57–61}. The original method⁵⁷ applies stress by bonding a bulk sample (of hundreds of microns in thickness) to a piezo-stack to which a voltage is applied at low temperature. In this method, the application of stress does not introduce additional noise, for instance, charge noise in the semiconductor, and the narrow QD linewidths of the starting material are preserved. However, the tuning range is rather small ($\simeq 0.1$ THz^{48,57}).

Much larger tuning ranges (up to 20 THz⁶²) have been achieved on QDs in nano-membranes^{58,63,64} (~ 100 nm in thickness), or in other nanostructures⁶⁵ such as nanowires⁶⁶. However, the nano-membranes tend to have a higher level of charge noise than the starting bulk material, and therefore QDs with broader linewidths. While successively emitted photons may demonstrate high levels of indistinguishability⁴⁴, the coherence of the photons decreases as the temporal separation between photons increases^{67,68}. Suppressing noise in QDs' charge environments is thus critical. Recent progress has been made to reduce the noise of QD environments in nano-membranes – narrow spectral

linewidths were achieved for InGaAs QDs^{8,69}. Suppressing the noise in semiconductors relies on a working *n-i-p* diode hosting the QDs at cryogenic temperatures⁷⁰. Such a diode structure has been demonstrated for GaAs QDs as well, but so far only in the bulk^{36,37,71}. This complicates the strain tuning criteria for the current device: large-range strain tuning is required for the bulk sample. For GaAs QDs, the spectral width of the QD ensemble is typically 5 – 10 THz; after careful calibration of the growth, it can be controlled to less than 1 THz³². In a photon memory application, it is desirable to bring a significant fraction of the QDs into resonance with the ⁸⁷Rb D₁ or D₂ line^{17,50,52}. Therefore, a strain tuning range of about 1 – 2 THz is needed while meeting the constraint that applying the stress should not introduce any additional noise.

In this chapter, we present a device that allows strain tuning of a GaAs QD in a 100 μm -thick wafer. We show reversible tuning of the QD's emission frequency over a range of 1.15 THz – about a thousand times more than its linewidth (1.26 GHz). The emission linewidth is close to the transform limit (0.97 GHz) and remains at this low level on inducing the large external strain. This frequency tuning is demonstrated on several QDs. Additionally, we prove that the QD is a good single-photon emitter throughout the entire tuning range.

2.2 Sample Growth and Strain Amplification Device

The sample contains GaAs QD grown by molecular-beam epitaxy using the local droplet etching method⁷². The growth procedure is detailed as follows. First, a 120 nm-thick Al_{0.4}Ga_{0.6}As barrier layer is grown on the standard GaAs (100) wafer. On this barrier layer, 0.5 monolayer (ML) of aluminium is deposited at a growth rate of 0.5 ML/s. The Al atoms migrate and form Al droplets on the Al_{0.4}Ga_{0.6}As surface. The substrate material beneath an Al droplet is unstable, initialising nano-hole formation⁷³. To facilitate this process, the sample is annealed at 600 °C in an arsenic-depleted ambience. Subsequently, a 2 nm-thick GaAs layer is deposited at a rate of 0.1 ML/s. During a two-minute annealing step, diffusion into the nano-holes takes place. The filled nano-holes are finally capped with another thick Al_{0.4}Ga_{0.6}As barrier to form optically active QDs.

In order to induce strain into the sample, we employ a home-built strain-amplification device following the design of Hicks *et al.*⁷⁴. It is composed of three conventional lead zirconate titanate (PZT) piezoelectric stacks (Piezomechanik GmbH, PSt150 cryo I). The device [see Fig. 2.1(a)] has a footprint of 24 mm \times 24.5 mm, well-matched to the size of attocube's low-temperature nano-positioners. The PZT stacks have equal lengths (L) of 9 mm and are firmly glued onto a C-shaped titanium holder. The holder itself is

fixed to the nano-positioners. The other ends of the PZT stacks connect to two movable titanium blocks, which are separated by a gap $d = 0.5$ mm. The sample straddles this gap: it is glued firmly in place. Upon applying a positive (negative) voltage, the central PZT stack extends (contracts) while the outer ones contract (extend), applying a compressive (tensile) stress to the sample. By making the cross-sectional area of the central PZT stack ($7 \text{ mm} \times 7 \text{ mm}$) twice as large as the outer ones ($5 \text{ mm} \times 5 \text{ mm}$), the force applied to the sample is balanced and therefore the sample displacement in its centre is minimised. The parallel arrangement of PZT stacks also minimises the strain induced by the cool-down process⁷⁴: when no piezo-voltage is applied, the QDs remain strain-free at cryogenic temperatures. Owing to the fact that the PZT stacks are longer than the width of the gap, QDs in the gap region experience an amplified effective strain⁶². Assuming the sample stiffness to be much smaller than that of the PZT stacks, we expect, in the ideal case, $\epsilon_{\text{eff}} = (2L/d) \epsilon_{\text{PZT}}$, with ϵ_{eff} and ϵ_{PZT} denoting the effective strain in the GaAs located above the gap, and the strain of the PZT stacks, respectively. In this ideal limit, the amplification factor is $2L/d = 36$. At a voltage of +150 V, the unloaded PZT stack achieves $\epsilon_{\text{PZT}} = -1.20 \times 10^{-3}$ at 300 K. Reducing by a factor⁵⁷ of ~ 20 at 4 K, the device ideally achieves $\epsilon_{\text{eff}} \simeq -2.17 \times 10^{-3}$ at 4 K on applying +150 V.

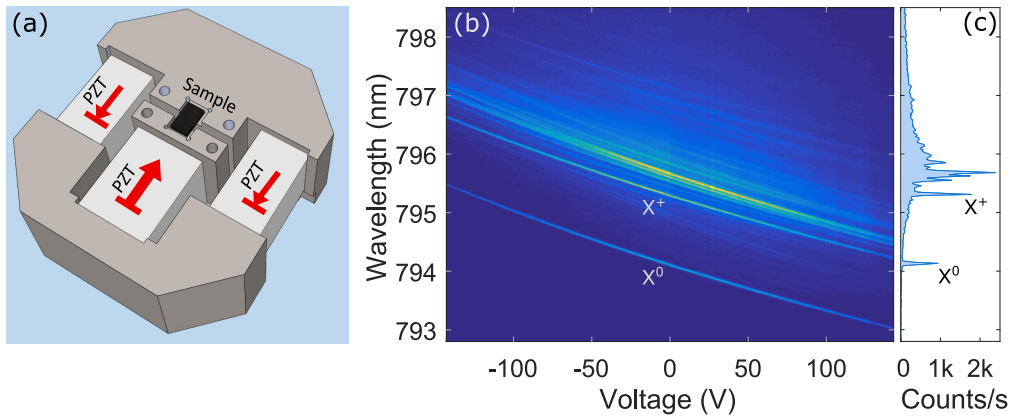


Fig. 2.1. **A strain-amplification device for bulky samples.** (a) A sketch of the strain-amplification device. Three PZT piezoelectric stacks are mounted in parallel on a C-shaped titanium holder. The sample is glued over a narrow gap separating two movable blocks. (b) Photoluminescence (PL) from a QD around the rubidium-87 D_1 line (794.98 nm). The QD can be tuned bidirectionally as a function of the voltage applied to the PZT stacks. (c) A PL spectrum of the GaAs QD at zero applied stress.

2.3 Strain Tuning of GaAs Quantum Dots in a Bulky Sample

We carry out photoluminescence and resonance fluorescence measurements on individual GaAs QDs with a confocal dark-field microscope⁷⁵. The strain-amplification device is housed in a liquid helium cryostat and cooled down to 4.2 K. Helium gas (25 mbar at room temperature) is used as a heat exchanger between the liquid helium and the strain-amplification device.

The photoluminescence measurements are performed under above-band excitation with a weak 632.8 nm He-Ne laser (intensity $\simeq 42$ nW/ μm^2). We look for QDs in the central region of the gap, where QDs experience larger strain. The QD emission is collected by an aspheric objective lens (numerical aperture NA = 0.71) and is sent to a spectrometer. A typical emission spectrum of a GaAs QD (bulk sample, without *n-i-p* diode structure) is depicted in Fig. 2.1(c), where we identify two characteristic narrow emission lines^{17,48}: the neutral exciton (X^0) and the positively charged trion (X^+). Using a combination of a low-noise voltage source (LNHR DAC, Basel Precision Instruments, ± 10 V output) and the amplification from an Attocube controller module (ANM 300, ~ 14.3 gain), we are able to apply voltages of up to ± 143 V to the PZT piezo-stacks. We record photoluminescence of the QD as a function of the external voltage (in the other words, external stress). As shown in Fig. 2.1(b), the X^0 and X^+ lines are red-shifted (blue-shifted) in parallel by around 1.38 nm (1.08 nm) when experiencing tension (compression).

Resonance fluorescence measurements are performed on the X^+ by scanning the frequency of a narrow-bandwidth continuous-wave (CW) laser across the QD resonance (intensity $\simeq 42$ nW/ μm^2). A very weak non-resonant laser ($\lambda = 632.8$ nm, intensity < 0.8 nW/ μm^2) illuminates the QD constantly during the scan, helping to stabilise the charge environment^{48,76}. From a Lorentzian fit to the measured fluorescence intensity we determine the frequency and the linewidth of the X^+ emission [see Fig. 2.2(d)]. The resonance frequency of the QD can be tuned bidirectionally as a function of strain. By applying ± 143 V voltage to the piezo-stack, the X^+ frequency is shifted over a total range of $\Delta f = 1.15$ THz (4.8 meV) [see Fig. 2.2(a)]. This tuning is 20-times larger than with the aforementioned original method^{48,57}, in which the sample is glued directly onto a PZT piezo-stack. The amplification is about 60% of the ideal limit. With our device, it is possible to address the ^{87}Rb D₁ transition [orange dashed line in Fig. 2.2(a)] with a QD which is originally far off-resonance.

The tuning of the QD emission energy ΔE with strain ϵ can be calculated from the Pikus-Bir Hamiltonian⁷⁷. We assume that the valence state has pure heavy-hole

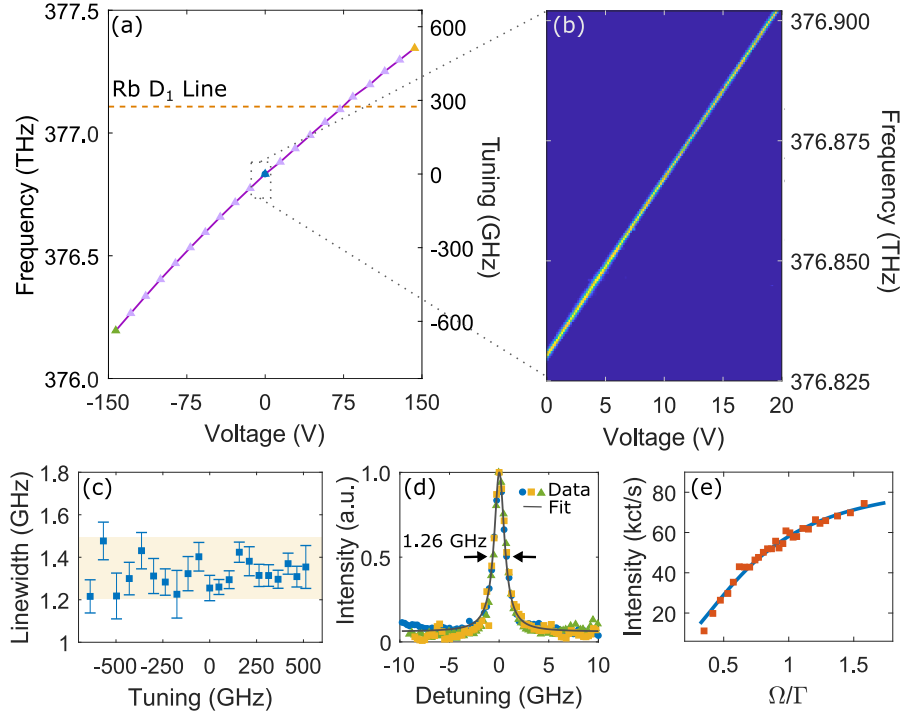


Fig. 2.2. **Strain Tuning of a GaAs QD across the ^{87}Rb D_1 line.** (a) Frequency of single QD resonance fluorescence as a function of the voltage applied to the PZT stacks (purple curve). The orange dashed line indicates the frequency of the ^{87}Rb D_1 line. (b) A zoomed-in plot of a selected area of (a). The QD emission stays bright and narrow independent of the externally induced strain. (c) The linewidth of QD emission as a function of the frequency-tuning with respect to the frequency at zero external stress. (d) Three different resonance fluorescence scans are plotted together in each case with normalised intensity. Blue, yellow and green symbols indicate the conditions where zero stress, maximum compression and maximum tension is applied to the QD, respectively [see (a)]. A Lorentzian curve (grey curve) provides a good fit to all three data sets. The full-width-at-half-maximum (FWHM) is 1.26 GHz. (e) Intensity of the resonance fluorescence (red squares) versus normalised Rabi frequency Ω/Γ . The blue curve is a fit modelled by a two-level system.

character and that the strain-dependence of the QD emission energy follows the strain-dependence of the GaAs band-gap. In a simple case where a stress is applied along the $[100]$ direction, $\Delta E = (a_c - a_v)\text{tr}(\epsilon) + \frac{b}{2}(2\epsilon_{zz} - \epsilon_{xx} - \epsilon_{yy})$. Here, a_c and a_v stand for the hydrostatic deformation potentials of the conduction band and valence band, respectively; b represents the shear deformation potential⁷⁷. For a uniaxial stress⁶², ϵ_{xx} , ϵ_{yy} , and ϵ_{zz} are connected through the Poisson effect: $\epsilon_{yy} = \epsilon_{zz} = -\nu\epsilon_{xx}$ (ν is the Poisson ratio). For GaAs, we have⁷⁸ $a_c = -7.17$ eV, $a_v = 1.16$ eV, $b = -1.7$ eV and $\nu = 0.318$. This results in $\Delta E/\epsilon_{xx} = -1.91$ eV. In practice, the stress is applied

along the [110] direction⁵⁷. In this case, we find that $\Delta E/\epsilon_{110} = -1.80$ eV (-435 THz). (The slight difference with respect to stress along [100] arises from the anisotropy in the stiffness tensor for GaAs.) Based on the measured frequency shift and this calculation, we estimate the maximum strain experienced by the QD at $+143$ V (-143 V) to be $\epsilon_{110} = -1.18 \times 10^{-3} (+1.47 \times 10^{-3})$. (Note that the heavy- and light-hole mixing in GaAs QDs could slightly reduce the ϵ_{110} values in reality.)

2.4 Narrow-Linewidth and Single-Photon Characteristics During Strain-Tuning

Figure 2.2(b) shows the resonance fluorescence of a selected area in Fig. 2.2(a) with a better resolution. The QD resonance features a bright and narrow line as its frequency is tuned continuously by the externally induced strain. The linewidth (γ) of QD emission, shown as a function of the frequency in Fig. 2.2(c), stays narrow throughout the whole strain-tuning process. γ fluctuates slightly with a standard deviation of 0.07 GHz but there is no obvious dependence on the QD resonance frequency. Figure 2.2(d) plots three different resonance fluorescence scans, where different colours denote different tuning positions [see Fig. 2.2(a)]. The grey curve is a Lorentzian fit to the blue data points (zero-strain condition), indicating a linewidth of 1.26 GHz. The same fit matches the other two data sets similarly well. This means that despite the sizeable shift in emission energy, the spectral properties (such as spectral shape and linewidth) of the QD emission remain unaffected by the strain. We describe the tuning with a dynamic factor, the ratio of the total tuning range (R) to the resonance fluorescence linewidth, and find $R/\gamma \simeq 920$. Similar results were observed for at least three different QDs in the region of the sample close to the middle of the gap.

In order to characterise the single-photon property of the emission⁷⁹, we perform a Hanbury Brown and Twiss (HBT) measurement under CW resonant excitation. We send the QD signal through a 50:50 beamsplitter and detect it with two superconducting nanowire single-photon detectors. Figure 2.3 displays the measured second-order correlation function $g^{(2)}(\tau)$ as a function of delay τ in three different conditions: (a) with maximum tension (-150 V applied), (b) zero stress (0 V), (c) with maximum compression ($+150$ V applied). In all three cases, the QD photons are time-tagged for over an hour with stable count rates, demonstrating that our strain tuning technique is suitable for measurements involving long timescale integration.

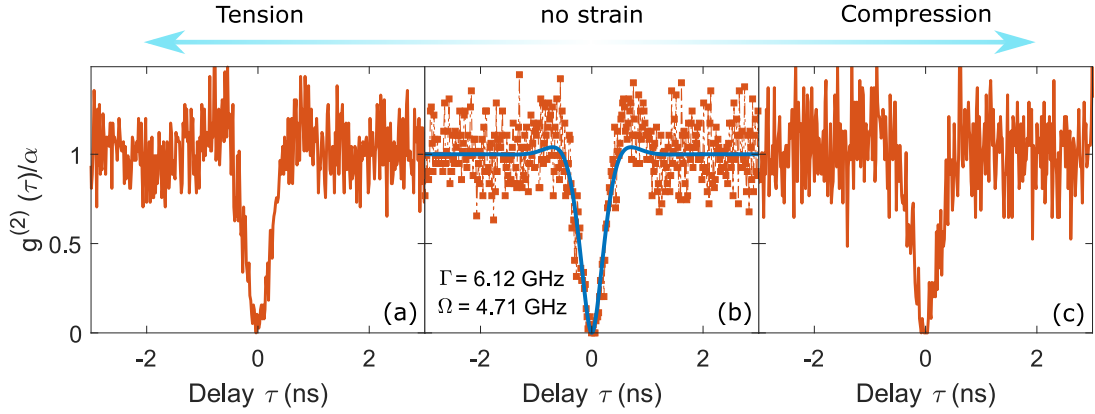


Fig. 2.3. **Measured second-order correlation function $g^{(2)}(\tau)/\alpha$ under resonant continuous-wave excitation** at (a) maximum tension, (b) zero stress, and (c) maximum compression. In all three cases, the dip around zero time-delay ($\tau = 0$) drops to near-zero, indicating single-photon emission from the GaAs QD. The fitting function Eq. 2.1 is implemented to subplot (b), yielding a decay rate $\Gamma = 6.12$ GHz and a Rabi frequency $\Omega = 4.71$ GHz. The measured second-order correlation function is normalised to one at times of a few nanoseconds (due to the heavy blinking effect). The effect of blinking on longer timescales^{38,48} (indicated by the factor α , $\alpha \sim 10$ shows strong bunching characteristic) is not shown in the plots.

Within a two-level model, $g^{(2)}(\tau)$ is described by⁴⁸:

$$g^{(2)}(\tau) = 1 - e^{-\frac{3\Gamma\tau}{4}} \left(\cos\lambda\tau + \frac{3\Gamma}{4\lambda} \sin\lambda\tau \right), \quad (2.1)$$

with $\lambda = \sqrt{\Omega^2 - \frac{\Gamma^2}{16}}$, Γ representing the upper-level decay-rate, and Ω being the Rabi frequency. The relationship between Γ and Ω is extracted from a intensity power curve in Fig. 2.2(e). Subsequently, Eq. 2.1 is fitted to the experimental data Fig. 2.3, where we obtain $\Gamma = 6.12$ GHz (radiative lifetime 163 ps; linewidth transform-limit 0.97 GHz) and $\Omega = 4.71$ GHz. The two-level model describes the data well. In particular, $g^{(2)}(0)$ is zero in the model and this crucial feature – it signifies photon antibunching – is observed in all the three experimental data sets. This shows that the QD is a good single-photon emitter at zero strain and retains this property under both tensile and compressive strain.

2.5 Summary

In this chapter, we present bidirectional frequency tuning of narrow-linewidth QD emission by external stress. Our results show that strain tuning can be used as a non-destructive method to modify QD emission frequency over a large range, neither broadening the emission linewidth nor reducing the single-photon purity. Although not being tested on our device, the induced strain is shown elsewhere to be a tool to reduce the fine-structure splitting. Changing the QD emission frequency over a large range while minimising the fine-structure splitting might require strain in multiple directions. Compared to other platforms such as $\text{Pb}(\text{Mg}_{1/3}\text{Nb}_{2/3})\text{O}_3\text{--PbTiO}_3$ (PMN–PT) based device, which have been used mostly for nano-membranes, our strain tuning apparatus provides a convenient way of applying stress to thick wafers with long-time stability (in hours) and high precision. The tuning range can be extended further by applying larger voltages to the PZT stacks (e.g. ± 300 V with reduced helium pressure), by reducing the gap in the strain device, and possibly by softening the sample further.

Chapter 3

Low-Noise GaAs Quantum Dots in an $n-i-p$ Diode

This chapter is adapted from:

Liang Zhai, Matthias. C. Löbl, Giang Nam Nguyen, Julian Ritzmann, Alisa Javadi, Clemens Spinnler, Andreas D. Wieck, Arne Ludwig, and Richard J. Warburton, *Low-noise GaAs quantum dots for quantum photonics*, **Nature Communications** 11, 4745 (2020).

Quantum dots are both excellent single-photon sources and hosts for single spins. This combination enables the deterministic generation of Raman-photons – bandwidth-matched to an atomic quantum memory – and the generation of photon cluster states, a resource in quantum communication and measurement-based quantum computing. GaAs quantum dots in AlGaAs can be matched in frequency to a rubidium-based photon memory, and have potentially improved electron spin coherence compared to widely used InGaAs quantum dots. However, their charge stability and optical linewidths are typically much worse than their InGaAs counterparts. In this chapter, we embed GaAs quantum dots into an $n-i-p$ -diode specially designed for low-temperature operation. We demonstrate ultralow-noise behaviour: charge control via Coulomb blockade, close-to-lifetime-limited linewidths, and no blinking. We observe high-fidelity optical electron-spin initialisation and long electron-spin lifetimes for these quantum dots. Our work establishes a material platform for low-noise quantum photonics close to the red part of the spectrum.

3.1 Background

Quantum dots (QDs) in III-V semiconductors form excellent sources of indistinguishable single photons. These emitters have a combination of metrics (brightness, purity, coherence, repetition rate) which no other source can match^{7,9,10,36,43,80,81}. These excellent photonic properties can be extended by trapping a single electron to the QD, enabling spin-photon entanglement⁸² and high-rate remote spin-spin entanglement creation²⁷. Underpinning these developments are, first, a self-assembly process to create nano-scale QDs; and second, a smart heterostructure design along with high-quality material. The established platform consists of InGaAs QDs embedded in GaAs. However, InGaAs QDs emit at wavelengths between 900 nm and 1200 nm, a spectral regime lying inconveniently between the telecom wavelengths (1300 nm and 1550 nm) and the wavelength where silicon detectors have a high efficiency⁸³ (600 nm - 800 nm). It is important in the development of QD quantum photonics to extend the wavelength range towards both, shorter and longer wavelengths.

GaAs QDs in an AlGaAs matrix can be self-assembled by local droplet etching^{13,15} and have a spectrally narrow ensemble^{14,17}. They emit at wavelengths between 750 nm and 800 nm. This is an important band: It coincides with the peak quantum efficiency of silicon detectors; it contains the rubidium D₁ and D₂ wavelengths (795 nm and 780 nm, respectively) offering a powerful route to combining QD photons with a rubidium-based quantum memory^{35,52}. Furthermore, GaAs QDs typically have more symmetric shapes, facilitating the creation of polarisation-entangled photon pairs from the biexciton cascade^{81,84}.

GaAs QDs also have very low levels of strain^{13,40,85-87}. In contrast, the high level of strain in InGaAs QDs complicates the interaction of an electron spin with the nuclear spins on account of the atomic-site-specific quadrupolar interaction^{40,88}. For electrostatically defined GaAs QDs, the spin-dephasing time, T_2^* , has been extended to the microsecond regime by narrowing the nuclear spin distribution together with real-time Hamiltonian estimation⁸⁹. Applied to a droplet GaAs QD, such techniques could prolong the spin dephasing time to values several orders of magnitude above the radiative lifetime. In this case, in combination with optical cavities^{10,11}, droplet GaAs QDs can potentially serve as fast and high-fidelity sources of spin-photon pairs and cluster states^{26,90}.

The development of GaAs QDs for quantum photonics lags far behind that of InGaAs QDs. Recurrent problems are blinking^{48,50,72} (telegraph noise in emission) and optical linewidths well above the lifetime limit^{44,50,63,84,86}. Both of these problems are caused

by noise in semiconductors. On short time-scales, the charge environment is static such that successively emitted photons exhibit a high degree of coherence^{44,81}. On longer time-scales however, the charge noise introduces via blinking an unacceptable stochastic character to the photon stream. An additional weak non-resonant laser provides control over the noise to a certain extent, though it does not remove the blinking completely^{48,72}.

For InGaAs QDs, embedding the QDs in an *n-i-p* diode has profound advantages: the charge state is locked by the Coulomb blockade^{8,54,64}; the charge noise is reduced significantly⁷⁰; and the exact transition frequency can be tuned in-situ via a gate voltage^{9,53}. Such a structure is missing for GaAs QDs^{44,48,50,63,72,84,86} – in previous attempts, charge stability was not demonstrated^{55,56}. A materials issue must be addressed: the barrier material AlGaAs must be doped, yet silicon-doped AlGaAs contains DX-centres^{91,92} which both reduce the electron concentration, causing the material to freeze out at low temperatures, and lead to complicated behaviour under illumination. In this chapter, we resolve this issue – all doped AlGaAs layers have a low Al-concentration. In this case, the DX level lies above the conduction band minimum and is therefore not occupied at cryogenic temperatures⁹¹. The GaAs QDs are grown in a region with higher Al-concentration, the established technique for these QDs¹⁵. On GaAs QDs in this device, we demonstrate charge control via Coulomb blockade, optical linewidths just marginally above the transform limit, blinking-free single-photon emission, electron spin initialisation, and a spin-relaxation time as large as $\sim 50 \mu\text{s}$.

3.2 Sample Design and Characterisation

The sample is grown on a GaAs substrate with (001)-orientation. The QDs are embedded in an *n-i-p*-diode structure where the QDs are tunnel-coupled to the *n*-type layer. The *n*-type back gate consists of silicon-doped $\text{Al}_{0.15}\text{Ga}_{0.85}\text{As}$. The low Al-concentration in this layer is crucial to avoid the occupation of DX-centres in *n*-type AlGaAs^{91,92}. A tunnel barrier consisting of 20 nm $\text{Al}_{0.15}\text{Ga}_{0.85}\text{As}$ followed by 10 nm $\text{Al}_{0.33}\text{Ga}_{0.67}\text{As}$ separates the QDs from the *n*-type back gate. The QDs are grown in the $\text{Al}_{0.33}\text{Ga}_{0.67}\text{As}$ -layer by using local droplet-etching¹⁵. The QD-density is $n_{\text{QD}} = 0.37 \pm 0.01 \mu\text{m}^{-2}$. Above the QDs, there is 274 nm of $\text{Al}_{0.33}\text{Ga}_{0.67}\text{As}$ followed by a *p*-type top gate. The top gate is composed of carbon-doped $\text{Al}_{0.15}\text{Ga}_{0.85}\text{As}$, where reduced Al-concentration is used as well. A schematic bandstructure of the diode is shown in Fig. 3.1(a); all Al-concentrations in this design are small enough that processing into micropillars⁹⁴ and nanostructures will not be hindered by oxidation⁹⁵. In Table 3.1, details of the complete heterostructure are given.

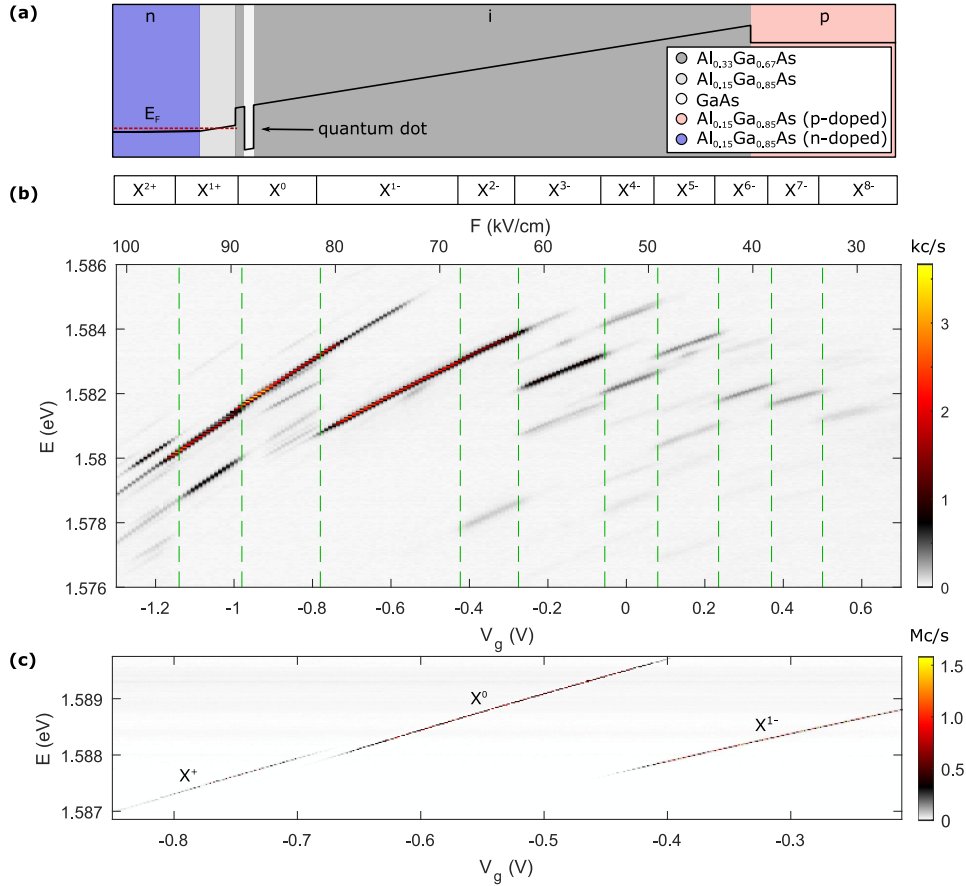


Fig. 3.1. **Charge tuning of single GaAs quantum dots.** (a) Schematic bandstructure (conduction band) of the diode hosting charge-tunable GaAs quantum dots. (b) The photoluminescence emitted by an exemplary quantum dot as a function of the gate voltage, V_g . The corresponding electric field, F , is plotted as an additional x-axis on top. The photoluminescence is resolved in energy by a spectrometer and measured on a CCD-camera. The emission spectrum shows several plateaus corresponding to different charge states of the quantum dot. We observe narrow photoluminescence linewidths on highly charged excitons where up to eight additional electrons occupy the quantum dot. (c) Resonance fluorescence from X^+ , X^0 , and X^{1-} charge plateaus measured on another quantum dot (QDA). The measurement is performed by sweeping the gate voltage for different laser frequencies. The resonance fluorescence intensity is measured with a superconducting nanowire single-photon detector. This measurement is performed by resonant continuous-wave (CW) excitation below saturation. In saturation with CW excitation, the maximum count rate is 6.5 MHz [see Fig. 3.7(a)].

We characterise our device by measuring the photoluminescence of a single GaAs QD as a function of the gate voltage (V_g) applied to the diode [see Fig. 3.1(b)]. As a function of V_g , the emission lines show a pronounced Stark shift. At specific gate voltages, discrete jumps in the emission spectrum take place: one emission line abruptly

Material	Thick (nm)	Temp ($^{\circ}\text{C}$)	Time (s)	Comments
GaAs:C	5	540	25.1	p^{++} -doped epitaxial gate
$\text{Al}_{0.15}\text{Ga}_{0.85}\text{As}$:C	10	540	42.7	p^{++} -doped epitaxial gate
$\text{Al}_{0.15}\text{Ga}_{0.85}\text{As}$:C	65	540	277.7	p^{+} -doped epitaxial gate
$\text{Al}_{0.33}\text{Ga}_{0.67}\text{As}$	273.6	540	921.8	blocking barrier
GaAs	2	605	10	filling of the etched nano-holes
–	–	605	60	droplet etching
Al	–	605	3.7	Al-droplet 0.09 nm plus 1 ML Al
$\text{Al}_{0.33}\text{Ga}_{0.67}\text{As}$	10	590	33.7	tunnel barrier (part 3)
$\text{Al}_{0.15}\text{Ga}_{0.85}\text{As}$	15	590	64.1	tunnel barrier (part 2)
$\text{Al}_{0.15}\text{Ga}_{0.85}\text{As}$	5	575	21.4	tunnel barrier (part 1)
$\text{Al}_{0.15}\text{Ga}_{0.85}\text{As}$:Si	150	590	640.8	n^{+} -doped back contact
$\text{Al}_{0.15}\text{Ga}_{0.85}\text{As}$	50	590	209.3	buffer layer
$\text{AlAs}/\text{Al}_{0.33}\text{Ga}_{0.67}\text{As}$	$10 \times (67.1/59.6)$	590	8904.7	distributed Bragg reflector
GaAs/AlAs	$22 \times (2.8/2.8)$	590	1101.7	short-period superlattice
GaAs	100	590	601.8	start

Table 3.1. **Sample design with relevant growth parameters.** For the Al-layer, the amount of deposited aluminium is given as the thickness of the corresponding AlAs layer. In our molecular beam epitaxy chamber, the background impurity concentration is estimated to be $\sim 5 \times 10^{14} \text{ cm}^{-3}$ for $\text{Al}_{0.33}\text{Ga}_{0.67}\text{As}$ layers⁹³. The doping concentration is $\sim 2 \times 10^{18} \text{ cm}^{-3}$ for the n^{+} back-contact, while for p^{+} and p^{++} layers, it is around $2 \times 10^{18} \text{ cm}^{-3}$ and $8 \times 10^{18} \text{ cm}^{-3}$, respectively. Between the n -type back gate and the p -type top gate, the sample has a built-in potential of 1.82 V.

becomes weaker and another line appears. This effect is the characteristic signature of charge-control of a QD via Coulomb blockade⁵⁴: the net-charge of the QD increases one by one and the emission energy is shifted due to the additional Coulomb interaction with the new carrier.

We fit the relation $E = E_0 + \alpha F + \beta F^2$ to the dependence of the emission energy E on electric field F (see Fig. 3.4 in Methods section). The energy jumps between different charge plateaus are removed for the fit. We find $\alpha/e = 0.21 \text{ nm}$, the permanent dipole moment in the growth direction, and $\beta = -1.35 \cdot 10^{-6} \text{ eV}/(\text{kV}/\text{cm})^2$, the polarisability of the QD⁹⁶. Extrapolating the fit shows that the Stark shift is zero at a non-zero electric field ($F = 7.8 \text{ kV}/\text{cm}$). The nonzero value of α represents a small displacement between the “centre-of-mass” of the electron and the hole wavefunctions. The hole wavefunction is slightly closer to the back gate than the electron wavefunction.

3.3 Resonance Fluorescence from GaAs QDs

We identify the neutral exciton, X^0 , from its characteristic fine-structure splitting as well as a quantum-beat in time-resolved resonance fluorescence [see Fig. 3.5 (a,b)]. For our device, the fine-structure splittings are distributed over a range of 1 – 3 GHz [see Fig. 3.6(c)]. The fine-structure splittings are comparable to literature values on (001)-oriented

samples^{15,81}. Smaller fine-structure splittings can be obtained by using (111)-oriented samples⁸⁴ and strain-tuning³³. We identify the other charge states by counting the number of jumps in the emission spectrum as the gate voltage increases/decreases. We measure emission from highly charged excitons ranging from the two-times positively charged exciton, X^{2+} , to the eight-times negatively charged exciton, X^{8-} . Such a wide range of charge tuning was not previously achieved with any QDs emitting in the close-to-visible wavelengths. Our GaAs QDs give a large range of charge tuning due to their relatively large size¹⁵ in comparison to the widely used InGaAs QDs⁹⁷.

We now turn to resonant excitation. This excitation scheme is key for creating low-noise photons and represents a true test of the fidelity of the device as, unlike photoluminescence, continuum states are not deliberately occupied. By sweeping both the gate voltage and excitation laser frequency, we map out three charge plateaus of a single quantum dot (QDA) – X^+ , X^0 , and X^{1-} . As is visible in Fig. 3.1(c), the exact transition energy of all three charge states can be tuned via V_g across a range of above 1 meV. At a fixed gate voltage, we determine a resonance fluorescence linewidth of X^{1-} to be 0.64 ± 0.01 GHz (full width at half maximum) on scanning a narrow-bandwidth CW laser over the trion resonance [see Fig. 3.2(a)]. This measurement takes several minutes: The linewidth probes the sum of all noise sources over a large frequency bandwidth⁹⁸. The measured linewidth is very close to the lifetime limit of $\Gamma_r/2\pi = 0.59 \pm 0.01$ GHz. [It is assumed here that the decay is radiative. The radiative decay rate Γ_r is determined by recording a decay curve following pulsed resonant excitation, Fig. 3.2(b)]. This result shows that there is extremely little linewidth broadening due to noise in our device. These excellent results are not limited to one individual QD. Shown in Fig. 3.2(d) is a linewidth measurement on a second QD (QDB). Resonance fluorescence laser-scans of QDB on X^+ and X^0 can be found in Fig. 3.5. In the central part of the X^{1-} charge plateau [from $V_g = -0.5$ V to $V_g = -0.4$ V in Fig. 3.2(c)], we also measure a close-to-lifetime-limited linewidth. On average, the ratio between the measured linewidth and the lifetime limit is 1.08 for QDB. At the edges of the charge-plateau, the linewidth increases – a known effect due to a co-tunnelling interaction with the Fermi-reservoir⁹⁹. Comparably good properties are found for in total seven out of ten randomly chosen QDs with X^{1-} below 785 nm [see Fig. 3.6(a,b)].

A remarkable feature is that the close-to-transform-limited linewidths are observed despite the large dc Stark shifts of these QDs. Within the X^{1-} plateau of QDA [Fig. 3.1(c)], the dc Stark shift is 0.0347 GHz/(V/cm), approximately four times greater than the typical dc Stark shifts of InGaAs QDs⁹⁸. The sensitivity of the transition frequency to the electric field renders the QD linewidth susceptible to charge noise. The close-

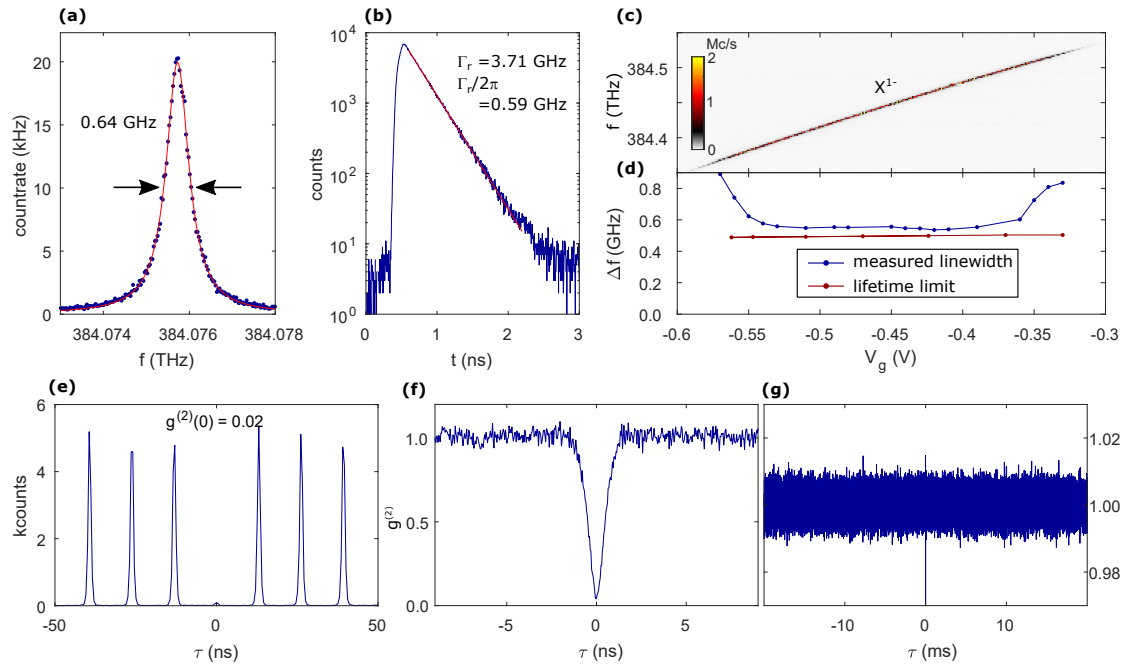


Fig. 3.2. Time-resolved lifetime and photon correlation measurements. (a) Resonance fluorescence linewidth measured on the singly-charged exciton, X^{1-} (QDA). The measurement is performed by sweeping a narrow-bandwidth laser over the X^{1-} resonance. The overall time for the shown scan is ~ 8 minutes. The measured linewidth is 0.64 ± 0.01 GHz (Lorentzian fit). (b) Lifetime measurement on X^{1-} under pulsed resonant excitation. The gate voltage is the same as in (a). The measured decay rate ($\Gamma_r = 3.71 \pm 0.04$ GHz, corresponding to a lifetime of $1/\Gamma_r = 270 \pm 3$ ps), implies a lifetime-limited linewidth of $\Gamma_r/2\pi = 0.59 \pm 0.01$ GHz (exponential fit). (c) Resonance fluorescence of X^{1-} (QDB) as a function of the gate voltage. (d) Resonance fluorescence linewidth along with the lifetime-limit (obtained from separate lifetime measurements at the corresponding gate voltages). Similar to QDA, the linewidth of QDB stays very close to the lifetime limit in the plateau centre. (e) Auto-correlation ($g^{(2)}$) measured under resonant π -pulse excitation. (f) Auto-correlation of the resonance fluorescence measured under weak CW excitation shown on a short time-scale. The $g^{(2)}$ measurement is normalised³⁸ by dividing the number of coincidences by its expectation value $T \cdot t_{\text{bin}} \cdot x_1 \cdot x_2$, where T is the overall integration time, t_{bin} is the binning time, and x_1, x_2 are the count rates on the two single-photon detectors. (g) The same auto-correlation measurement as in (f) but evaluated on a much longer time-scale (milliseconds). The perfectly flat $g^{(2)}$ reveals the absence of blinking.

to-transform limited linewidths reflect therefore an extremely low level of charge noise in the device. Assuming that the slight increase in broadening with respect to the transform limit arises solely from charge noise, the linewidth measurement places an upper bound of ~ 3.0 V/cm for the root-mean-square (RMS) electric field noise at the location of QDA. This upper bound is comparable to the very best gated InGaAs QD devices.^{70,98,100–102}

3.4 Blinking-Free Single-Photon Emission

For applications as a single-photon source, it is crucial to demonstrate that the photons are emitted one by one, i.e. photon anti-bunching. Therefore, we continue our analysis by performing an intensity auto-correlation ($g^{(2)}$) of the resonance fluorescence. This $g^{(2)}$ -measurement of QDA is shown in Fig. 3.2(e) and also in Fig. 3.9(c,d) under resonant π -pulse excitation (Coherent MIRA900, 76.3 MHz repetition rate). We observe a strong anti-bunching at zero time-delay, $g^{(2)}(0) = 0.019 \pm 0.008$, corresponding to a single-photon purity of $1 - g^{(2)}(0) \sim 98\%$. The corresponding measurement under weak continuous-wave excitation is shown in Fig. 3.2(f). ($g^{(2)}$ -measurements versus excitation power as well as laser detuning are mapped out in Fig. 3.8, where clear Rabi oscillations are shown. In both cases, we find excellent agreement between the measured $g^{(2)}$ and a calculation based on a simple two-level model.) The strong anti-bunching feature proves the single-photon nature of the QD emission.

Based on previous studies, resonance fluorescence on GaAs QDs is known to suffer from blinking, i.e. telegraph noise in the QD emission. This is a deleterious consequence of charge noise: either the QD charges abruptly or the charge state of a nearby trap changes, detuning the QD from the excitation laser in both cases. Blinking gives rise to a characteristic bunching ($g^{(2)} > 1$) in the auto-correlation even for driving powers well below saturation⁴⁸. We investigate this point here. Even out to long (millisecond) time-scales, the $g^{(2)}$ -measurement is absolutely flat and close to one [see Fig. 3.2(g)]. (We note that our analysis includes a mathematically justified normalisation of the $g^{(2)}$ -measurement.) This result demonstrates that blinking is absent in our device. This is a consequence both of the diode structure, in particular the Coulomb blockade which locks the QD charge, and the low charge noise in the material surrounding the QD.

We subsequently carried out auto-correlation measurements with either a small magnetic field along the growth direction or a laser slightly detuned from the QD resonance. In the former case, the sensitivity to spin noise is enhanced, while in the latter case the sensitivity to charge noise is enhanced⁹⁸. The results are shown in Fig. 3.11 in Methods section, where we compare the auto-correlation on millisecond time-scales. For the measurement with an additional magnetic field [see Fig. 3.11(c,d)], the $g^{(2)}$ remains flat and stays close to one. In contrast, we observe slight blinking behaviour when the laser is detuned [see Fig. 3.11(e,f)]. These results infer that, in our device, charge noise is most likely to account for the residual linewidth broadening.

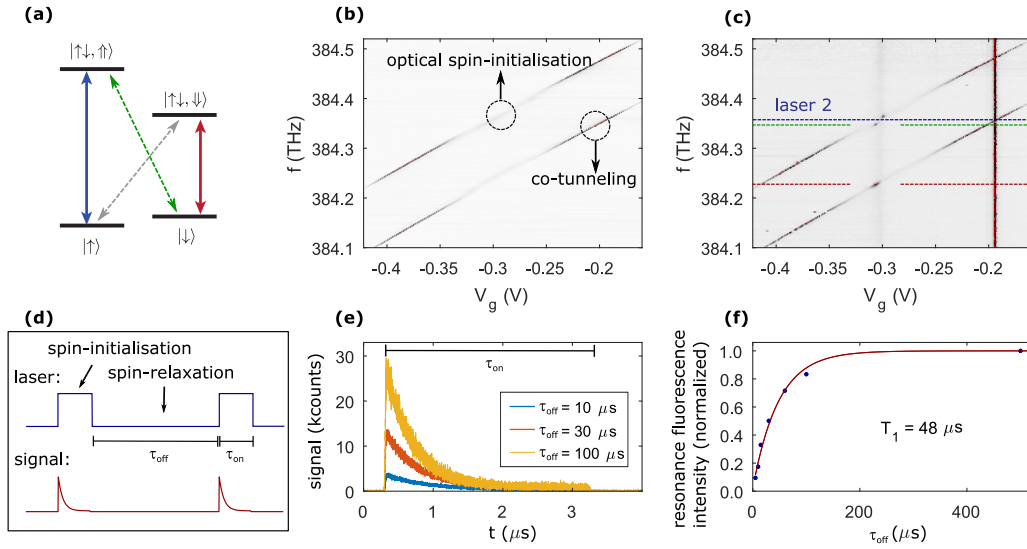


Fig. 3.3. **Initialisation of a single electron spin.** (a) Level scheme of the negative trion X^{1-} in a magnetic field (Faraday geometry). (b) Optical spin-initialisation via optical pumping on X^{1-} . The measurement is carried out at $B = 6.6$ T. At the centre of the plateau, the resonance fluorescence disappears due to successful spin-initialisation; at the plateau edges the signal remains due to rapid spin randomisation via co-tunnelling⁹⁹. (c) Optical spin-initialisation and re-pumping with a second laser at a fixed frequency (laser 2). Recoveries of the signal are found in the centre of the plateau. (d) Schematic of the time-resolved spin-pumping measurement. (e) Time-resolved resonance fluorescence measurements. The signal drops due to optical spin-initialisation after turning the driving laser on. The overall intensity is higher when the time delay τ_{off} between the laser pulses is larger. In this case, the spin has more time to relax back to the bright state. (f) Resonance fluorescence intensity as a function of the waiting time between the spin-pumping laser pulses. From this measurement, we extract an electron-spin lifetime of $T_1 = 48 \pm 5 \mu\text{s}$.

3.5 High-Fidelity Spin Initialisation

The diode structure allows us to load a QD with a single electron. The spin of the electron is a valuable quantum resource. To probe the electron-spin dynamics, we probe the X^{1-} resonance fluorescence in a magnetic field (Faraday-geometry). In this configuration, the ground state is split by the electron Zeeman energy and the excited state is split by the hole Zeeman energy [see Fig. 3.3(a)]. As the diagonal transitions in this level-scheme are close-to forbidden, the X^{1-} -charge-plateau splits into two lines which are separated by the sum of electron and hole Zeeman energies [see Fig. 3.3(b)]. We find that the X^{1-} charge-plateau becomes optically dim in its centre. This is the characteristic feature of spin-initialisation via optical pumping^{101,103,104}. On driving e.g. the $|\uparrow\rangle - |\uparrow\downarrow\rangle$ transition, the trion will most likely decay back to the $|\uparrow\rangle$ -state via the

dipole-allowed vertical transition. However, due to the heavy-hole light-hole mixing, it can also decay to the $|\downarrow\rangle$ -state through the “forbidden” diagonal transition with a small probability. When the QD is in the $|\downarrow\rangle$ -state, the driving laser is off-resonance on account of the electron Zeeman energy. Therefore, the centre of the X^{1-} -charge-plateau becomes dark and the initialisation of the electron spin in the $|\downarrow\rangle$ -state is heralded by the disappearing resonance fluorescence. At the plateau-edges, resonance fluorescence reappears due to fast spin-randomisation via co-tunnelling⁹⁹. By comparing the remaining intensity in the charge-plateau centre to the plateau edges, we estimate the spin initialisation fidelity to be $F = 98.3 \pm 0.3$ %. To confirm that the signal disappears in the plateau-centre on account of optical spin initialisation and not some other process, we perform a measurement with a second laser at a fixed frequency. When the fixed laser is resonant with $|\uparrow\rangle - |\uparrow\downarrow\uparrow\rangle$ transition, we observe a recovery of the signal [see Fig. 3.3(c)] on either driving the weak diagonal transition $|\uparrow\downarrow\uparrow\rangle - |\downarrow\rangle$ or the strong vertical transitions $|\downarrow\rangle - |\uparrow\downarrow\downarrow\rangle$ with the scan laser. While the fixed laser is tuned to $|\downarrow\rangle - |\uparrow\downarrow\uparrow\rangle$ transition (at a different V_g), another recovery spot is seen as the scan laser drives the vertical transition $|\uparrow\rangle - |\uparrow\downarrow\uparrow\rangle$. This confirms the optical spin-initialisation mechanism¹⁰³. From the energy splitting at the plateau edges, the electron and hole g-factors are determined⁸⁷, $g_e = -0.076 \pm 0.001$ and $g_h = 1.309 \pm 0.001$. For the positively charged trion (X^+), we also observe high-fidelity optical spin-initialisation [see Fig. 3.10] and narrow linewidths [0.62 GHz, see Fig. 3.5(c,d)], in this case of a hole spin.

How long-lived is the prepared spin state? To answer this question, we measure the time-dependence of the X^{1-} spin initialisation^{101,104}. The scheme is illustrated in Fig. 3.3(d). First, we drive the $|\uparrow\rangle - |\uparrow\downarrow\uparrow\rangle$ transition for $\tau_{\text{on}} = 3$ μs . During this laser pulse, the signal decreases due to optical spin-initialisation [see Fig. 3.3(e)]. Subsequently, we turn the laser off for a time τ_{off} , and then turn the laser back on again. During the off-time the electron spin randomises. Figure 3.3(e) shows that the resonance fluorescence signal is stronger when the waiting time τ_{off} is longer. The reason for this effect is that with increasing τ_{off} the spin has more time to randomise. For a short value of τ_{off} , in contrast, the spin remains in the off-resonant state – it has no time to relax before the next optical pulse is applied. By measuring the signal strength for varying τ_{off} [see Fig. 3.3(f)], we determine an electron-spin relaxation time of $T_1 = 48 \pm 5$ μs . Our result shows that the design of the tunnel-barrier between QDs and the back gate is well suited for spin experiments on single QDs. This T_1 value is significantly larger compared to that of the GaAs QDs without the *n-i-p* diode structure⁵⁰. The point is that the T_1 time is potentially longer than the coherence time T_2 , such that the relaxation process governing T_1 is unlikely to limit the coherence time T_2 .

3.6 Summary

In this chapter, we have developed charge-tunable GaAs QDs with ultra-low charge noise. We show notable improvements of the GaAs QDs properties: optical linewidths are close-to lifetime-limited, blinking is eliminated, and long electron-spin lifetimes are achieved. From a materials perspective, the crucial advance is the new diode structure hosting GaAs QDs – a key feature is that all the doping is incorporated in layers of low Al-concentration. In this way, the occupation of DX-centres is avoided and the AlGaAs layers are conducting at low temperatures. The concepts developed in this chapter can be transferred to thinner diode structures that allow integration into photonic-crystal cavities and other nanophotonic devices^{8,9,95}. From a quantum photonics perspective, our results pave the way to bright sources of low-noise single photons close to the red part of the visible spectrum. This will facilitate the development of both short-range networks and a hybrid QD-rubidium quantum memory. On account of the low-strain environment in GaAs QDs, our results can also open the door to prolonged electron spin coherence.

3.7 Methods

The sample heterostructure and the quantum dots were grown by molecular beam epitaxy (MBE). The overall growth conditions are similar to those described in Ref. 105. The complete heterostructure of the sample is shown in Table 3.1. All doped layers in Al-GaAs have low Al-concentration (15%). The quantum dots are surrounded by AlGaAs with higher Al-concentration (33%), to enable the growth of QDs close to rubidium-frequencies and with small fine-structure splittings^{15,17}.

Resonance fluorescence was performed with a narrow-bandwidth laser (~ 100 kHz linewidth), using a polarisation-based dark-field microscope to distinguished QD-signal from scattered laser light, and detected using superconducting-nanowire single-photon detectors (Single Quantum) and counting hardware (PicoQuant, HydraHarp) with a total timing jitter of ~ 35 ps (full width at half maximum). Details of the polarisation-based dark-field microscope are described in Refs. 75.

In our device, GaAs QDs with a small height (emission wavelength below ~ 785 nm) tend to have excellent optical properties. We find that more than every second QD has a close to lifetime-limited linewidth [see Fig. 3.6(a,b)]. This includes QDs close to the ^{87}Rb D_2 line (~ 780 nm). For QDs larger in size (emission wavelength above ~ 785 nm), the QD linewidths are usually broader. The reason is probably the following: the GaAs

QDs in our sample are grown by infilling nano-holes droplet-etched into a 10 nm-thin layer of $\text{Al}_{0.33}\text{Ga}_{0.67}\text{As}$ (see Table 3.1). The depths of the nano-holes, and therefore the heights of the QDs, typically range from 5 nm to 10 nm^{15,17}. A QD emitting at a higher wavelength tends to have a larger height¹⁷. When the height of a QD comes close to 10 nm, the optical properties could be affected by the $\text{Al}_{0.33}\text{Ga}_{0.67}\text{As}/\text{Al}_{0.15}\text{Ga}_{0.85}\text{As}$ interface. A simple solution is to make the $\text{Al}_{0.33}\text{Ga}_{0.67}\text{As}$ -layer 5 nm thicker. In this case, we also expect good optical properties for QDs of higher wavelengths.

We investigate the stability of the QD under different excitation schemes. We start with continuous-wave (CW) excitation. We perform auto-correlation measurements on X^{1-} at a constant gate voltage while exciting the QD with (i) an above-band laser ($\lambda = 632.8$ nm), (ii) a laser resonant with the p -shell, and (iii) a laser resonant with the $|s\rangle$ -to- $|s\rangle$ transition. The results are shown in (i) Fig. 3.9(a), (ii) Fig. 3.9(b), and (iii) Fig. 3.2(g), respectively. In all three cases, the $g^{(2)}$ stays very flat and close to one – there is no blinking even on a long time-scale. This shows that the QD is a very stable quantum emitter under all three CW excitation schemes. From an applications point of view (e.g. for a single-photon source application), it is usually necessary to drive the QD with a resonant pulsed laser. We investigate the auto-correlation under resonant π -pulse excitation in Fig. 3.2(e). An evaluation of this $g^{(2)}$ -measurement on a longer time-scale is plotted in Fig. 3.9(c), where the y-axis is displayed on a logarithmic scale to resolve the central peak. To investigate whether a strong π -pulse introduces any blinking, we plot the $g^{(2)}$ -measurement in a histogram plot [see Fig. 3.9(d)] by summing the coincidence events for every pulse. This sum is divided by the expectation value for a perfectly stable source: the normalisation factor is $x_1 x_2 T_{\text{int}} / f_{\text{rep}}$, where f_{rep} is the repetition rate of the pulsed laser, x_1, x_2 represent the count-rates of the two detectors used for a T_{int} -long $g^{(2)}$ -measurement. A derivation of the normalisation factor is given in the caption of Fig. 3.9. Importantly, the histogram bars at non-zero time delay are flat and very close to one; the bar at zero delay is close to zero. This shows that the QD is a stable single-photon emitter for resonant π -pulse excitation.

The $g^{(2)}$ -measurement shown in Fig. 3.2(f,g) is performed on a trion at zero magnetic field when the CW laser drives the QD resonantly. The sensitivity can be enhanced towards either spin noise or charge noise by applying a small magnetic field B along the growth direction, and detuning the laser slightly from the QD-resonance by δ , respectively. A trion state is degenerate at zero magnetic field, consisting of two opposite spin ground states. When applying a magnetic field B , the degeneracy is lifted and the trion state is split into two by a Zeeman energy $E_z = g\mu_B B$, with g being the electron or hole g -factor, and μ_B the Bohr magneton. We maximise the spin noise sensitivity by

applying a small magnetic field such that $E_z = \frac{\tilde{\Gamma}}{\sqrt{3}}$ [see Fig. 3.11(c)]. Here $\tilde{\Gamma}$ represents the full width at half maximum (FWHM) of the QD emission. For the maximised spin noise sensitivity, the $g^{(2)}$ -measurement does not show any clear sign of bunching [see Fig. 3.11(d)]. The charge noise sensitivity is maximised when the laser is detuned from the QD by $\delta = \frac{\tilde{\Gamma}}{2\sqrt{3}}$ [see Fig. 3.11(e)]. In this configuration, we observe a small bunching peak in the $g^{(2)}$ -measurement [see Fig. 3.11(f)]. This result suggests that charge noise on a millisecond time-scale is responsible for the slight linewidth broadening.

Below we add relevant experimental details in the figure format:

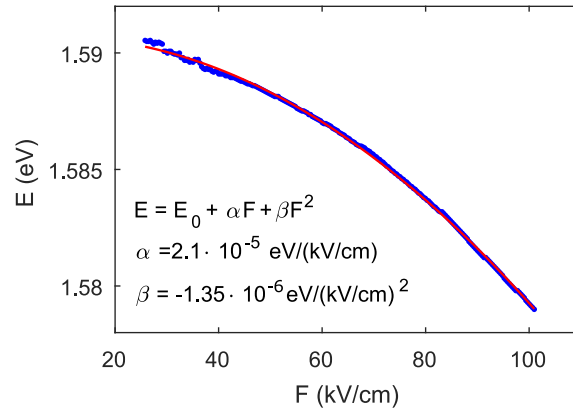


Fig. 3.4. **Photoluminescence resolved by a spectrometer as a function of external electric field.** Photoluminescence energy (E) versus electric field (F) for the quantum dot¹⁰⁶ shown in Fig. 3.1. F is obtained by a bandstructure simulation. The solid curve is a quadratic fit to the data. We extract the permanent dipole moment to be $\alpha/e = 0.21 \text{ nm}$, and the polarisability $\beta = -1.35 \mu\text{eV}/(\text{kV}/\text{cm})^2$.

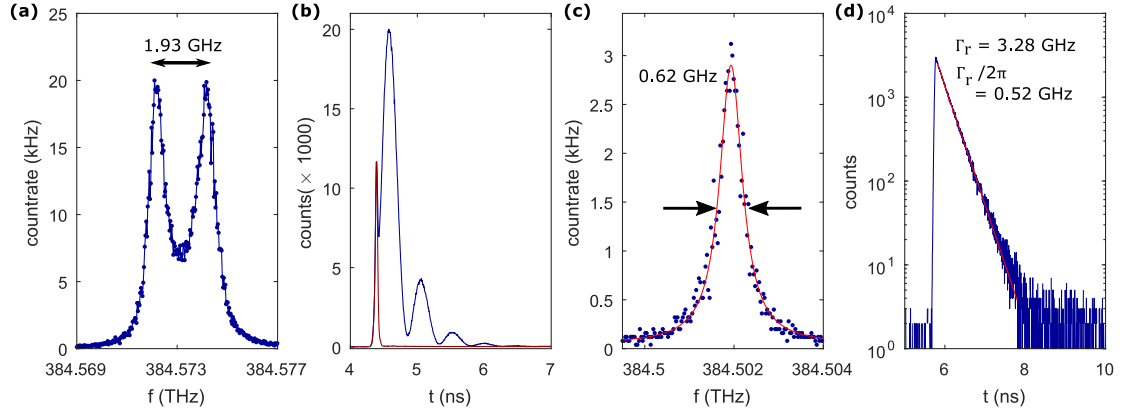


Fig. 3.5. **Spectral and time-resolved resonance fluorescence** (a) Resonance fluorescence from the neutral exciton, X^0 , measured on QDB. The neutral exciton has a small fine structure splitting of $FSS = 1.93$ GHz ($7.98 \mu\text{eV}$). (b) Lifetime measurement on the X^0 (QDB). Resonance fluorescence (blue) is measured as a function of the time delay t after exciting X^0 with a picosecond laser pulse. Here, a pronounced quantum beat with a frequency of $\frac{2\pi}{FSS}$ is observed. The red curve corresponds to the background from the scattered laser light. (c) Resonance fluorescence measurement (blue) on the positively charged exciton, X^+ , from QDB. The red curve is a Lorentzian fit. The X^+ shows a narrow optical linewidth of 0.62 GHz. (d) Lifetime measurement (blue) on the X^+ (QDB). The radiative decay rate, which corresponds to a natural linewidth of $\Gamma_r/2\pi = 0.52$ GHz, is extracted by fitting an exponential curve (red).

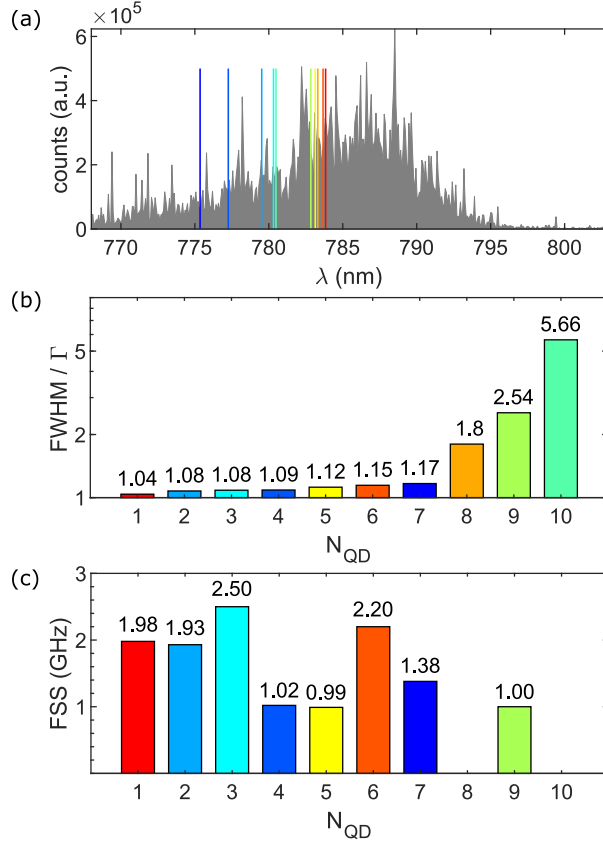


Fig. 3.6. **Summary of the optical properties of ten randomly chosen QDs.** (a) Emission of the QD-ensemble at a gate voltage of $V_g = -0.4$ V. The coloured lines indicate the emission wavelengths of the QDs (X^{1-}) that have been measured in detail. (b) Ratio between the measured optical linewidth (full width at half maximum, FWHM) on the negatively charged exciton X^{1-} and its lifetime limit (Γ) shown for ten randomly chosen QDs. On the x-axis, N_{QD} indicates the QD number sorted by the ratio FWHM/ Γ in ascending order. The colours of the bars are linked to the colours in (a). In the ideal case, the optical linewidth of QD reaches the lifetime limit: the ratio FWHM/ Γ is one. For the majority of QDs, the ratio is close to one – below a level of FWHM/ $\Gamma = 1.2$ we find seven QDs out of ten. These QDs suffer from little noise. The QDA and QDB investigated in the paper are labelled here as $N_{\text{QD}} = 3$ and $N_{\text{QD}} = 2$, respectively. For a few QDs, there is a rather large broadening of the linewidth beyond the lifetime limit. (c) Fine structure splitting (FSS) for the neutral exciton (X^0) measured on the same QDs as in (b). The FSS is determined by scanning the laser frequency across the QD resonance. An example is shown in Supplementary Fig. S3. As in (b), the colours of the bars are linked to the QD wavelengths in (a). For most of the QDs, the FSS is below 2 GHz. For $N_{\text{QD}} = 9$, we state here an upper bound of 1 GHz for its FSS. For $N_{\text{QD}} = 8$ & 10, determining the FSS by scanning a laser across X^0 was not successful due to the relatively large linewidth.

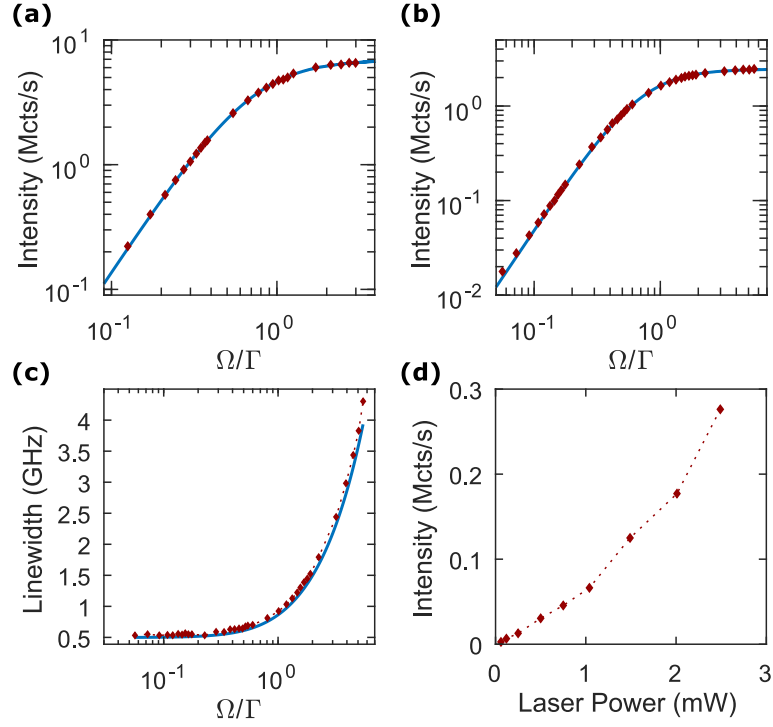


Fig. 3.7. Power curve of GaAs quantum dots. (a) Intensity of resonance fluorescence (red diamonds) of X^{1-} from QDA as a function of the normalised Rabi-frequency Ω/Γ . The resonance fluorescence is measured using a dark-field con-focal microscope⁷⁵. The intensity saturates at around 6.5 Mcts/s (raw count rate). The blue curve is a theoretical fit of a two-level model¹⁰⁷. (b) Power dependent resonance fluorescence measurement (red diamonds) of X^{1-} from QDB. The measurement is performed in a way similar to the one shown in (a) and recorded with a superconducting nanowire single-photon detector (SNSPD). The intensity saturates around 2.5 Mcts/s (raw data, the slightly lower saturation count-rate is because of the lower efficiency of the SNSPD). Similarly, the blue curve represents the theoretical fit of a two-level model. (c) Optical linewidth (red) of the resonant fluorescence from QDB X^{1-} displayed as a function of the normalised Rabi-frequency Ω/Γ . The linewidth measurements are performed by scanning the gate voltage across the QD resonance under different excitation laser powers (the laser frequency is fixed). The linewidths are fitted to Lorentzian functions and converted into frequency unit using a Stark shift of 621.679 GHz/V [see Fig. 3.2(c)]. The linewidths stay very close to the lifetime limit (496 MHz) at low power and become broader due to the power broadening effect at higher powers. The blue curve represents the power broadening effect of a two-level system. The plot is not a fit, but rather a two-level theoretical calculation using the parameters Γ as well as Ω extracted from (b). The measured optical linewidths stay close (marginally above) to theoretical values for all excitation powers. (d) Intensity of photoluminescence of X^{1-} from the same QD (QDB), plotted as a function of non-resonant laser power. This non-resonant laser is a CW He-Ne laser emitting at $\lambda = 633$ nm. The non-resonant laser power is measured before we send it to the dark-field microscope. Photoluminescence is measured at the same gate voltage as in (b). It is collected by the dark-field microscope setup, sent through a grating-based filter and counted by the SNSPD. Under lower-power non-resonant excitation, we determine an upper bound of 7.7 GHz for the photoluminescence linewidth. This boundary is obtained by fitting the photoluminescence spectrum to a Lorentzian function and is limited by the resolution of the spectrometer. The actual photoluminescence linewidth shall be much narrower.

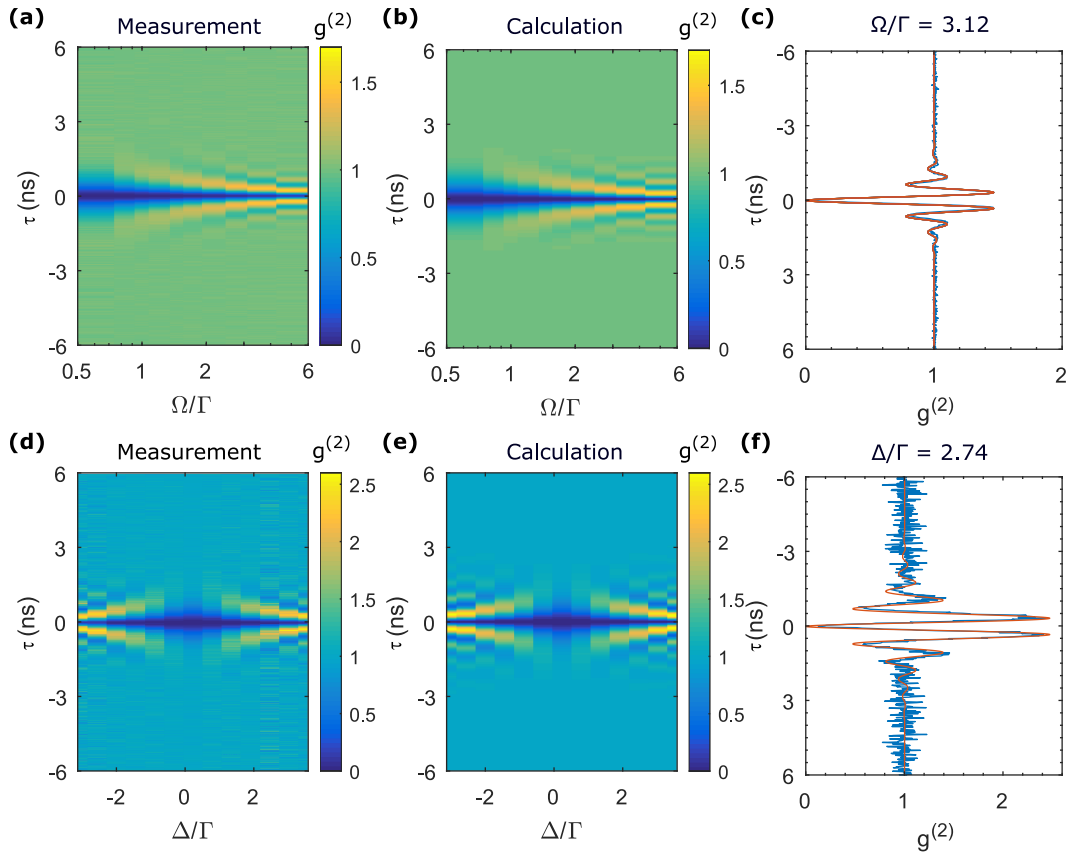


Fig. 3.8. Comparing a low-noise GaAs QD with an ideal two-level system in auto-correlation measurements. (a) Time-resolved intensity auto-correlation measurement, $g^{(2)}(\tau)$, as a function of the normalised Rabi-frequency Ω/Γ . Measurement is carried out under continuous wave (CW) resonant excitation on the negatively charged exciton, X^{1-} , from QDB. The $g^{(2)}(\tau)$ is normalised to one by the number of coincidence events at 300 ns delays. The Rabi frequency Ω is extracted independently from a power saturation curve under CW resonant excitation, while the radiative decay rate Γ is obtained by fitting an exponential function to the lifetime measurement. (b) Calculation of the power-dependent auto-correlation function. The $g^{(2)}(\tau)$ function is calculated by solving the optical Bloch equations of a two-level system and then applying the quantum regression theorem. The calculation is carried out with QuTip¹⁰⁸. We chose to ignore upper-level dephasing in this calculation⁴⁸. The normalised Rabi-frequency is taken from the measurement in (a). Under a strong driving field ($\Omega \gg \Gamma$), the $g^{(2)}(\tau)$ value approaches its upper bound¹⁰⁹ $g^{(2)}(\tau = \pm\pi/\Omega) = 2$. (c) Comparison between the measured $g^{(2)}(\tau)$ (blue) and the calculation (red) for $\Omega/\Gamma = 3.12$. (d) Time-resolved intensity auto-correlation measured as a function of normalised laser detuning, Δ/Γ . The excitation laser power is locked to $\Omega = 0.49 \Gamma$. (e) Calculation of the detuning-dependent auto-correlation function in a two-level system. Under a detuned driving, the effective Rabi-frequency^{107,110} is represented as $\sqrt{\Omega^2 + \Delta^2}$. In the calculation, the dephasing is again set to zero, and the values of Δ/Γ are taken from (d). In both the measurement and the calculation, the maximum value of $g^{(2)}(\tau)$ exceeds 2, the upper bound in the resonant case, when Δ is relatively large compared to Γ . (f) Comparison between the experiment (blue) and the calculation (red) under the condition $\Delta/\Gamma = 2.74$, $\Omega/\Gamma = 0.49$. We find a perfect overlap between the data and the calculation, indicating that the X^{1-} behaves as an ideal two-level system.

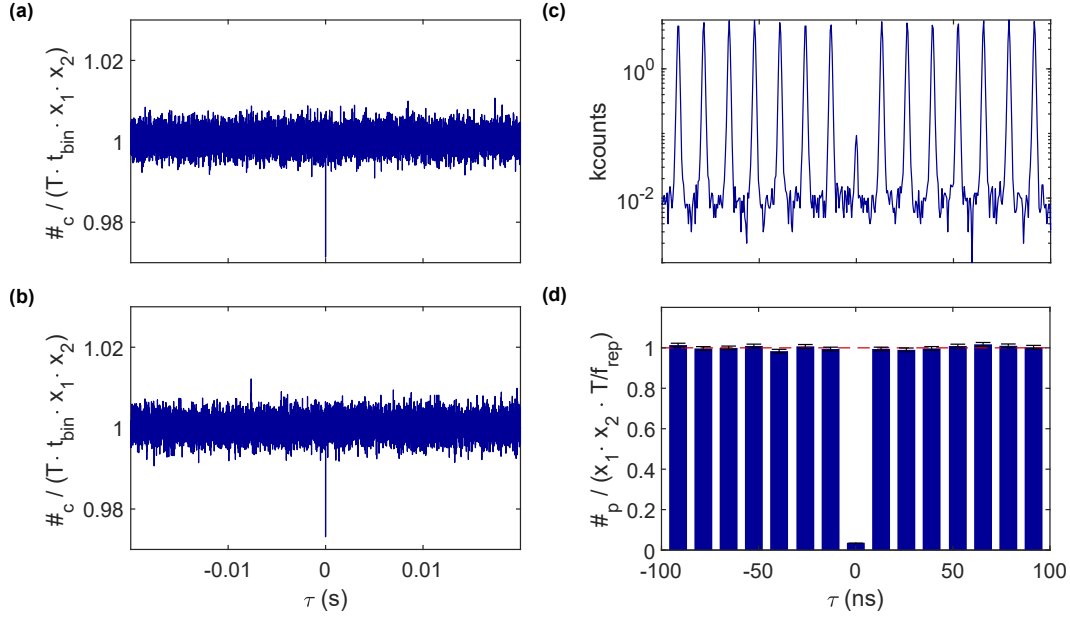


Fig. 3.9. **Auto-correlation measurements of QDA X^{1-} under non-resonant CW and resonant pulsed excitation.** (a) The auto-correlation measurement performed under above-band excitation with a laser at $\lambda = 632.8$ nm. The $g^{(2)}$ is close to the ideal Poissonian limit of one for all time-scales, demonstrating the long-time stability of the emitter. (b) The auto-correlation measurement performed by exciting the quantum dot via p -shell excitation. Similarly here, the $g^{(2)}$ is flat and close to the ideal Poissonian limit. (c) The pulsed $g^{(2)}$ -measurement (resonant π -pulse excitation) from Fig. 3.2(e) plotted on a logarithmic scale and evaluated on a longer time-scale. The offset (about ten coincidence events) arises from detector dark counts. For the calculation of the $g^{(2)}(0)$ value of $g^{(2)}(0) = 0.019$, we have subtracted this dark-counts-induced background. By integrating all coincidence events over one full pulse period without substrating the background, we estimate a “worst-case” upper limit: $g^{(2)}(0) = 0.036$. (d) The same $g^{(2)}$ -measurement as in (c) but plotted as a histogram. To obtain the histogram, we sum up all coincidence events within every single pulse and normalise it by the expectation value for the coincidence events in the case of an ideal Poissonian source: $\langle \#_p \rangle = x_1 x_2 T_{\text{int}} / f_{\text{rep}}$, where x_1 and x_2 are the count rates of each detector channel, $T_{\text{int}} = 2500$ s is the overall integration time for the measurement, and $f_{\text{rep}} = 76.3$ MHz is the repetition rate of the pulsed laser. Using this normalisation factor, the $g^{(2)}$ -measurement normalises to a value very close to the ideal limit of one. This evaluation shows that the quantum dot is a very stable emitter under resonant π -pulse excitation. The normalisation factor $\langle \#_p \rangle$ is obtained by a similar consideration compared to the case of continuous wave excitation³⁸: Let p_1 and p_2 be the probabilities that a photon is detected on channel 1 or 2, after the π -pulse excitation. The count rates x_1 , x_2 are then connected to these probabilities by $x_1 = f_{\text{rep}} p_1$, $x_2 = f_{\text{rep}} p_2$. In case of two uncorrelated channels, the joint probability for one detection event on channel 1 together with another detection event for a later or earlier excitation pulse on channel 2 is $p_1 p_2 = x_1 x_2 / f_{\text{rep}}^2$. The expectation value for the overall number of joint (coincidence) events is then $p_1 p_2$ times the overall number of π -pulses, $T_{\text{int}} \cdot f_{\text{rep}}$. This consideration leads to the aforementioned expression: $\langle \#_p \rangle = x_1 x_2 / f_{\text{rep}}^2 \times T_{\text{int}} \cdot f_{\text{rep}} = x_1 x_2 T_{\text{int}} / f_{\text{rep}}$.

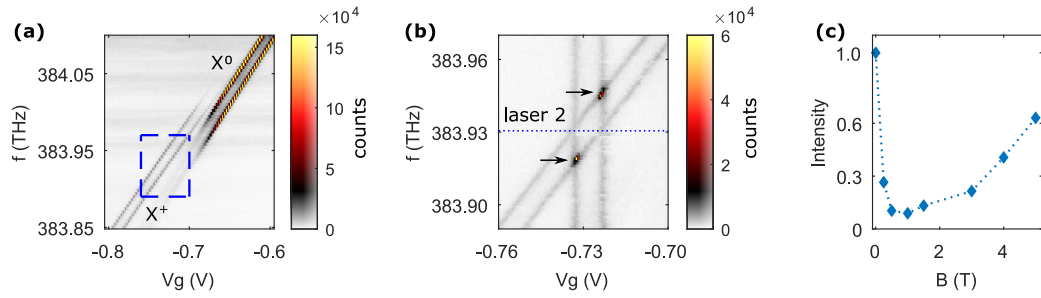


Fig. 3.10. **Optical Spin pumping of the X^+ .** (a) Resonance fluorescence charge-plateau of the positively charged trion, X^+ , and the edge of the X^0 charge-plateau (QDA). The X^+ -lines are split in a magnetic field ($B = 1.5$ T). The resonance fluorescence is weak due to optical spin-initialisation of the hole-spin. (b) The signal recovers (marked with arrows) on addressing a second spin-ground state with a second laser (dashed line). This second laser is kept at a fixed frequency and a fixed power (same power as in (a)). The blue frame in (a) indicates the range over which the gate voltage and the first laser are tuned in this measurement. Two additional vertical lines are observed when the fixed laser is on resonance with the two vertical transitions. (c) Brightness of the X^+ resonance fluorescence as a function of the magnetic field. The brightness is normalised to the resonance fluorescence intensity at $B = 0$ T. At about 1 T, the signal has a minimum, suggesting that the lifetime of the hole-spin is the longest at this magnetic field¹¹¹.

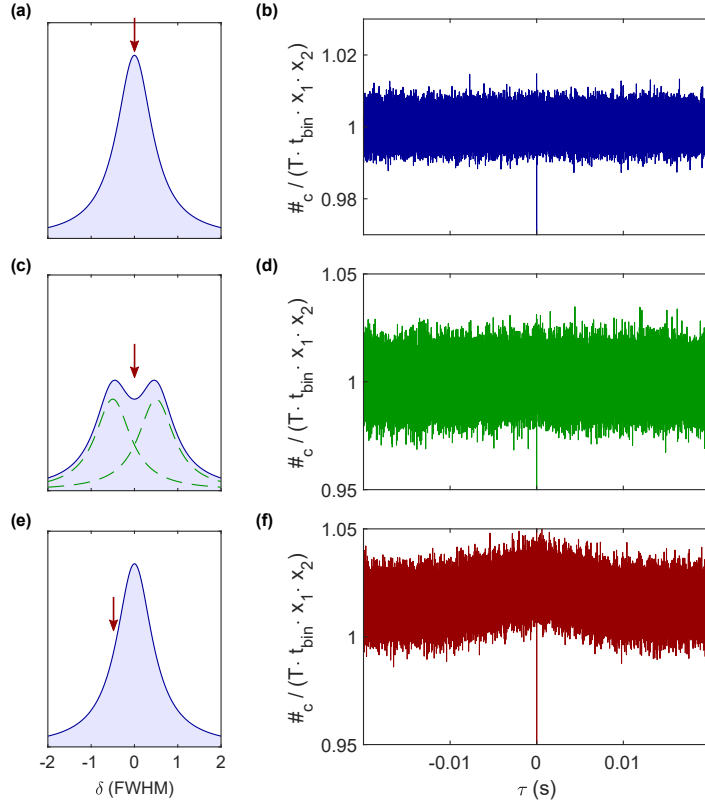


Fig. 3.11. **Auto-correlation of the resonance fluorescence on QDA X^{1-} .** (a) Configuration for resonant auto-correlation measurement. The measurement is performed at zero magnetic field ($B = 0$ T) with the laser on resonance with the quantum dot ($\delta = 0$). (b) Result of the auto-correlation measurement ($g^{(2)}$) as described in (a) evaluated for long time-scales. The $g^{(2)}$ is perfectly flat and stays close to one. (c) Configuration for an auto-correlation measurement with enhanced sensitivity to spin noise. This measurement is performed at a finite magnetic field ($B = 20$ mT) along the growth direction with the laser frequency centered between the two Zeeman peaks. (d) Result of the $g^{(2)}$ -measurement as described in (c) for long time-scales. The $g^{(2)}$ remains flat and close to one. (e) Configuration for an auto-correlation measurement with enhanced sensitivity to charge noise. This measurement is performed at zero magnetic field with the laser slightly detuned (by about half of the linewidth) with respect to the quantum dot resonance. (f) Result of the $g^{(2)}$ -measurement as described in (e). Here, a Rabi power similar to (b) is used. A bunching on a millisecond time-scale is observed, which can be attributed to charge noise.

Chapter 4

Driving the Radiative Auger Transition in GaAs Quantum Dots

This chapter is adapted from the following article:

Clemens Spinnler*, Liang Zhai*, Giang Nam Nguyen, Julian Ritzmann, Andreas D. Wieck, Arne Ludwig, Alisa Javadi, Doris E. Reiter, Paweł Machnikowski, Richard J. Warburton, and Matthias. C. Löbl*,
Optically driving the radiative Auger transition,
Nature Communications 12, 6575 (2021).

In a radiative Auger process, optical decay leaves other carriers in excited states, resulting in weak red-shifted satellite peaks in the emission spectrum. The appearance of radiative Auger in the emission questions whether the process can be inverted, such that an excitation corresponds to simultaneous photon absorption and electronic demotion. So far, such excitation of the radiative Auger transition has not been shown, neither on atoms nor on solid-state quantum emitters. In this chapter, we demonstrate the optical driving of the radiative Auger transition for the first time. We perform our experiments on a negative trion in the low-noise GaAs quantum dot. Radiative Auger and the fundamental transition form a Λ -system. On driving both transitions of this Λ -system simultaneously, we observe a reduction of the fluorescence signal by up to 70%. Our results reveal an optically addressable transition connecting few-body Coulomb interactions and quantum optics. The results open up the possibility of carrying out Terahertz spectroscopy on single quantum emitters with all the benefits of optics close to the visible regime: coherent laser sources, efficient and fast single-photon detectors. In analogy to optical control of an electron-spin, the Λ -system between the radiative Auger and the fundamental transitions points to optical control of the emitters' orbital degree of freedom.

4.1 Background

Non-radiative Auger processes have been observed in both atoms¹¹² and solid-state quantum emitters^{113,114}. They play an important role in determining the efficiency of semiconductor light-emitting diodes and lasers¹¹⁵. In the non-radiative Auger process, one electron reduces its energy by transferring it to a second electron that is promoted to a high-energy state. In the radiative Auger (shake-up) process, in contrast, one electron makes an optical decay, creating a photon. Part of the photon energy is transferred to a second electron such that the radiative Auger emission is red-shifted with respect to the main emission line. Both Auger and non-radiative Auger processes arise as a consequence of the Coulomb interactions between electrons in close proximity^{116–118}. The non-radiative Auger process is a purely Coulomb scattering process. On the contrary, the radiative Auger process involves both Coulomb scattering and electromagnetic (electron-photon) interactions. It can either be viewed as a higher-order scattering process or interpreted in terms of Coulomb-induced admixtures of higher single-particle states to the multi-electron wavefunction¹¹⁸. What appears to be an optical relaxation of one electron in the single-particle picture involves in fact a sudden change of the many-particle configuration.

Radiative Auger emission has been observed over a large spectral range: in the X-ray emission of atoms¹¹⁹; close to visible frequencies on donors in semiconductors¹²⁰ and quantum emitters^{38,121,122}; and at infrared frequencies as shake-up lines in two-dimensional systems^{123–127}. Furthermore, radiative Auger connects carrier dynamics to the quantum optical properties of the emitted photons³⁸, making it a powerful probe of multi-particle systems. Driving the fundamental transition between the electron ground state and an optically excited state is an important technique in quantum optics^{109,128}. In contrast, driving the radiative Auger transition has not been achieved on any atomic or semiconductor system. Success here would significantly increase the number of quantum optics techniques that can be employed.

We demonstrate driving the radiative Auger transition on a low-noise GaAs quantum dot (QD)³⁷. Without optical illumination, a single electron is trapped in the conduction band of the QD and occupies the lowest possible shell (the s -shell, $|s\rangle$). Upon resonant excitation of the fundamental transition, a second electron is promoted from the filled valence band to the conduction band and a negative trion X^{1-} ($|t\rangle$) is formed. This trion consists of two electrons in the conduction band and a hole in the valence band. Fig. 4.1(a) shows the possible optical decay paths: in the fundamental transition, one electron decays removing the valence band hole while the other electron remains in the

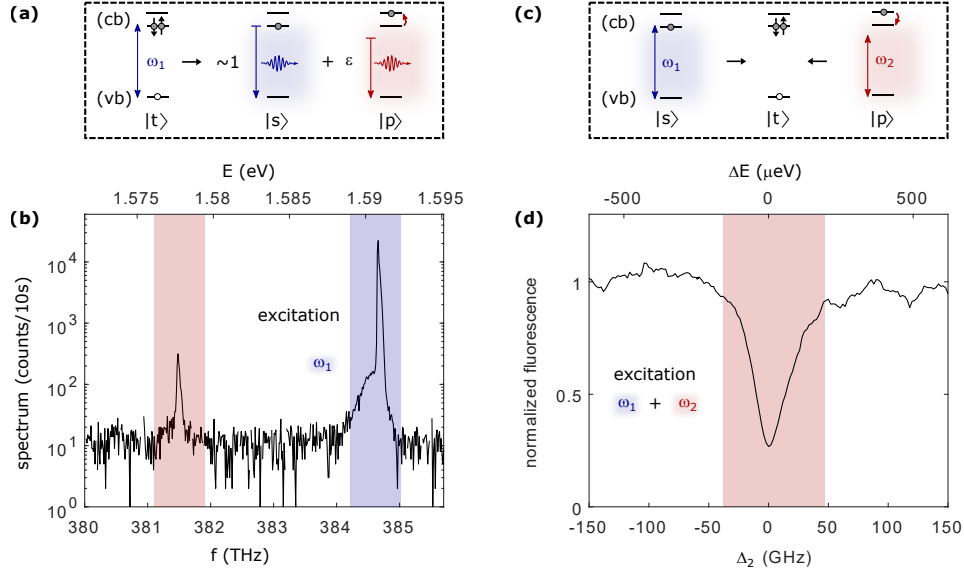


Fig. 4.1. **Radiative Auger emission and excitation of the radiative Auger transition.** (a) Schematic illustration of radiative relaxation processes of a negatively charged quantum dot (QD), a trion $|t\rangle$. With a near-unity probability, the trion state decays optically by recombination of an electron in the conduction band (cb) and a hole in the valence band (vb). In this case, the second electron either stays in its ground state (i.e. $|s\rangle$) – the fundamental transition. With only a small probability ϵ (in this case the process is a radiative Auger process), the second electron in the trion state is promoted to a higher shell (e.g. $|p\rangle$), resulting in red-shifted photon where part of the photon energy is transferred to the second (Auger) electron. (b) Emission spectrum from a negatively charged QD upon optical excitation at the fundamental transition. In addition to the resonance fluorescence at the position of the fundamental transition (highlighted in blue), there is a red-shifted satellite line (highlighted in red). This emission arises from the radiative Auger process; the intensity of the radiative Auger emission is around two orders of magnitude lower compared to the resonance fluorescence in this QD. (c) Two possible absorption channels in the presence of one confined conduction band electron. When the electron is in the ground state $|s\rangle$, a laser resonant with the fundamental transition (blue, frequency ω_1) excites a valence band electron and brings the system to the trion state, $|t\rangle$. When the conduction band electron is in an excited state $|p\rangle$, a red-shifted laser (frequency ω_2) can excite the system to the same trion state $|t\rangle$. In this inverted radiative Auger process, the missing energy is provided by the excited electron. (d) Resonance fluorescence from the fundamental transition in the presence of a strong second laser. When the second laser (ω_2) is on resonance with the radiative Auger transition ($\Delta_2 = 0$), the resonance fluorescence intensity is strongly reduced.

conduction band ground state $|s\rangle$; in the radiative Auger process, the remaining electron is left in an excited state $|p\rangle$. The emitted photon is red-shifted by the energy separation between $|p\rangle$ and $|s\rangle$ ^{38,116,122}. Figure 4.1(b) shows a typical emission spectrum from the trion decay. This spectrum is measured on resonantly driving the fundamental transition $|s\rangle\text{--}|t\rangle$ at 384.7 THz (1.591 eV) with a narrow-bandwidth laser³⁸. Red-shifted by 3.2 THz

(13.2 meV) from the fundamental transition, there is a weak satellite peak arising from the radiative Auger emission.

4.2 Inverting the Radiative Auger Process

Lasers at the radiative Auger frequency do not have sufficient energy to excite the fundamental transition $|s\rangle\text{--}|t\rangle$. Figure 4.1(c) illustrates a way how the trion state $|t\rangle$ can be excited with a laser at the Auger transition. In such a way, the missing energy is provided by the electron which initially occupies the excited state $|p\rangle$. However, driving the radiative Auger transition is experimentally challenging for two reasons: first, there is a fast non-radiative relaxation from the excited single-electron state $|p\rangle$ back to $|s\rangle$ ^{38,129}. The state $|p\rangle$ is not occupied at thermal equilibrium. Second, the dipole moment of the radiative Auger transition is small – it is difficult to achieve high Rabi frequencies on driving the transition. Furthermore, the small dipole moment also means that the radiative Auger emission is very weak: when driving the radiative Auger transition with a strong laser, it is hard to distinguish the radiative Auger emission from the back-reflected laser light.

Here, we rely on a two-colour experiment. We employ one laser (labelled as ω_1) to address the fundamental transition $|s\rangle\text{--}|t\rangle$ and a second laser (labelled as ω_2) to simultaneously drive the radiative Auger transition. This experiment has the following advantages: first, on driving $|s\rangle\text{--}|t\rangle$ with the ω_1 laser, there is a small chance of initialising the system in state $|p\rangle$ via the radiative Auger emission. Additionally, driving the $|p\rangle\text{--}|t\rangle$ -transition with the ω_2 laser, while transferring population to $|t\rangle$ with the ω_1 laser, also leads to a finite occupation of $|p\rangle$. Second, the small dipole matrix element of the radiative Auger transition is compensated by using high power for the ω_2 laser. The high power causes a high laser background when detecting the fluorescence from the radiative Auger transition. Instead, we tune the second laser over the Auger transition while measuring just the fluorescence originating from the fundamental transition $|s\rangle\text{--}|t\rangle$. Fig. 4.1(d) shows the result of this two-laser experiment. We observe a strong reduction in fluorescence on addressing the transition $|p\rangle\text{--}|t\rangle$ which is characteristic of two-colour excitation of a Λ -configuration. Our approach has a conceptual similarity to the driving of weak phonon-sidebands of mechanical resonators resulting in optomechanically induced transparency^{130,131}.

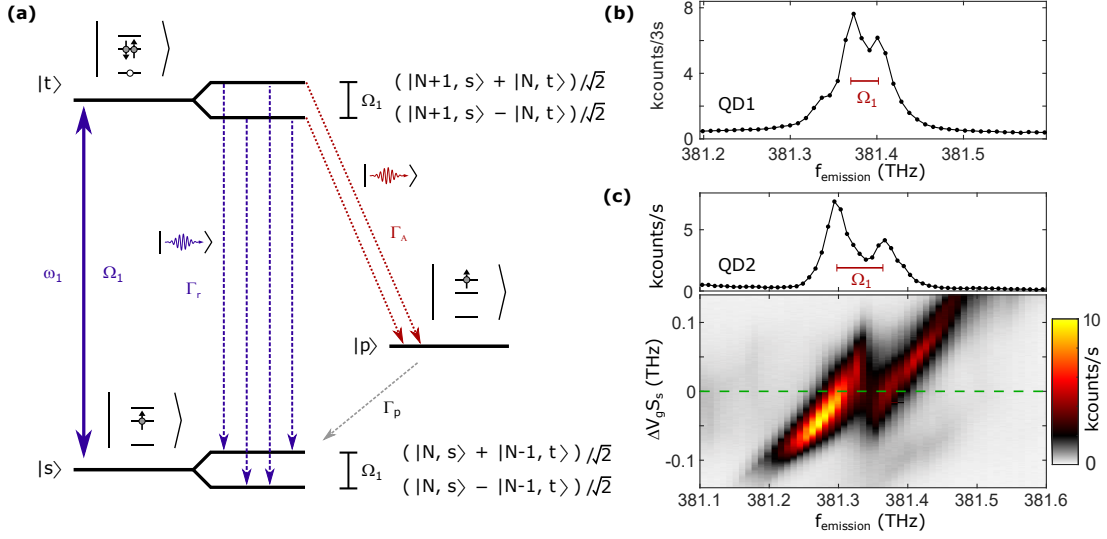


Fig. 4.2. **Autler-Townes splitting in the radiative Auger emission.** (a) Level scheme under strong resonant driving of the fundamental transition ($|s\rangle \rightarrow |t\rangle$). The energy levels are split into dressed states. The splitting between the dressed states is given by the Rabi frequency, Ω_1 . In the radiative Auger emission (red arrows), the dressed-state splitting enables two decay paths leading to an Autler-Townes splitting in the spectrum. (b) Radiative Auger emission from a GaAs quantum dot (QDa) on driving the transition $|s\rangle \rightarrow |t\rangle$ with the ω_1 laser. The Rabi frequency of $\Omega_1 = 2\pi \times 31.9$ GHz (red bar) is determined from a separate power saturation measurement. The measured Autler-Townes splitting in the emission matches the Rabi frequency. (c) Emission spectrum from another quantum dot (QDb), measured for a set of different detunings ($\Delta_1 = \Delta V_g \cdot S_s$) between fundamental transition and laser. The upper part of the plot is a line cut along the dashed green line at zero detuning ($\Delta_1 = 0$). In this case, the measured Autler-Townes splitting agrees with the independently determined Rabi frequency ($\Omega_1 = 2\pi \times 67.7$ GHz).

4.3 Autler-Townes Splitting in Radiative Auger Emission

We first consider the situation where the fundamental transition ($|s\rangle \rightarrow |t\rangle$) is driven by a strong laser. Since radiative Auger and fundamental transitions form a Λ -system, one would expect an Autler-Townes splitting in the radiative Auger emission. Fig. 4.2(a) illustrates the corresponding level scheme including the dressed states $\frac{1}{\sqrt{2}}(|N+1, s\rangle \pm |N, t\rangle)$ and $\frac{1}{\sqrt{2}}(|N, s\rangle \pm |N-1, t\rangle)$, where N is the photon number. The dressed-state splitting leads to a Mollow triplet in the resonance fluorescence^{109,132}. For a decay into a third level (e.g. $|p\rangle$), the Autler-Townes splitting¹³³ in the emission is expected to be Ω_1 . Fig. 4.2(b) shows the radiative Auger emission from one quantum dot (QDa). In this measurement, the laser is on resonance with the fundamental transition. The Rabi frequency [$\Omega_1 = 2\pi \times 31.9$ GHz, shown as the red bar in Fig. 4.2(b)] is estimated independently by measuring the fluorescence intensity as a function of laser power [see

Fig. 4.5(b)]. We observe an Autler-Townes splitting that agrees well with this Rabi frequency. For this QD, we also observe an additional weak emission appearing on the low energy side of the spectrum when using high Rabi frequencies [see Fig. 4.2(b) and Fig. 4.7]. We speculate that this emission is connected to optical coupling between $|p\rangle$ and an excited trion state, $|t^*\rangle$. Figure 4.2(c) shows radiative Auger emission from a second quantum dot (QDb). For QDb, we measure the radiative Auger emission as a function of detuning (see Fig. 4.7 for the corresponding measurement on QDa). On applying a gate voltage ΔV_g , the QD transition $|s\rangle-|t\rangle$ is detuned from the fixed laser by $\Delta_1 = \Delta V_g \cdot S_s$ via the quantum-confined Stark shift. S_s represents the Stark shift coefficient of the fundamental transition. At zero detuning, the observed Autler-Townes splitting also agrees well with the Rabi frequency obtained from an additional power saturation curve ($\Omega_1 = 2\pi \times 67.7$ GHz).

4.4 Driving Radiative Auger Transition in a Two-Colour Experiment

We now consider the two-colour experiments where the ω_2 laser is placed at the radiative Auger transition. Figure 4.3(a) shows the corresponding level scheme. We set the ω_1 laser to a modest power [$\Omega_1 = 2\pi \times 0.08$ GHz in comparison with the decay rate of the trion $\Gamma_r = 2\pi \times 0.50$ GHz]. The frequency of the radiative Auger transition is estimated from the emission spectrum [see Fig. 4.1(b)]. We sweep the frequency of the ω_2 laser and simultaneously monitor the resonance fluorescence intensity from the fundamental transition. Figure 4.3(b) shows the measurements for different powers of the ω_2 laser (placed around the radiative Auger transition). On increasing the laser power of ω_2 to several orders of magnitude higher than the power of ω_1 , there is a pronounced dip in the fluorescence intensity. This intensity dip appears precisely when the laser frequency ω_2 matches the radiative Auger transition ($|p\rangle-|t\rangle$) and is characteristic for a Λ -system that is driven with two lasers. We estimate the Rabi frequency Ω_2 driving $|p\rangle-|t\rangle$ by simulating the resonance fluorescence intensity as a function of Δ_2 (see Sec. 4.6.1 for the quantum optics simulation). In this simulation we keep the decay rate from $|p\rangle$ to $|s\rangle$ ($\Gamma_p \sim 2\pi \times 9.3$ GHz) fixed to the value that we determine from independent auto- and cross-correlation measurements³⁸ [see Fig. 4.6(d)]. The value of Ω_2 can be determined by a corresponding fit to the two-laser experiment. Additionally, we fit a constant pure dephasing, γ_p , for the state $|p\rangle$ which leads to an additional broadening of the fluorescence dip. We estimate $\gamma_p \sim 2\pi \times 8.8$ GHz from the fit and a Rabi frequency of $\Omega_2 = 2\pi \times 3.2$ GHz (the ω_2 laser) for the strongest fluorescence dip. Note that

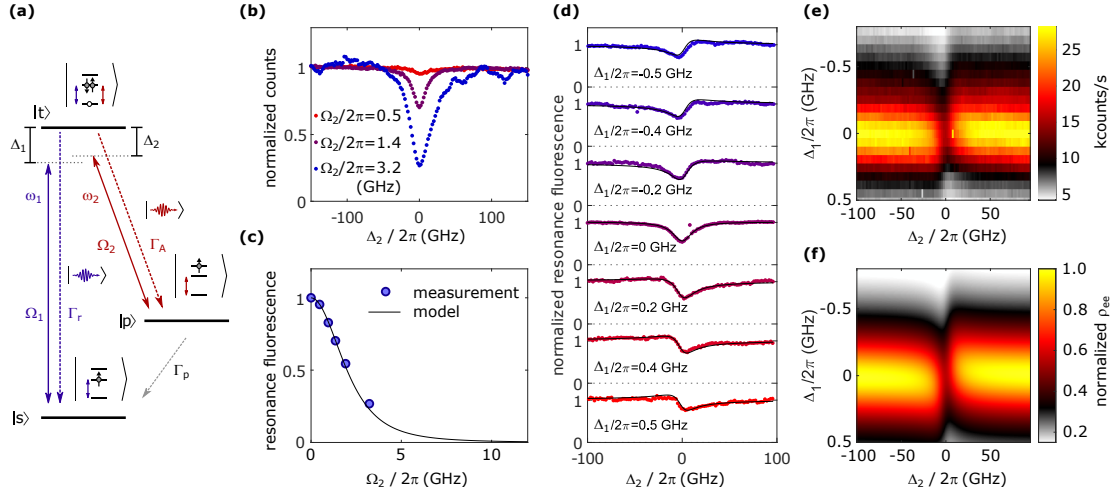


Fig. 4.3. **Optically driving the radiative Auger transition.** (a) The level scheme where one laser (denoted by ω_1) with Rabi frequency Ω_1 drives the fundamental transition ($|s\rangle-|t\rangle$) while a second laser (denoted by ω_2) drives the radiative Auger transition ($|p\rangle-|t\rangle$) with Rabi frequency Ω_2 . (b) Resonance fluorescence ($\Omega_1 = 2\pi \times 0.08$ GHz) as a function of detuning Δ_2 (detuning of the ω_2 laser). At low powers (small Ω_2), the resonance fluorescence intensity is almost constant for different values of Δ_2 . For the highest value of Ω_2 , the resonance fluorescence drops by up to $\sim 70\%$ on bringing ω_2 into resonance with the radiative Auger transition. This strong reduction in fluorescence intensity at a particular frequency is a characteristic feature of a two-laser driven Λ -system. When the lasers frequencies match the Λ -system transitions, a dip manifest. This is a direct evidence that the radiative Auger transition are optically addressable. (c) Resonance fluorescence at $\Delta_2 = 0$ as a function of Ω_2 . The resonance fluorescence intensity (blue dots) drops with increasing Ω_2 , fitting well to the theoretical model (black line). (d) Fluorescence intensity as a function of detuning Δ_2 . The Rabi frequencies are $\Omega_1 = 2\pi \times 0.27$ GHz, $\Omega_2 = 2\pi \times 2.1$ GHz. The same measurement is repeated for a series of fixed detunings Δ_1 (detuning of ω_1 from the fundamental transition). Detuning ω_1 leads to an asymmetric fluorescence dip. This asymmetry is well captured by the quantum optics simulations (black lines) based on the level scheme shown in (a). (e) Fluorescence intensity as a function of laser detunings Δ_1, Δ_2 . (f) Simulation of the fluorescence intensity as a function of the laser detunings.

additional excitation-induced dephasing via phonons is expected to be weak for such Rabi-frequencies¹³⁴.

In Fig. 4.3(c), we plot the minimum of the resonance fluorescence dip as a function of Ω_2 . The data fit well to a typical Λ -system driven by two lasers. For the highest value of Ω_2 , we achieve a reduction of the resonance fluorescence intensity by up to 70%. The depth of this reduction dip is limited by the power that we can reach in our optical setup. The measurement shows that resonance fluorescence can be switched on and off by using the radiative Auger transition. In our system, part of the fluorescence dip is due to the reduction of the overall absorption via the formation of a dark state. This effect is related

to electromagnetically induced transparency (EIT)¹³⁵ and coherent population trapping (CPT)¹³⁶. An additional reduction of the signal comes from the fact that there is a fast decay rate Γ_p from state $|p\rangle$ to $|s\rangle$. Thus, after the laser-induced transition from state $|t\rangle$ to $|p\rangle$, the system quickly decays to the ground state $|s\rangle$. This de-excitation channel reduces the population of the trion state and therefore the fluorescence intensity. We can distinguish the contribution of the two mechanisms by our quantum optics simulations. The density matrix element ρ_{tt} (occupation of state $|t\rangle$) is proportional to the overall fluorescence intensity. The term $\text{Im}(\rho_{st})$ (coherence between the states $|s\rangle$ and $|t\rangle$) is proportional to the absorption and reflects the coherent part of the intensity reduction. The contribution of both mechanisms varies but is comparable for the parameter regime in which we operate (see Methods Sec. 4.6.1).

The measurements so far were performed with the ω_1 laser on resonance ($\Delta_1 = 0$). We repeat the two-laser experiments while detuning the ω_1 laser frequency from the fundamental transition. Figure 4.3(d) shows the fluorescence intensity for positive, zero, and negative detuning Δ_1 . For non-zero detuning, the fluorescence dip is asymmetric as a function of Δ_2 . The asymmetry is an important result as it cannot be explained by a rate equation description, but depends on quantum coherence in a master-equation model. The full dependence of the resonance fluorescence intensity as a function of Δ_1 and Δ_2 is plotted in Fig. 4.3(e). This data set fits well to the corresponding quantum optics simulation in Fig. 4.3(f) using the parameters from the previous measurements.

4.5 Summary

In this chapter, we show that the radiative Auger process is reversible. The resonance fluorescence is strongly reduced when addressing the radiative Auger transition. Such an intensity manipulation allows a modulated laser on the radiative Auger transition to be used for fast optical gating of the emitter's absorption. As an outlook, we suggest that an effective coupling between the orbital states, split by frequencies in the terahertz band, can be created by two lasers at optical frequencies. The idea here is to establish a Raman-like process: the lasers are equally detuned from their resonances and an exciton is not created. This scheme facilitates control of the orbital degree of freedom with techniques that have been developed for manipulating spin-states^{136,137}. Further quantum optics experiments with radiative Auger photons are conceivable: adding a third laser with a terahertz-frequency at the transition¹²⁹ $|s\rangle$ - $|p\rangle$ might allow close-contour driving schemes¹³⁸. In analogy to experiments on spins⁸², the radiative Auger process could lead to an entanglement between the frequency of the emitted photon and

the orbital state of the Auger electron.

4.6 Methods

4.6.1 A three-level model for quantum optics simulations

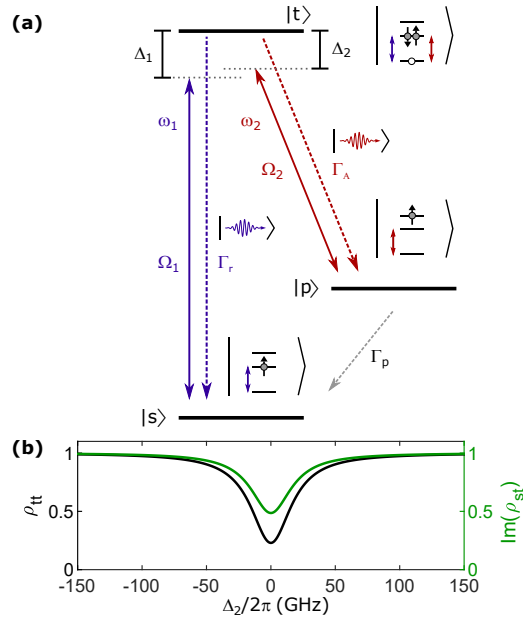


Fig. 4.4. **The three-level model.** (a) Fundamental transition and radiative Auger transition form a Λ -system where each transitions can be driven by an independent laser. The Rabi-frequency of the laser on the fundamental transition (ω_1) is given by Ω_1 , the Rabi frequency of the laser on the radiative Auger transition (ω_2) is given by Ω_2 . The corresponding laser detunings are Δ_1 and Δ_2 ; and the corresponding spontaneous decay rates from the trion state $|t\rangle$ are Γ_r (fundamental transition), Γ_A (radiative Auger transition). The parameter Γ_p is the relaxation rate from the electron excited state $|p\rangle$ to the electron ground state $|s\rangle$. (b) Comparison of the density matrix elements ρ_{tt} and $\text{Im}(\rho_{st})$ as a function of Δ_2 . The parameters are identical to those used to describe the lowest fluorescence dip shown in Fig. 4.3(b).

The level scheme to describe the two-laser experiments is described in detail in Fig. 4.4(a). It consists of the electron ground state $|s\rangle$, an excited electron state $|p\rangle$, and the trion state $|t\rangle$. The laser driving the fundamental transition is labelled as ω_1 and the laser driving the radiative Auger transition is labelled as ω_2 . The corresponding Rabi frequencies are given by Ω_1 , Ω_2 and the detunings of the lasers from the corresponding transition are Δ_1 , Δ_2 . The spontaneous decay rates are the decay rate via the fundamental transition (Γ_r), the decay rate via radiative Auger (Γ_A), and the p -to- s decay rate (Γ_p). We simulate the system with a standard quantum optics approach. Making

the dipole and the rotating-wave approximations, the Hamiltonian of the system is given by¹³⁶:

$$\begin{aligned} \hat{H} = & \frac{\hbar}{2}[2(\Delta_2 - \Delta_1) |p\rangle \langle p| - 2\Delta_1 |t\rangle \langle t| \\ & + \Omega_1 |t\rangle \langle s| + \Omega_2 |t\rangle \langle p| + \Omega_1 |s\rangle \langle t| + \Omega_2 |p\rangle \langle t|]. \end{aligned} \quad (4.1)$$

The Hamiltonian describes the coherent evolution of the system. The incoherent decay paths are taken into account by the Lindblad collapse operators for the spontaneous emission from the fundamental transition ($L_1 = \sqrt{\Gamma_r} |s\rangle \langle t|$), the spontaneous radiative Auger emission ($L_2 = \sqrt{\Gamma_A} |p\rangle \langle t|$), the p -to- s relaxation ($L_3 = \sqrt{\Gamma_p} |s\rangle \langle p|$), and the p -shell dephasing ($L_4 = \sqrt{\gamma_p} |p\rangle \langle p|$). The dynamics of the system are described by the following master equation:

$$i\hbar \frac{d\rho}{dt} = [\hat{H}, \rho] + i\hbar \sum_i \left(L_i \rho L_i^\dagger - \frac{1}{2} \{L_i^\dagger L_i, \rho\} \right), \quad (4.2)$$

where ρ is the density matrix. Using this equation, we determine the steady state of the system ($\frac{d\rho}{dt} = 0$). The steady state occupation of the trion state is used for simulating the experiments as it is proportional to the fluorescence intensity.

This simulation fits well to our experimental results in Fig. 4.3. We also use it to estimate the Rabi frequency Ω_2 and the dephasing γ_p : when Δ_2 is close to zero, the resonance fluorescence depends on Ω_2 . Due to the small dipole moment of the radiative Auger transition, strong laser power is used for high values of Ω_2 . For the strongest power of the ω_2 laser, we estimate $\Omega_2 = 2\pi \times 3.2$ GHz from the simulation. Alternatively, one could estimate the ratio of the corresponding dipole moments by using the intensity ratio between resonance fluorescence and radiative Auger emission ($\sim 50 : 1$). Ω_2 could then be obtained by using this estimation together with the power saturation curve of the resonance fluorescence. We find that this method underestimates Ω_2 compared to the simulation. Since effects such as chromatic aberration make this second approach more prone to systematic errors, we use the two-colour experiment and the corresponding simulation to determine Ω_2 . The dephasing term γ_p is also estimated by simulating the two-colour experiments. We find that it mainly affects the width of the fluorescence dip. The other parameters ($\Gamma_r, \Gamma_p, \Omega_1$) are determined from independent measurements and kept fixed in the simulation.

Two mechanisms contribute to the fluorescence reduction when driving the Auger transition with the ω_2 laser: a coherent part related to EIT/CPT and dark-state formation¹³⁵, an incoherent part due to a fast de-excitation channel from $|t\rangle$ to $|p\rangle$ by the

radiative Auger process and from $|p\rangle$ to $|s\rangle$ by two-phonon emission¹²⁹. The incoherent decay path is irrelevant in systems where the ground state lifetime is long¹³⁵. To distinguish these two mechanisms we compare the density matrix element ρ_{tt} (proportional to the overall fluorescence signal) to $\text{Im}(\rho_{st})$ (proportional to susceptibility). The susceptibility determines the system's absorption¹³⁵ and is associated with the coherent contribution of the fluorescence reduction. In Fig. 4.4(b) we plot ρ_{tt} and $\text{Im}(\rho_{st})$ as a function of Δ_2 . This comparison shows that the coherent contribution to the fluorescence reduction (EIT/CPT mechanism) is only part of the overall fluorescence reduction.

4.6.2 Experimental techniques

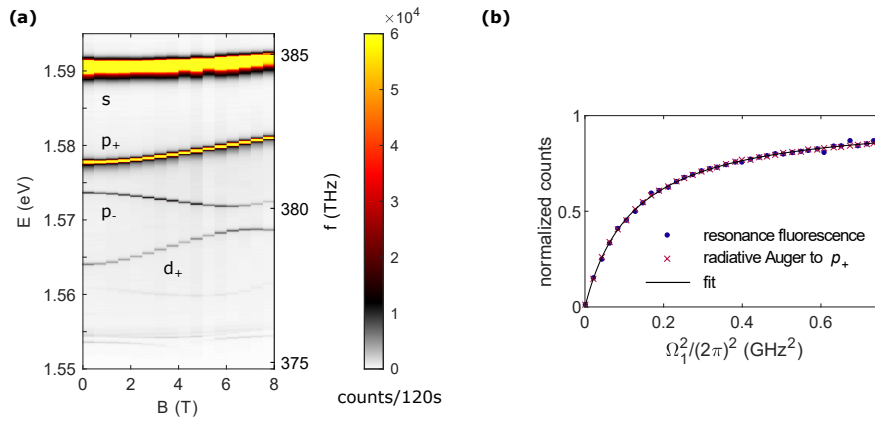


Fig. 4.5. **Magnetic field dependence of the different emission lines.** (a) Resonance fluorescence from the fundamental transition and radiative Auger emission as a function of the magnetic field B (data from QDa). The strong magnetic field dispersion of the radiative Auger emission enables direct identification of the final electron states of the Auger electron. (b) Normalised fluorescence intensity of the different emission channels as a function of Rabi frequency Ω_1 . This is a single-laser experiment: the ω_2 laser is off. The power dependence of the radiative Auger intensity coincides with that of the resonance fluorescence from the fundamental transition and matches the power curve of a two-level system. From a fit to the power curve we determine the relationship between the Rabi frequency Ω_1 and the actual power used in the measurements. For the fitting, the radiative decay is fixed to a value that we determine from an independent lifetime measurement ($\Gamma_r = 2\pi \times 0.50$ GHz)^{37,72}.

For all our measurements, the low-noise GaAs QD sample is kept in a liquid helium bath cryostat at 4.2 K. The decay rates Γ_r of GaAs QDs [typically in the range $2\pi \times (0.5 - 0.6)$ GHz] were determined by lifetime measurements using pulsed resonant excitation³⁷. The decay rate of the radiative Auger transition, $\Gamma_A \sim \Gamma_r/100$, is estimated by comparing its emission intensity to the fundamental transition. QDa is identical to the second QD in Ref. 37 (the same as QDB in Chapter 3). The QDs presented in this

chapter have a stronger radiative Auger emission compared to InGaAs QDs³⁸ indicating a stronger dipole-moment of the radiative Auger transition. We use radiative Auger lines where the final state of the Auger electron, $|p\rangle$, is a QD p -shell. In particular, we investigate the transition associated with the lower p -shell (p_+) for QDa and the higher p -shell (p_-) for QDb. We can assign further emission lines to the corresponding higher electronic shells by measuring the magnetic field dispersion of the emission spectrum³⁸ [see Fig. 4.5(a)].

To excite the QDs, we use a tunable CW laser with a narrow bandwidth. Resonant excitation is not necessary for the observation of the radiative Auger emission: above-band excitation is also effective^{118,121}. It is also possible to observe radiative Auger on systems that suffer from more charge noise than ours¹²¹. However, resonant excitation has the advantage that no continuum states are excited making it easier to identify all emission lines, and low charge noise makes resonant excitation a lot easier to perform. For this chapter, resonant excitation and the low level of noise are crucial to optically addressing single radiative Auger transition.

4.6.3 Time-resolved correlation measurements

To determine the relaxation rate Γ_p ($\sim 2\pi \times 9.3$ GHz) from $|p\rangle$ to $|s\rangle$, we exploit a technique developed in Ref. 38: on driving $|s\rangle-|t\rangle$ ($\Omega_2 = 0$), we measure an auto-correlation of the resonance fluorescence from the fundamental transition, and subsequently compare it to the cross-correlation between the resonance fluorescence and the radiative Auger emission. The corresponding measurement setups are shown in Fig. 4.6(a,b). To resolve the auto- and cross-correlations with high time-resolution, we use two superconducting nanowire single-photon detectors (SingleQuantum, timing jitter of 10 ps) in combination with a time-to-digit converter (Swabian Instruments, Time Tagger Ultra).

Compared to the auto-correlation, the cross-correlation has a small time offset when a radiative Auger photon is followed by a photon from the fundamental transition [see Figs. 4.6(d)]. This time scale corresponds to the relaxation time, $\tau_p = 1/\Gamma_p$, describing the relaxation from $|p\rangle$ to $|s\rangle$. The relaxation time appears in the cross-correlation: when a radiative Auger event is detected by the first detector, there is an additional waiting time of τ_p before the excited Auger electron relaxes to the ground state and the system can be optically re-excited. Therefore, it takes longer before a second photon is detected. The additional waiting time is only present for the cross-correlation. For the auto-correlation, the system decays directly to the ground state $|s\rangle$ and there is no additional waiting time.

As shown in Fig. 4.6(e), the theoretical model fits well to the data. In these measure-

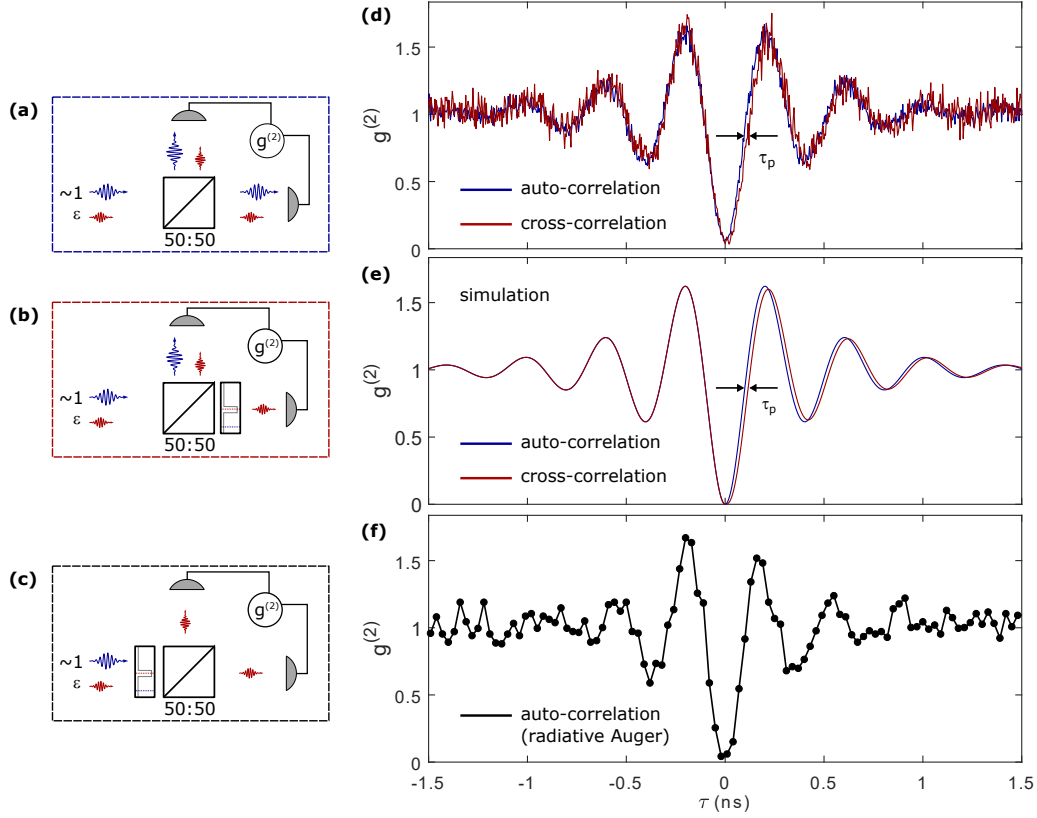


Fig. 4.6. **Time-resolved correlation measurements.** (a) Schematic measurement setup for the auto-correlation of resonance fluorescence. (b) Schematic setup for the cross-correlation between resonance fluorescence and radiative Auger emission. (c) Schematic setup for the auto-correlation of the radiative Auger emission. (d) Comparison between the auto-correlation of the resonance fluorescence (blue) and the cross-correlation (red, data from QDa). Both correlation measurements are performed with a single laser on the fundamental transition and show Rabi oscillations due to the strong driving (Ω_1). The cross-correlation (between the resonance fluorescence and the radiative Auger emission) has a small offset given by the $|p\rangle$ -to- $|s\rangle$ relaxation time ($\tau_p = 1/\Gamma_p = 17$ ps). This offset measures the finite time for which the Auger electron remains in the excited state after a radiative Auger process has occurred³⁸. (e) Results of the quantum optics simulations for auto- and cross-correlations. The simulations match well with our experimental data. (f) Auto-correlation of the radiative Auger emission. Since the radiative Auger emission is relatively weak (count rates: 630 Hz on the first, 530 Hz on the second detector), a long integration time (~ 50 h) is needed to resolve the Rabi oscillations in this measurement. The excitation power and Rabi frequency are slightly different with respect to the auto- and cross-correlation shown in (d).

ments, only a single laser at ω_1 is used. The system is described by Eqs. 4.1 and 4.2, with the parameter Ω_2 set to zero. We use the Quantum Toolbox in Python¹⁰⁸ (QuTiP) to compute the steady-state density matrix. With the resulting density matrix, we then

compute the auto- and the cross-correlation. The auto-correlation is:

$$g^{(2)}(\tau) = \frac{\langle \hat{a}^\dagger(t) \hat{a}^\dagger(t+\tau) \hat{a}(t+\tau) \hat{a}(t) \rangle}{\langle \hat{a}^\dagger(t) \hat{a}(t) \rangle^2}, \quad (4.3)$$

and the cross-correlation is:

$$g_{\text{cro}}^{(2)}(\tau) = \frac{\langle \hat{a}_A^\dagger(t) \hat{a}^\dagger(t+\tau) \hat{a}(t+\tau) \hat{a}_A(t) \rangle}{\langle \hat{a}^\dagger(t) \hat{a}(t) \rangle \langle \hat{a}_A^\dagger(t) \hat{a}_A(t) \rangle}. \quad (4.4)$$

In both cases, t is the time and τ is the time delay between two subsequently detected photons. \hat{a}^\dagger describes the creation of a photon via the fundamental transition, and \hat{a}_A^\dagger describes the creation of a photon via the radiative Auger transition.

Finally, we also measure the auto-correlation of the radiative Auger emission [see Fig. 4.6(c) for the setup]. The measurement is shown in Fig. 4.6(f). We observe a pronounced anti-bunching at zero delay proving the single-photon nature of the radiative Auger photons. We also observe the Rabi oscillation from strongly driving the transition $|s\rangle-|t\rangle$ in the photon-statistics of the radiative Auger photons from the transition $|p\rangle-|t\rangle$.

4.6.4 Magnetic Field Dispersion of the Emission

The magnetic field dispersion of the radiative Auger emission is significantly stronger than that of the emission from the fundamental transition [see Fig. 4.5(a)]. The reason is the different final states after the optical decay: the electron ground state $|s\rangle$ (s -shell) has a weak magnetic field dispersion and, in contrast, higher shells such as the excited state $|p\rangle$ (p -shell) have a much stronger dependence on the magnetic field. Since the optical emission energy is given by the energy of the trion minus the energy of the final state, the strong magnetic field dispersion is transferred to the radiative Auger lines. The strong dispersion of the radiative Auger emission is an important feature allowing it to be distinguished unambiguously from phonon replicas. For a two-dimensional harmonic confinement potential, the magnetic field dispersion of the different shells form the Fock-Darwin spectrum. The dispersion of the radiative Auger emission is, therefore, typically close to an inverted Fock-Darwin spectrum³⁸.

4.6.5 Further Measurements of Autler-Townes splitting

In Fig. 4.7 we show further measurements of the Autler-Townes splitting on QDa. The measurements are performed for different Rabi frequencies Ω_1 and the detuning Δ_1 between the laser and fundamental transition is varied. The QD transitions are detuned

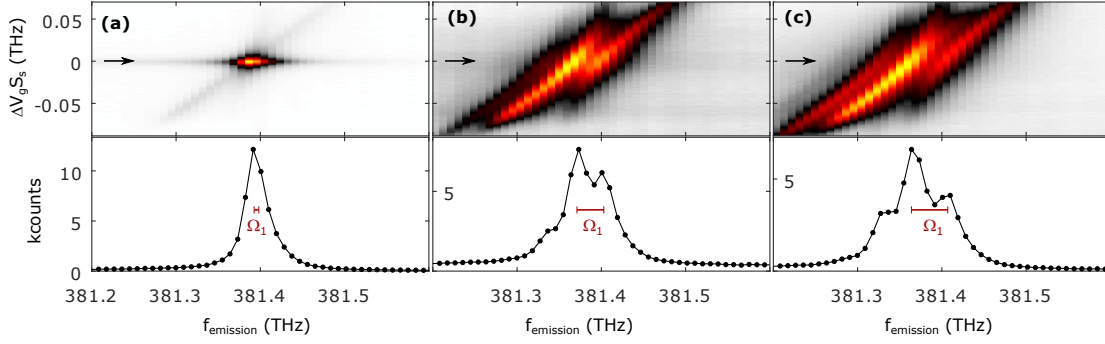


Fig. 4.7. **Radiative Auger emission upon excitation of the fundamental transition.** (a) Radiative Auger emission from QDa [see also Fig. 4.2(b)]. The emission frequency (x-axis) is plotted as a function of detuning between laser and the $|s\rangle - |t\rangle$ transition (y-axis). In the measurements shown here, the Autler-Townes splitting is not resolved since the Rabi frequency is too small ($\Omega_1 = 2\pi \times 5.5$ GHz). (b, c) The same measurements as before performed at higher Rabi frequencies ($\Omega_1 = 2\pi \times 31.9$ GHz, $\Omega_1 = 2\pi \times 43.2$ GHz) where the Autler-Townes splittings are resolved.

from the fixed laser by applying a gate voltage, V_g . The detuning from the fundamental transition is $\Delta V \cdot S_s$, where S_s is the Stark-shift of the fundamental transition and ΔV_g is the difference in gate voltage. The Rabi frequencies at zero laser detuning are independently determined from a power saturation curve (red bars in Fig. 4.7). They match the measured Autler-Townes splittings in the emission spectra. Furthermore, on detuning the QD resonance from the laser ($\Delta V_g \neq 0$), there is a small probability to excite the trion via the phonon sideband giving rise to a weak “diagonal” emission line. In the case of a red-detuned QD ($\Delta V_g < 0$), the laser has more energy than the QD transition and the additional energy can be transferred to LA-phonons. In the case of a blue-detuned QD, the laser energy is too small and the missing energy can be provided by phonon absorption.

Chapter 5

Nuclear-Spin Polarisation in Low-Noise GaAs Quantum Dots

5.1 Background

Self-assembled semiconductor quantum dots (QDs) are a promising resource of single photons^{7,11,36,81}. Single photons can travel over long distances, transferring quantum information between remote QDs. QDs are also hosts of single electron-spins^{3,37,103}. The electron spin in a QD interacts with a large number of nuclear spins. On the one hand, the interaction with nuclear spins is a dominant dephasing mechanism of the electron spin⁴⁰; on the other hand, via optically addressable electron spins, the interaction allows access to a long-lived mesoscopic nuclear ensemble, a potential resource for quantum information processing^{88,139}.

Electron-nuclear spin interaction has been extensively studied for InGaAs QDs under both resonant and non-resonant excitation. Compared to the non-resonant excitation, exciting QDs resonantly enables the creation of highly indistinguishable single photons^{7,11} and a deterministic spin-photon interface¹⁴⁰. Under resonant excitation, noncollinear hyperfine interaction plays an important role in the electron-nuclear spin coupling^{41,88,139,141}. The noncollinear hyperfine interaction stems mostly from the quadrupole effect⁴¹ induced by the intrinsically inhomogeneous strain in the QD environment. This quadrupolar interaction is at the origin of bidirectional dynamic nuclear-spin polarisation (DNSP), which complicates the optical resonance of InGaAs QDs. For example, the spectral lineshape of an InGaAs QD deviates from a standard Lorentzian profile at a high magnetic field and exhibits hysteresis with respect to the sweeping direction of the excitation laser frequency^{41,42}. On the other hand, utilising the quadrupolar interaction enables techniques to manipulate nuclear spins, allowing nuclear-spin cooling and collective nuclear-spin excitation^{25,88}.

Compared to the well-established InGaAs QDs, GaAs QDs have also lately emerged

as promising candidates for single-photon and single-spin applications. GaAs QDs are grown in the AlGaAs matrix – the lattice mismatch in the system is $< 0.05\%$. Thus, GaAs QDs are almost strain-free^{15,72}, and the nuclear quadrupolar field is expected to be strongly suppressed. Moreover, GaAs QDs do not contain indium nuclei, thus having more homogeneous nuclear spins compared to InGaAs QDs – all nuclei (Ga and As) have a nuclear spin of $I = 3/2$. Both a reduced quadrupolar field and more homogeneous nuclear spins promise a more coherent electron spin in GaAs QDs. However, the reduced quadrupolar coupling also limits the tool for nuclear spin manipulation. Such a limitation calls for a better understanding of the electron-nuclear spin dynamics in strain-free GaAs QDs under resonant conditions. So far, experimental studies have been missing. This is partially due to the lack of charge-state control in GaAs QDs.

In this chapter, we investigate interactions between an electron spin and its surrounding nuclear spins by probing the optical spectrum in a low-noise GaAs QDs platform^{36,37}. We show that, under single-laser resonant excitation, DNSP is either small or not present, which is an evidence of strongly suppressed quadrupolar interaction in strain-free QDs. Adding an additional laser field, bidirectional DNSP emerges in the recovery plateau (under two-laser driving, the QD signal recovers from spin pumping, see Fig. 3.3). The bistability of such DNSP can be erased by electron-spin randomisation. Yet, the nature of nuclear-spin effects depends drastically on whether the blue- or red-Zeeman recovery plateau is addressed: while the blue-Zeeman recovery plateau exhibits locking of the electron-spin in an optical dark-state due to coherent population trapping^{142–144} (CPT), the nuclear spins ensure that the CPT resonance is avoided on the red-Zeeman branch.

5.2 One-Colour Experiment: Suppressed Quadrupolar Interaction

The GaAs QDs are placed in a magnetic field $B = 5.6$ T along the growth direction (Faraday configuration). We charge a QD with an additional electron, creating a negative trion (X^{1-}). Resonance fluorescence plateau are mapped out in Fig. 5.1(a) as functions of external gate voltage V_g and the excitation laser frequency f_{scan} . At the centre of the plateau, the resonance fluorescence intensity is ~ 10 times lower than that at the edge of the plateau due to the successful spin pumping. At the two ends of the plateau, resonance fluorescence is bright because of the electron co-tunnelling. At both ends, the trion transition is split into four lines¹⁰³ – the two dimmer lines in the middle originates from the diagonal transitions ($|\uparrow\rangle - |\uparrow\downarrow\downarrow\rangle$ and $|\downarrow\rangle - |\uparrow\downarrow\uparrow\rangle$), which are surrounded by two brighter lines that corresponds to the vertical transitions ($|\uparrow\rangle - |\uparrow\downarrow\uparrow\rangle$ and $|\downarrow\rangle - |\uparrow\downarrow\downarrow\rangle$).

The diagonal transitions are weaker compared to the vertical ones (intensity ~ 4 times lower), but they are still optically allowed which is likely due to the heavy- and light-hole mixing^{62,101}.

At a fixed laser frequency, the spectrum of the X^{1-} resonance is resolved by bidirectionally scanning V_g at a slow speed. Shown in Fig. 5.1(b-e) are the scans at different plateau positions that are marked in (a). In every scan, the step size of V_g corresponds to $0.3 \mu\text{eV}$ in frequency (equivalently 60 MHz, that is $\sim 1/10$ of the spectral linewidth); the excitation power corresponds to $\Omega = 1.7 \Gamma$ (Γ is the radiative decay rate of X^{1-} , $\Gamma = 3.5$ GHz). In such conditions, the incident laser routinely leads to bidirectional nuclear spin polarisation via large quadrupolar fields in strained QDs, resulting in bistability depending on the scan directions and modifications of the QD lineshape^{40-42,141}. In strain-free GaAs QDs, the bistability is not well observed: at either the centre [Fig. 5.1(b,c)] or the edge [Fig. 5.1(d,e)] of the charge plateau, on either the blue-Zeeman [Fig. 5.1(b,d)] or red-Zeeman [Fig. 5.1(c,e)] branch, the spectrum of X^{1-} stays mostly invariant when reversing the V_g -scan direction (orange and blue colours represent different V_g -scan directions). One way to interpret the absence of bistability is a strongly suppressed quadrupolar-field-induced noncollinear interaction in strain-free GaAs QDs. In other words, we assume that for an electron-nuclear spin state, e.g. $|\uparrow\rangle \otimes |m_I\rangle$, the coupling rate to $|\uparrow\downarrow\uparrow\rangle \otimes |m_I \pm 1\rangle$ states is negligible (with $\hat{I}_z |m_I\rangle = m_I |m_I\rangle$); the same for the coupling of $|\downarrow\rangle \otimes |m'_I\rangle$ and $|\uparrow\downarrow\downarrow\rangle \otimes |m'_I \pm 1\rangle$ states). A single resonance laser (of moderate power) acting on a single electron-spin ground state barely induces nuclear-spin polarisation to the system.

In the co-tunnelling region, when the laser addresses the vertical transitions of the X^{1-} (stronger peaks) the lineshape resembles a typical Lorentzian profile, as is visible in Fig. 5.1(d,e). When the laser addresses the diagonal transitions (weaker peaks), the X^{1-} lineshape is not Lorentzian anymore, which is likely influenced by the electron-nuclear spin interaction. On the blue-Zeeman branch, the spectrum of the diagonal transition has a near-triangle shape, while on the red branch, the spectrum shows a flat top. However, the lineshapes remain almost unchanged when the V_g -scan direction is reversed. The lineshape modification is likely a consequence of the optically induced flip-flop process assisted by emission and absorption in the diagonal transition^{42,145}.

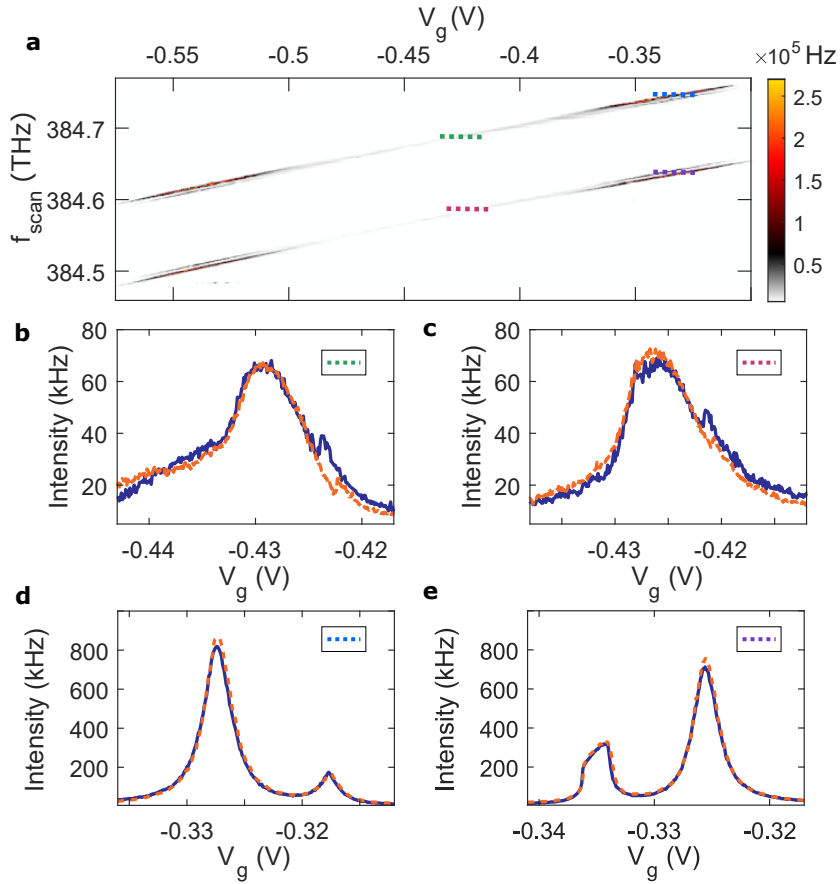


Fig. 5.1. **Resonance fluorescence from a GaAs quantum dot in a magnetic field.** (a) Plateau of resonance fluorescence from the negative trion. The frequency shift versus the external gate voltage V_g allows a Stark-shift coefficient $\partial f_{\text{QD}}/\partial V_g = 0.63$ THz/V to be calculated. At both ends of the plateau, four optical transitions are resolved. The distance between the transitions allows the electron and hole g -factors to be determined: $g_e = -0.074 \pm 0.009$, $g_h = 1.337 \pm 0.063$. (b-e) Resonance fluorescence spectrum as a function of gate voltage V_g at different plateau positions. The positions are marked with the corresponding colours in (a). For (b,c), the scans take place at the plateau centre, and for (d,e) close to the plateau edges. In all four plots, V_g is swept bidirectionally – blue lines represent the scan direction from right to left (“forward”); and the orange lines from left to right (“backward”). In the centre of the plateau, the QD signal becomes relatively weak due to successful spin pumping. On both Zeeman branches, the spectrum in forward and backward directions almost overlap with each other: no bistability. At the edges of the plateau, there are two peaks on either of the Zeeman branches. The peak with stronger intensity corresponds to the spin-preserving vertical transition, which leaves the electron spin state unchanged; the weaker peak represents the diagonal transition, which is assigned with a spin-flip. The spectra of vertical transitions at plateau edges resemble Lorentzian profiles, while the spectra of diagonal transitions are slightly modified by nuclear spins.

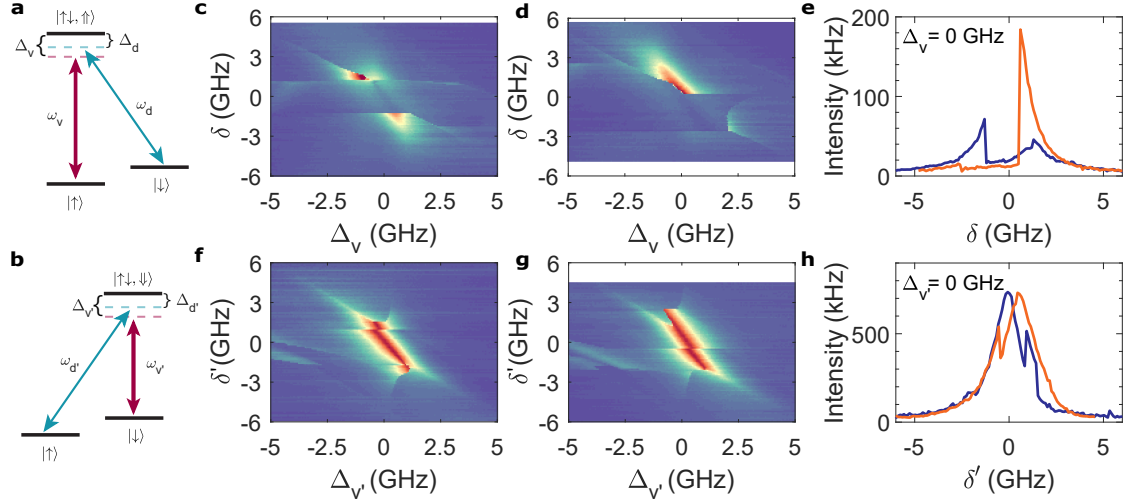


Fig. 5.2. **Bistability with two-colour excitation.** (a, b) Effective Λ -schemes for the blue-Zeeman and red-Zeeman branches. In both cases, the vertical transition (spin-preserving) is ~ 4 times stronger than the diagonal one (spin-flip), $\Gamma_{v(\prime)} = 4 \Gamma_{d(\prime)}$. A fixed-frequency laser ($\omega_{v(\prime)}$) is employed to drive the vertical transition, while another laser (of the same strength, $\omega_{d(\prime)}$) is swept across the diagonal transition. The detunings are labelled as $\Delta_{v(\prime)}$ and $\Delta_{d(\prime)}$ for the vertical and diagonal transitions, respectively. Relative detuning of the two driving field is defined as $\delta^{(\prime)} = \Delta_{d(\prime)} - \Delta_{v(\prime)}$. (c, d) Recovery plateau of X^{1-} when both lasers are close to the resonance condition on the blue-Zeeman branch. The excitation laser power corresponds to a Rabi frequency of $\Omega = 1.7 \Gamma \sim 2.1 \Gamma_v$. In (c), the gate voltage is scanned in the forward direction, while in (d), in the backward direction. The resulting recovery plateau shows bistability depending on the scan direction. (e) Spectrum of the QD resolved in δ when $\Delta_v = 0$. The scan in the forward (backward) direction is coloured blue (orange). (f, g) Recovery plateau of X^{1-} on the red-Zeeman branch. The excitation power is the same as in (c, d). The gate voltage is scanned in the forward direction in (f) and in the backward direction in (g). (h) QD fluorescence on the red-Zeeman branch as a function of δ' when $\Delta_{v'} = 0$. Instead of the dimmed regions shown in (e), the bistability is revealed as a “distortion”. Similarly, the scan in the forward (backward) direction is coloured blue (orange).

5.3 Two-Colour Experiment: Dynamic Nuclear-Spin Polarisation

In the following, we show that by adding an additional laser to the system, i.e., a two-colour experiment, the nuclear spins can be polarised.

In GaAs QDs, since the electron g -factor ($g_e = -0.07$) is very small compared to that of the hole ($g_h = 1.34$), the two excited-state levels of X^{1-} (split by the hole spin’s Zeeman energy) are far apart – the four-level system is equivalently two Λ -systems [see Fig. 5.2(a,b)]. We keep the additional laser fixed in frequency (red arrows, either on

the blue-Zeeman or the red-Zeeman branch) and sweep the frequency of another laser (blue arrows). In the meantime, the gate voltage V_g is scanned bidirectionally for every laser frequency. Here, the V_g -range is restricted to the plateau centre (spin-pumping region). When both lasers approach the resonance of the Λ -system, we observe the recovery of resonance fluorescence (see also the Methods section). In Fig. 5.2(c,d) the recovery plateau on the blue-Zeeman branch is presented depending on the V_g -scan direction. Here, detuning between the fixed-laser frequency and the vertical transition Δ_v is plotted on the x -axis instead of V_g . In Fig. 5.2(c) we sweep V_g thereby changing Δ_v from negative to positive values; while in (d) the Δ_v -scan direction is reversed. In stark contrast to the one-colour experiments, the resulting spectra of the recovery plateau of different scan directions are very different. The general feature is a dark region in the middle of the recovery plateau. Yet, the width, the shape, and the position of the dark region depend on the scan direction, a bistability. For direct comparison, we overlap the spectra of both directions when the fixed-laser is in resonance with $|\uparrow\rangle$ - $|\uparrow\downarrow\uparrow\rangle$ transition [$\Delta_v = 0$, see Fig. 5.2(e)]. At certain positions (scan-direction related) the QD enters abruptly into a dark state where the fluorescence intensity is reduced to near-zero. Such a dark state is a signature of coherent population trapping in a Λ -system¹⁴²⁻¹⁴⁴. However, unlike the standard CPT, the dark state can be locked (due to the electron-nuclear spin interaction) for a broad two-photon detuning range, which is about $2\pi \times 2.6$ GHz ($2\pi \times 3.3$ GHz) or equivalently $\sim 7 \Gamma_v$ ($9 \Gamma_v$) for the forward (backward) scan. The maximum range of the dark-state formation for forward (backward) scan [Fig. 5.2(c)/(d)] is around $2\pi \times 3.3$ GHz ($2\pi \times 5.2$ GHz) at $\Delta_v > 2\pi \times 2.5$ GHz ($\Delta_v < -2\pi \times 2.5$ GHz).

When the lasers address the red-Zeeman branch, the recovery plateau is visible as in Fig. 5.2(f,g). The dark region disappears on the red-Zeeman branch: the CPT condition cannot be met. Instead, the effect of nuclear-spin polarisation manifests itself as a “distortion” in the recovery plateau. The position of such distortion varies depending on the scan direction. Bidirectional scans when $\Delta_{v'} = 0$ (the fixed-laser at resonant with $|\downarrow\rangle$ - $|\uparrow\downarrow\downarrow\rangle$ transition) are visible in Fig. 5.2(h). In bidirectional δ' -scans, the distortion appears as a sharp drop in the fluorescence intensity (but not to zero) followed by a Lorentzian-like lineshape. The distortion distance (defined as the distance from the sharp drop to the point where the signal rises to the same intensity again) is ~ 0.6 GHz.

5.4 Nuclear-Spin Assisted Coherent Population Trapping

The bistability in the recovery plateau calls for explanations of the dynamic nuclear spin polarisation with limited noncollinear interaction in the GaAs QD Λ -system. The exact

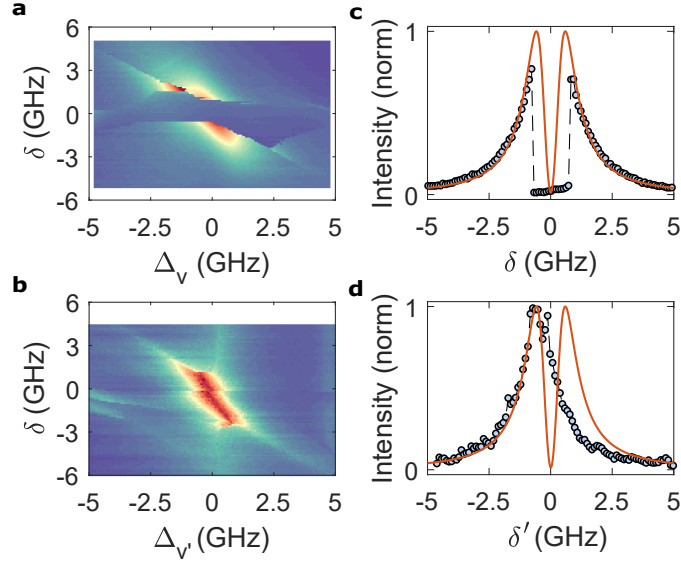


Fig. 5.3. **Overhauser-field selected coherent population trapping.** (a) Recovery plateau of the X^{1-} when both lasers are close to the resonance condition on the blue-Zeeman branch. Two excitation lasers have the same power, which corresponds to a Rabi frequency of $\Omega = 1.7 \Gamma$. The gate voltage is scanned in the forward direction. But between each V_g step, the QD is quickly tuned into the co-tunnelling region for electron-spin randomisation. The resulting recovery plateau reveals a “butterfly”-shaped dark region which does not depend on V_g -scan direction. (b) Recovery plateau of the red-Zeeman branch with electron-spin randomisation. Similarly to the blue-Zeeman plateau, the bistability is erased. However, the recovery plateau has a distortion in the centre rather than any dark region. (c) Spectrum of the blue-branch recovery plateau resolved in δ when $\Delta_v = 0$ (circles and dashed line). The orange line represents the standard CPT spectrum of a simple Λ -system. In this simple Λ -system, we only consider the optical drivings, the relaxation and dephasing of the excited state, and that of the ground states. The interaction between electron- and nuclear-spins is omitted. Such a standard model can match well with the rising and falling edge of the measured spectrum of the recovery plateau. In the experiment, for $\delta \rightarrow 0$ the nuclear-spin effects play an important role. The dark state exists over a broader detuning range compared to the standard CPT spectrum. (d) Spectrum of the red-branch recovery plateau resolved in δ' when $\Delta_{v'} = 0$ (circles and dashed line). At small δ , the nuclear spins shift the QD resonance such that the CPT resonance condition is avoided.

answer remains under investigation. To gain more insight, we perform the two-colour experiment with a randomised electron-spin. Instead of sweeping V_g unidirectionally, a quick jump to the co-tunnelling gate voltage (e.g. $V_g = -0.54V$) is added between every V_g step. This jump takes several milliseconds, which thus restores the thermal occupation of the electron spin-state to the equilibrium. The resulting recovery plateau is visible in Fig. 5.3(a) for the blue-Zeeman branch, and Fig. 5.3(b) for the red-Zeeman branch. On both Zeeman branches, the spectrum in the recovery plateau when sweeping V_g in forward or backward directions together with electron-spin randomisation looks the

same. (Only one spectrum per Zeeman branch is shown.) The slow hysteresis induced by the nuclear spin polarisation is erased; the bistability depending on the scan direction is not observed.

However, the stark contrast in the recovery plateau between different Zeeman branches remains. On the blue-Zeeman branch, the QD is locked to the CPT resonance condition and the associated dark-region is extended to a “butterfly” shape. On the red-Zeeman branch, the CPT resonance is avoided and the recovery plateau is always bright: the dark region is not visible, instead, a distortion in the centre of the recovery plateau can be found. In Fig. 5.3(c), a line-cut at $\Delta_v = 0$ (circles and dashed line) is taken from (a) on the blue-Zeeman recovery plateau and compared with the standard CPT spectrum (orange line). For calculating the standard CPT spectrum, the electron-nuclear spin coupling is not taken into consideration. We assume a branching ratio of $\Gamma_{v(\prime)} = 4 \Gamma_{d(\prime)}$. The two lasers have the same amplitude, which translates into a Rabi frequency of $\Omega = 1.7 \Gamma$. The electron spin has a T_1 time³⁷ of $\sim 50 \mu s$, corresponding to a spin-flip rate $\kappa_{\uparrow\downarrow} = 20$ kHz. The upper-state dephasing (due to phonons and spectral fluctuations) is estimated to be $\gamma_{\uparrow} \sim 2\pi \times 25$ MHz from linewidth broadening. Electron spin dephasing in the ground state is set to $\gamma \sim 2\pi \times 10$ MHz to match the depth of the measured CPT dark region in the recovery plateau. The height of the recovery plateau signal is scaled such that its rising edge matches the standard CPT spectrum. In comparison to the standard CPT, the coupled electron-nuclear spin system in the blue-Zeeman branch tends to jump into the CPT dark state more abruptly and maintain this dark state for a range (1.6 GHz in Fig. 5.3(c)) much larger than the standard CPT (full width at half maximum of 0.5 GHz). On the red Zeeman branch, the line-cut at $\Delta'_v = 0$ overlaps with the standard CPT theory in Fig. 5.3(d). For visibility reasons, we shift the measured spectrum in δ' to match the theory rising edge. The falling edge of the measured spectrum is parallel to the theory as well. Here, the electron-nuclear spin interaction shifts the QD resonance to avoid the CPT dark-state condition. The shift by nuclear-spin effects can be estimated by the distance between the falling edge of the measured and standard CPT spectrum. In Fig. 5.3(d), this shift is 0.85 GHz.

5.5 Summary

In this chapter, we optically excite the low-noise GaAs QDs when a magnetic field is applied in a Faraday configuration. Sweeping a single-laser across the QD resonance results in a lineshape close to the typical Lorentzian profile – nuclear-spin polarisation is not obvious, which is a hint for a strongly suppressed quadropolar field. In a two-colour

experiment, we discover dynamic nuclear-spin polarisation in the recovery plateau. Although the detailed theoretical investigation is still under development, we speculate that such nuclear-spin polarisation originates from the hole spin of the excited trion states. Changing the experimental scheme slightly, we find that bistability can be erased by electron-spin randomisation, but the nuclear-spin effects remain very different on the blue- and red-Zeeman branches. The understanding of such electron-nuclear spin coupling could help for nuclear-spin cooling¹⁴³ and extending the electron-spin coherence²³ in GaAs QDs.

5.6 Methods

The experiments in this chapter is performed with a standard dark-field technique⁷⁵ on the low-noise GaAs QDs. Both one-colour and two-colour experiments employ narrow-band continuous-wave lasers. In the two-colour experiment, the frequency of one laser is fixed, f_{fixed} . The frequency of the other laser, f_{scan} , is increased step-by step (step size ~ 1 GHz). The recovery plateaus of the negative trion are mapped out by scanning the external gate voltage V_g for every f_{scan} . When f_{fixed} is close to the centre of the blue-Zeeman branch, the resulting four recovery plateaus are shown in Fig. 5.4(a). Depending on f_{scan} and the V_g -scan direction, different spectra of the recovery plateaus are observed. Part of these spectra are shown in Fig. 5.2(c,d). The entire spectrum is visible in Fig. 5.4(b-e) for the four recovery plateaus. When f_{fixed} is close to the centre of the red-Zeeman branch, the resulting recovery plateaus are shown in Fig. 5.2 (f,g) and Fig. 5.5.

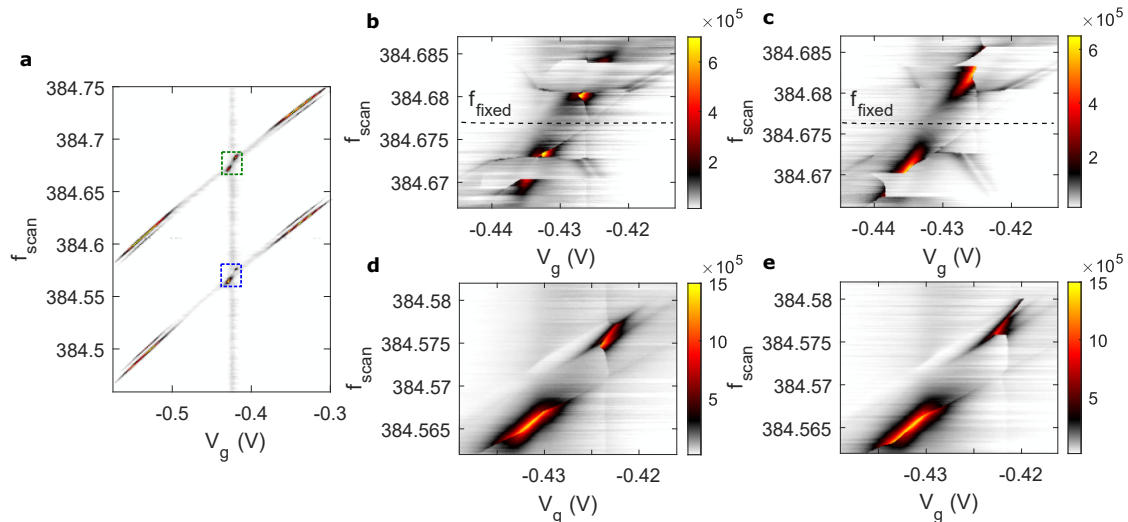


Fig. 5.4. Recovery plateau on the blue Zeeman branch. (a) Trion resonance under two-colour excitation. The fixed-laser is positioned on the blue-Zeeman branch, $f_{\text{fixed}} = 384.677$ THz [same for the subplots (b-e)]. Both the scan and the fixed-laser are weak in intensity, $\Omega = 0.7 \Gamma$. Four recovery plateaus are visible in the spin-pumping region. Two of them can be found on the blue-Zeeman branches, whose intensity is similar. The other two are on the red-Zeeman branches, where there an asymmetry in intensity can be observed. The green box represents the recovery plateaus in (b,c), while the blue box marks the location of the recovery plateaus in (d,e). (b,c) The recovery plateaus on the blue-Zeeman transitions in different V_g -scan directions. Here, both the fixed-laser and scan-laser address the blue-Zeeman branch. For every f_{scan} , we sweep the gate voltage V_g in either the forward or the backward directions. The two resulting recovery plateaus are shown in (b) and (c), respectively. For both, the upper recovery plateau appears when f_{scan} is on resonance with the vertical transition $|\uparrow\rangle - |\uparrow\downarrow\rangle$, while f_{fixed} matches the diagonal transition $|\uparrow\rangle - |\uparrow\downarrow\rangle$. In the lower recovery plateau, f_{scan} and f_{fixed} are flipped: the fixed-laser is on resonance with the vertical transition and the scan with the diagonal one. Since the scan- and the fixed-laser have the same power (for b-e, $\Omega = 1.7 \Gamma$), the upper and lower recovery plateau can in principle be transformed from one to the other. We have plotted the lower recovery plateaus as a function of detuning in Fig. 5.2(c,d). (d,e) The recovery plateaus on the red-Zeeman transitions in different V_g -scan directions. The scan-laser f_{scan} addresses the transitions on the red-Zeeman branch. When the fixed-laser addresses the vertical transition of the blue-Zeeman and the scan-laser addresses the vertical one of the red, the bright recovery plateaus appear in (d,e) at around -0.43 V. Alternatively, when the two lasers each addresses one diagonal transition, the corresponding recovery plateaus are weaker at -0.42 V. Slight differences can be seen when comparing the spectra of different V_g -scan directions.

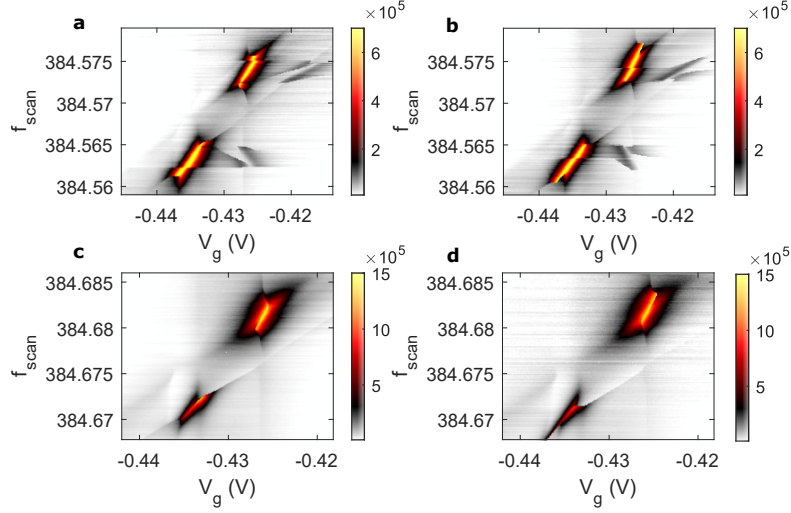


Fig. 5.5. **Recovery plateau on the red Zeeman branch.** (a,b) The recovery plateaus on the red-Zeeman transitions in different V_g -scan directions. Here, both the fixed-laser and scan-laser address the red-Zeeman branch. The fixed-laser is positioned at $f_{\text{fixed}} = 384.576$ THz [same for the subplots (c,d)] For every f_{scan} , we sweep the gate voltage V_g in either the forward (a) or the backward (b) directions. A distortion appears in the centre of each recovery plateau. The position of this distortion depends on the V_g -scan direction. We have plotted the upper recovery plateaus as a function of detuning in Fig. 5.2(f,g). (c,d) The recovery plateaus on the blue-Zeeman transitions. Similarly, the experimental conditions of the two plots are different in terms of the V_g -sweep direction. The fixed-laser is still on the red-Zeeman branch, but the scan-laser sweeps across the blue-Zeeman branch. Similar to Fig. 5.4, there exist a bright and a weak recovery plateau in either (c) or (d). Comparing the recovery plateaus in (c) and in (d), one can also find a small dependence on the V_g -direction.

Chapter 6

Quantum Interference of Identical Photons from Remote Quantum Dots

This chapter is adapted from the following article:

Liang Zhai, Giang Nam Nguyen, Clemens Spinnler, Julian Ritzmann, Andreas D. Wieck, Matthias. C. Löbl, Arne Ludwig, Alisa Javadi, and Richard J. Warburton, *Quantum Interference of Identical Photons from Remote Quantum Dots*, arXiv: 2106.03871 (2021).

The article has been later published as **Nature Nanotechnology** 17, 829–833 (2022).

Photonic quantum technology provides a viable route to quantum communication^{22,83}, quantum simulation¹⁹, and quantum information processing¹⁴⁶. Recent progress has seen the realisation of boson sampling using 20 single-photons¹⁹ and quantum key distribution over hundreds of kilometres²². Scaling the complexity requires architectures containing multiple photon-sources, photon-counters, and a large number of indistinguishable single photons. Semiconductor quantum dots are bright and fast sources of coherent single-photons^{7,9,11,147,148}. For applications, a significant roadblock is the poor quantum coherence upon interfering single photons created by independent quantum dots^{149,150}. Here, we demonstrate two-photon interference with near-unity visibility ($93.0 \pm 0.8\%$) using photons from two completely separate GaAs quantum dots. The experiment retains all the emission into the zero-phonon-line – only the weak phonon-sideband is rejected – and temporal post-selection is not employed. Exploiting the quantum interference, we demonstrate a photonic controlled-not circuit and an entanglement with fidelity ($85.0 \pm 1.0\%$) between photons of different origins. The two-photon interference visibility is high enough that the entanglement fidelity is well above the classical threshold. The high mutual-coherence of the photons stems from high-quality material, a diode-structure, and the relatively large quantum dot size. Our results establish a platform, GaAs QDs, for creating coherent single photons in a scalable way.

6.1 Background

From large-scale quantum simulations¹⁹ to multi-user quantum networks⁸³, the requested number of photons soars as the complexity grows. Single-photon sources meeting these needs do not yet exist. While current proof-of-principle demonstrations of photonic quantum applications rely mostly on parametric down-conversion sources^{146,151}, the adoption of deterministic sources is a clear trend^{7,9,11,18,147,148,152}: semiconductor quantum dots (QDs) are on-demand emitters with a significantly higher efficiency and photon generation-rate than down-conversion sources^{7,11}. In addition, QDs can be easily integrated into various nanostructures^{9,64,148}. For single-photon generation, these advantages make QD-based sources arguably the best choice^{7,11}. However, to create a large number of photons, the prevalent approach – active demultiplexing from a single QD¹⁹ – is not optimal. It introduces additional losses and leads to a large resource overhead, limiting the maximal number of photons.

A more advantageous approach is to create indistinguishable photons simultaneously from multiple QDs single-photon sources. This facilitates scaling up to higher photon numbers without sacrificing efficiency and photon generation-rate. It is an enabling technology with immediate use in photon-based boson sampling¹⁹, device-independent quantum key distribution¹⁵³ (QKD) and a photonic approach to measurement-based quantum computing¹⁴⁸ (MBQC). All these concepts call for quantum interference (i.e. interference with unity visibility) between photons from separate sources with no additional filtering loss. However, achieving such quantum interference using separate QDs has been a challenge for many years^{53,149,150,154–157}. The reason is that the quantum interference is sensitive to the total noise in two uncorrelated solid-state environments. Fast noise processes (upper-level dephasing) and slow noise processes (spectral fluctuations) over an enormous bandwidth all contribute. So far, the highest visibility on interfering photons directly created by two separate QDs (without filtering) is just above 50%¹⁴⁹.

In this chapter, we show a two-photon interference visibility of $\mathcal{V} = 93\%$ when interfering the photons created by two separate QDs in distant cryostats. The key is the employment of gated GaAs QDs. This system exhibits an ultra-low level of noise – exciton dephasing is small compared to the radiative rate; spectral fluctuations are weak compared to the spectral linewidth – as confirmed by the high visibility of single-QD and two-QD Hong-Ou-Mandel (HOM) interference. We exploit the quantum interference to introduce entangling capabilities to the remote solid-state systems [Figure 6.1(a)]. We demonstrate a controlled-not (CNOT) gate, the fundamental two-qubit logic in quan-

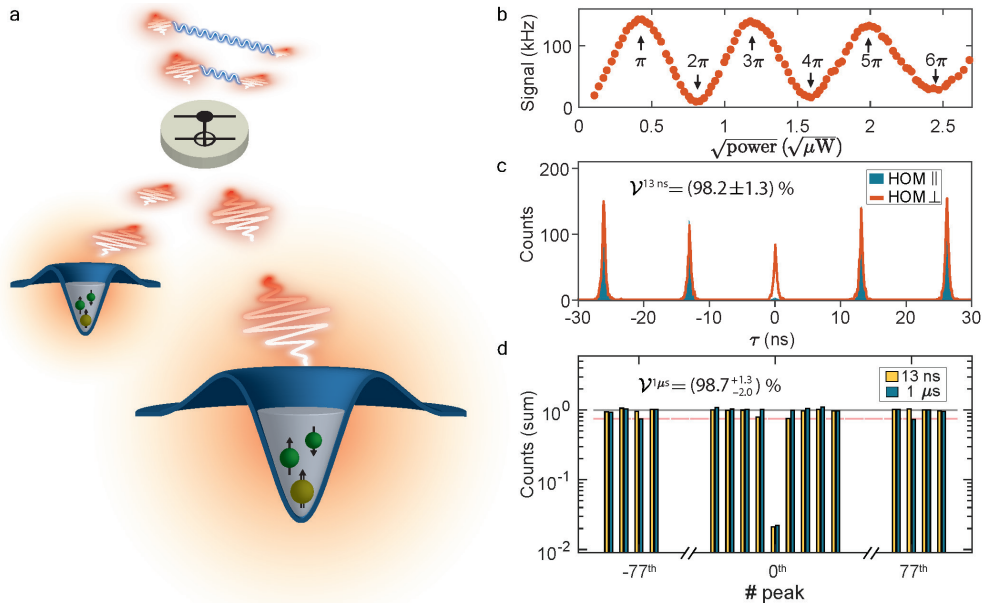


Fig. 6.1. **Coherent single photons from GaAs quantum dots at a wavelength of 780 nm.** (a) Schematic of an entangling gate between photons from two separate GaAs QDs. Each QD is independently excited (creating two electrons and one hole, the X^-) and generates a stream of single photons. When the two photon-streams are identical, quantum interference takes place in the gate, entangling the two photon streams. (b) Resonance fluorescence from an individual QD (QD2, X^-) reveals Rabi oscillations. A π -pulse power is chosen for all subsequent experiments. (c) Hong-Ou-Mandel (HOM) experiments on QD2 X^- showing quantum interference of photons created 13 ns apart. (d) Two-photon interference for two different delays, 13 ns and 1 μs . Each bar represents the total coincidence counts summing over one whole pulse period and is normalised at long delays. The coincidence probability is nearly identical for the two delays, while the side peaks are flat and close to one (grey line). The red line indicates the decrease to 75% due to route probability.

tum algorithms, between two independently generated streams of photons. Utilising the CNOT operation, an entangled two-photon state is created: in the entangled pair, one photon is created by one semiconductor chip, the other photon is created by a separate chip far apart. Our results suggest that the GaAs QD platform represents a versatile launchpad for scalable photonic technologies.

6.2 Indistinguishable Photons from Single GaAs Quantum Dots

The QDs are hosted in n - i - p -diode heterostructures³⁷. Three typical dots, namely QD1 – QD3, are presented in Appendix Fig. A.1 and A.2. For on-demand single-photon generation, we excite the QDs resonantly with short laser pulses (duration 6 ps). A 22 GHz-bandwidth spectral filter is inserted in the collection to improve laser suppress-

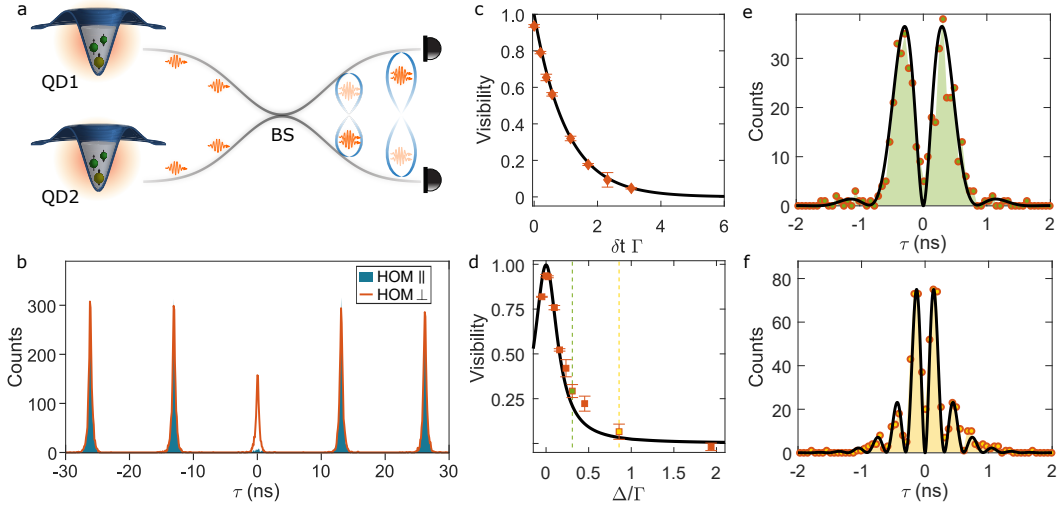


Fig. 6.2. **Two-photon interference from remote quantum dots.** (a) Schematic of quantum interference between photons from two remote GaAs QDs. Provided the photons are indistinguishable, they coalesce and exit the beamsplitter (BS) at the same port. (b) HOM interference from photons generated by two remote QDs. The vanishing central peak shows a raw HOM visibility of $(90.9 \pm 0.8)\%$ and a true two-photon interference visibility of $(93.0 \pm 0.8)\%$. (c,d) Two-QD HOM visibility as a function of normalised temporal delay δt and spectral detuning Δ between the two QDs. In (c), the QD2 photons are delayed with respect to QD1 by a delay δt . In (d), the frequency detuning Δ between the two QDs is varied by exploiting the exquisite frequency control provided by the electrical gates. (e,f) Pronounced quantum beats are revealed in the two-QD HOM central peak when the QDs are slightly detuned in frequency. The green and yellow colours indicate the detuning in (d). The solid-lines in (c-f) show the quantum-optical theory. In the theory, we assume the wave-packets of remote QDs are identical except for a small delay in (c) and a small detuning in (d-f).

sion, and to remove the weak phonon sideband and radiative Auger emission³⁸. Figure 6.1(b) shows Rabi oscillations up to 6π . The first Rabi cycle shows the highest contrast – at a Rabi power of 2π the signal intensity drops to just $\sim 6\%$ of that at π power.

In the following experiments of this chapter, a π -pulse power is used to ensure that the excited state population is maximised to near-unity before photon creation. The purity of the photons, as characterised by $1 - g^{(2)}(0)$ in a Hanbury Brown-Twiss measurement, is $(99.0 \pm 0.1)\%$. To probe the indistinguishability of single-QD photons, we perform a HOM experiment: the single photons are sent into a Mach-Zehnder interferometer (see Appendix Fig. A.5), where a photon travelling through the longer path overlaps on a symmetric beamsplitter with the \mathcal{N}^{th} subsequently emitted photon travelling through the shorter path. Figure 6.1(c) shows the HOM measurements on QD2 X^- for $\mathcal{N} = 1$, that is, the delay of the interferometer corresponds to one repetition pulse-period ($\mathcal{D} =$

13 ns). By preparing the two photons in the same polarisation (co-polarisation) the central HOM peak vanishes due to quantum interference. On the contrary, the photons become distinguishable in cross-polarisation: the quantum interference no longer takes place and the central peak appears. The raw HOM visibility, defined as the ratio of the central-peak intensity between co-polarised (HOM \parallel) and cross-polarised (HOM \perp) configurations, is $\mathcal{V}_{\text{raw}}^{13\text{ns}} = (95.8 \pm 1.2)\%$. The true HOM visibility for QD2 is $\mathcal{V}^{13\text{ns}} = (98.2 \pm 1.3)\%$ on correcting¹⁵⁸ the raw visibility for the finite $g^{(2)}(0)$ and experimental imperfections (see Methods). Here, we calculate \mathcal{V} by summing over the whole pulse period [the yellow bars in Fig. 6.1(d)]. This evaluation time-window ($T_{\text{bin}} = 13$ ns) is significantly larger than the QD lifetime ($1/\Gamma_2 = 256$ ps) and thus introduces no temporal post-selection. (Narrowing the time bin T_{bin} artificially increases the HOM visibility at the expense of efficiency.) For QD1, we achieve comparable results: $1 - g^{(2)}(0) = (98.7 \pm 0.2)\%$, and $\mathcal{V}^{13\text{ns}} = (97.8 \pm 1.8)\%$.

The ambient environment of a QD can be static on a short time-scale such that it has little impact on the coherence between consecutively emitted photons ($\mathcal{N} = 1$). However, slowly varying noise, for instance spectral fluctuations, decrease the HOM visibility on longer time-scales^{67,68}. By adding a 200-metre fibre to the HOM interferometer, we extend the delay to $\mathcal{D} \sim 1$ μs , overlapping the two photons separated by 77 pulse periods ($\mathcal{N} = 77$). The HOM interference of 13 ns and 1 μs separation are compared in Fig. 6.1(d). We extract the 1 μs HOM visibility for QD2 ($T_{\text{bin}} = 13$ ns), $\mathcal{V}_{\text{raw}}^{1\mu\text{s}} = (95.7 \pm 2.0)\%$ and $\mathcal{V}^{1\mu\text{s}} = (98.7_{-2.0}^{+1.3})\%$. (Similarly good results are achieved on QD1, $\mathcal{V}^{1\mu\text{s}} = (99.0_{-1.8}^{+1.0})\%$, see Appendix Sec. A.2.) As for the 13 ns case, the 1 μs HOM visibility remains near-unity. As far as the HOM is concerned, we deduce that the QD environment is static over a time-scale at least 4×10^3 larger than the QD's lifetime.

6.3 Two-Photon Interference from Distant Emitters

We now turn to the quantum interference between photons from independent sources [Fig. 6.2(a)]. For QD-based sources, the challenge lies not only in matching emitters both spectrally and temporally but also in suppressing noise over a huge bandwidth. Exploiting the large Stark tuning, QD1 and QD2 are well-matched: their temporal overlap is $\Gamma_1/\Gamma_2 = 96\%$, while the spectral overlap is $\Delta\nu_1/\Delta\nu_2 = 95\%$ (with $\Delta\nu_{1,2}$ denoting the measured linewidths). QD1 and QD2 are located in two individual wafer pieces and are hosted in two cryostats separated by 20 metres (in fibre length). Thus, the environments of QD1 and QD2 are completely uncorrelated. As such, the remote-interference visibility is sensitive to the noise in both semiconductor environments over

a huge bandwidth, from 10^{-4} Hz to 10^9 Hz. Despite this sensitivity to environmental noise, the visibility is near-unity, $\mathcal{V}^{\text{remote}} = (93.0 \pm 0.8)\%$ [Fig. 6.2(b)]. The high visibility is not limited to only one pair of QDs: between QD1 and QD3 (another QD in the QD2-cryostat), a similar two-QD HOM visibility is observed, $\mathcal{V}^{\text{remote}} = (92.7 \pm 1.6)\%$.

The crucial aspects to achieve the high two-QD HOM visibility are an *n-i-p* diode heterostructure³⁷ and well-controlled growth: the diode locks the QD charge-state via Coulomb blockade and suppresses spectral fluctuations; in the growth, impurities are minimised yielding ultra-pure materials. The GaAs QDs themselves are also important. GaAs QDs are larger in size (~ 100 nm in diameter and 5-7 nm in height) with respect to InGaAs QDs. The larger QD-size increases the radiative rate thereby increasing the lifetime-limited linewidth, rendering the QD less sensitive to environmental fluctuations. Furthermore, the larger QD-size reduces slightly both the spin-noise, the main source of inhomogeneous broadening in low-charge-noise InGaAs QDs⁹⁸, and the exciton-phonon scattering rate, the main source of homogeneous broadening.

On account of the uncorrelated environments, the two-QD HOM interference is equivalent to the coalescence of two photons from a single QD with an almost-infinite separation in time ($\mathcal{N} \rightarrow \infty$). Such coalescence is otherwise difficult to measure. For highly developed InGaAs QDs, 96% one-QD photon indistinguishability has been achieved¹¹ for temporal separation of up to 10^{-6} s. Our two-QD HOM interference indicates that 93% one-QD indistinguishability can be achieved using gated GaAs QDs with a longer temporal separation – as long as 10^4 s. As the residual noise in the QDs lies mostly at low-frequency ($< 10^4$ Hz), we expect to maintain a 98% one-QD indistinguishability even for a separation of 10^{-4} s. Assuming 100 MHz excitation repetition, such a separation infers that trillions more photons can be coherently created from a single-QD.

Our two-QD HOM experiments are carried out under rigorous conditions: there is no Purcell enhancement of the radiative rate, no temporal post-selection, no narrow spectral filtering, and no active frequency stabilisation. Adding temporal post-selections or narrow spectral filters leads to higher two-QD HOM visibility, but the flux of usable photons goes down as the visibility goes up (Figs. 6.4 and Fig. A.13). For practical applications, it is clearly better to avoid this loss. In this way, connecting multiple QD sources does not introduce an additional loss to the source efficiency.

The small imperfections in one-QD and two-QD HOM visibilities allow an estimation of the remaining noise. The fast noise process is exciton dephasing at rate Γ^* . This process is likely to arise from phonon scattering^{44,68}, resulting in a contribution to the homogeneous spectral-linewidth of $\Delta\nu_H = \Gamma^*/\pi$. Random changes in local environments of each QD are responsible for the slow noise process⁹⁸ – a spectral fluctuation. Assuming

identical QDs and a Lorentzian probability distribution⁹⁸ for each QD (with frequency width $\Delta\nu_{\text{H}}$) to describe the spectral fluctuations, the two-QD HOM visibility \mathcal{V} is given by:

$$\mathcal{V} = \frac{1}{1 + 2\pi(\Delta\nu_{\text{H}} + \Delta\nu_{\text{S}}) \cdot \tau_{\text{r}}}, \quad (6.1)$$

where τ_{r} is the radiative lifetime. This result demonstrates that a high \mathcal{V} is achieved only when both exciton dephasing and spectral fluctuations are suppressed. In the one-QD HOM experiment, the environment is static ($\Delta\nu_{\text{S}} \rightarrow 0$) and the imperfection in \mathcal{V} determines the homogeneous broadening. We find $\Gamma^* = 34 \pm 25$ MHz, equivalently $\Delta\nu_{\text{H}} = 11 \pm 8$ MHz. In the two-QD HOM experiment, \mathcal{V} depends on both exciton dephasing and spectral fluctuations allowing $\Delta\nu_{\text{S}} = 34 \pm 15$ MHz to be determined. The average single-QD linewidth predicted from this HOM-analysis, $1/(2\pi\tau_{\text{r}}) + \Delta\nu_{\text{H}} + \Delta\nu_{\text{S}}$, matches well with the measured linewidth. This analysis shows that together, the one-QD and two-QD HOM experiments enable the fast and slow noise processes to be separately determined (see Appendix Sec. A.3 for details).

The interference visibility of photons from independent GaAs QDs ($\mathcal{V}^{\text{remote}}$) is an important metric for the application of this system in quantum technologies. The visibility is comparable to that achieved in trapped ions^{159,160} and cold atoms¹⁶¹, the seemingly most identical emitters. It is also comparable to the visibilities achieved with state-of-the-art parametric photon sources¹⁵¹ and with coherent scattering from solid-state emitters²⁷. However, both parametric sources and coherent scattering operate in an intrinsically probabilistic manner where the photon generation rate is compromised to achieve high interference visibility. The two-QD HOM visibility is slightly higher than that achieved with remote nitrogen-vacancy centres^{162,163} for which temporal post-selections and narrow spectral filters are required: both considerably decrease the impact of spectral fluctuations at the expense of a reduced efficiency.

To map out the dependence of the two-QD HOM visibility on the two-photon coalescence, we deliberately reduce the overlap either temporally or spectrally. As the delay between the two QDs' photons δt increases, the interference visibility decreases exponentially [Fig. 6.2(c)], a consequence of the reduced temporal overlap of the two wave-packets. This is in excellent agreement with theoretical calculations for exponentially-decaying wave-packets¹⁶⁴ (Appendix Sec. A.3.1). When reducing the spectral overlap, the two-QD HOM visibility follows a Lorentzian profile on detuning Δ [Fig. 6.2(d)], again exactly as expected from theory. This configuration offers a further test of the photon coherence. When the two photons are slightly detuned in frequency, a quantum beat is expected in the time-dependence of the intensity correlation function¹⁶⁴. These

quantum beats are very clearly observed: Figure 6.2(e,f) show quantum beats in the central HOM peak for $\Delta/\Gamma = 0.31$ and $\Delta/\Gamma = 0.87$, respectively. The oscillation period decreases as Δ increases. These pronounced quantum beats match nicely with theoretical calculations, and from a different perspective, reflect the mutual coherence of the photons created by the remote QDs.

6.4 A Quantum Logical Gate Linking Remote Single-Photon Sources

Indistinguishable photons from distant QDs enable the creation of a CNOT gate. Quantum information can be encoded into the two separate streams of photons, and the CNOT unit allows the creation of entanglement between photons of different origins. The optical CNOT circuit can be realised by a combination of two half-wave plates (HWP) at 22.5° and three partially polarising beamsplitters¹⁸ (PPBS), as depicted in Fig. 6.3(a). Single photons from the remote QDs are encoded as polarisation qubits: $|H\rangle = |0\rangle$, $|V\rangle = |1\rangle$. Each 22.5° HWP acts as a Hadamard gate; the three PPBSs constitute a controlled-phase gate¹⁶⁵. The controlled-phase gate relies on coincidence clicks on detectors in two opposite output arms. The central PPBS transmits H -polarised qubits $T_H = 1$, and partially reflects (transmits) V -polarised qubits $R_V = 2/3$ ($T_V = 1/3$). Upon simultaneous arrival at the PPBS, quantum interference between two indistinguishable photons provides a π -phase shift in the $|VV\rangle$ amplitude¹⁶⁵. The other two PPBSs are rotated by 90° , such that $T_V = 1$ and $T_H = 1/3$, in order to compensate the imbalance between H - and V -polarised components in the output. The gate operation is probabilistic (success probability = $1/9$).

We evaluate the gate performance using the input-output relations in both the computational basis $|H\rangle/|V\rangle$ and the basis defined by the linear superpositions $|\pm\rangle = 1/\sqrt{2}(|H\rangle \pm |V\rangle)$. Ideally, in the $|H\rangle/|V\rangle$ basis (ZZ basis in Pauli matrix language) the target qubit flips the sign when the control reads logical one. In the $|+\rangle/|-\rangle$ basis (XX basis), the target qubit decides whether its control counterpart undergoes a flip. Experimentally, the output-states are analysed by a quantum tomography setup. The corresponding truth tables are shown in Fig. 6.3(b,c). The CNOT operation fidelity in ZZ and XX bases are $\mathcal{F}_{ZZ} = (88.90 \pm 5.34)\%$, and $\mathcal{F}_{XX} = (89.34 \pm 5.29)\%$. We calculate the bound for the overall quantum process fidelity¹⁸ based on $(\mathcal{F}_{ZZ} + \mathcal{F}_{XX} - 1) < \mathcal{F}_{\text{proc}} < \min(\mathcal{F}_{ZZ}, \mathcal{F}_{XX})$, yielding $(78.24 \pm 7.53)\% < \mathcal{F}_{\text{proc}} < (88.90 \pm 5.34)\%$.

Finally, we demonstrate the ability to create maximally entangled states using the photonic qubits from remote QDs. This is the hallmark of the CNOT operation – by

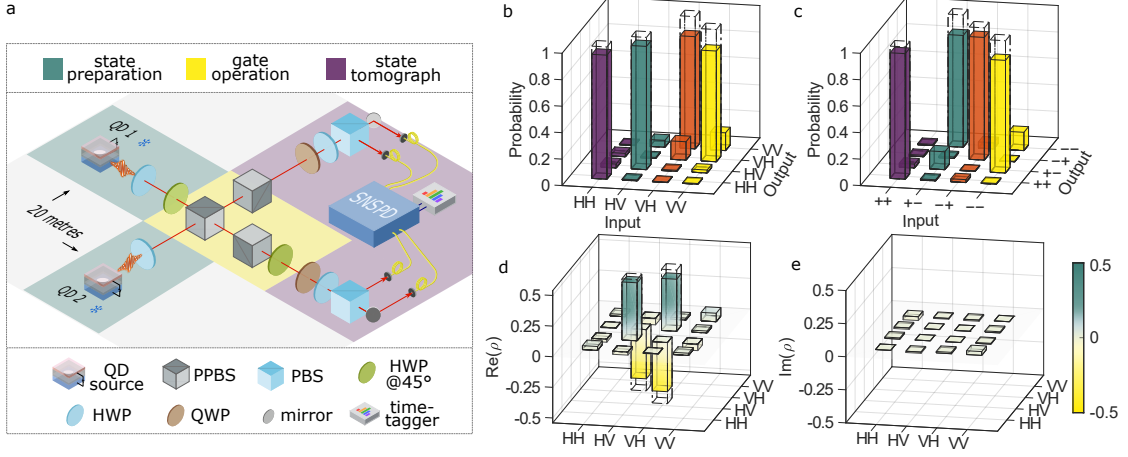


Fig. 6.3. **A quantum logic gate connecting photons from remote quantum dots.** (a) Sketch of the experimental setup for the CNOT gate based on two-photon interference between remote QDs. The photons from QD2 are used for the control qubit, and the photons from QD1 for the target qubit. For state preparation (highlighted in green), photons from the two QDs are carefully balanced to the same flux where their polarisations prepare the input states. The CNOT gate is highlighted in yellow. Half-wave plates (HWP) at 22.5° are Hadamard gates bringing H - and V -polarisations to the superposition. The central partially polarising beamsplitter (PPBS) transmits H -polarised light $T_H = 1$, while partially reflects (transmits) V -polarised light $R_V = 2/3$ ($T_V = 1/3$). Upon simultaneous arrival at this PPBS, quantum interference between two indistinguishable photons provides a π -phase shift in the $|VV\rangle$ amplitude¹⁶⁵. The two PPBSs in opposite arms are each rotated by 90° with respect to the central one, such that their $T_H = 1/3$, reducing the amplitude of H -polarised components to the same of $|VV\rangle$. Together, the three PPBSs constitute a controlled- Z gate. After the gate operation, the quantum state is projected in a quantum tomography setup (highlighted in purple). For every input state, the output state is mapped out using four simultaneous coincidence-measurements. (b,c) The truth tables for $|H\rangle/|V\rangle$ and $|+\rangle/|-\rangle$ bases. The coincidence events are converted to probabilities by normalising to the respective input state. For each input state, we accumulate total coincidence counts of ~ 500 . As in the HOM analysis, we do not use any temporal post-selection, $T_{\text{bin}} = 13$ ns. The empty dashed bars represent the ideal CNOT operation. (d,e) The real (d) and imaginary (e) parts of the density operator of state $|\Psi^-\rangle$ created by the CNOT gate. The real parts of the measured density matrix, $\text{Re}(\rho)$, are close to ideal (represented by the empty bars). In the imaginary parts, $\text{Im}(\rho)$, the intensities are all below 0.03.

preparing the input state as $|-\rangle_c |V\rangle_t$, the Bell state $|\Psi^-\rangle = \frac{1}{\sqrt{2}}(|HV\rangle - |VH\rangle)$ is produced. To fully characterise the produced state, quantum state tomography is performed with a series of 36 coincidence measurements, followed by state reconstruction using a maximum-likelihood-estimation algorithm¹⁶⁶. The real and imaginary parts of the reconstructed density matrix ρ are shown in Fig. 6.3(d, e). We obtain an entanglement fidelity of $\mathcal{F}_{\Psi^-} = (85.02 \pm 0.97)\%$, which exceeds the threshold of $(2 + 3/\sqrt{2})/8 = 0.78$ for violating Bell inequalities¹⁶⁵. To quantify the entanglement, we calculate the con-

currence $C = (74.67 \pm 1.93)\%$ and the linear entropy $S_L = (34.04 \pm 1.94)\%$. These values indicate a high level of entanglement established using two separate streams of photons.

Based on the measured two-QD HOM visibility, $\mathcal{V}^{\text{remote}} = 93.0\%$, the expected entanglement fidelity is 90.2%; the expected process fidelity in the computational basis is 93.9%. The slight mismatch with respect to the experiment is likely due to imperfections in the optical elements and the non-zero $g^{(2)}(0)$ values. The CNOT demonstration highlights the importance of high-visibility two-QD HOM-interference: if the visibility is low, the entanglement fidelity will be worse; a minimal visibility of $\mathcal{V} = 83\%$ is required in our scheme for the generated entanglement fidelity to surpass the Bell-inequality violation threshold, $\mathcal{F}_{\Psi^-} > 78\%$.

6.5 Summary

In this chapter, we have demonstrated that GaAs QDs are interconnectable sources of indistinguishable single photons. The near-unity mutual-coherence between photons created by separate QDs points to the potential of employing multiple QD-sources in quantum applications. The extraction efficiency can be boosted by the Purcell effect upon coupling the QDs to a single optical mode^{7,11,148}. The HOM visibility should also benefit from the reduced lifetime (Purcell effect, Eq. 6.1): with the present noise level, a Purcell factor $F_p \sim 10$ should result in one-QD and two-QD HOM visibilities of 99.6% and 99.0%, respectively. From a quantum-information perspective, increasing the number of identical photons to ~ 50 will lead to quantum advantage in a boson sampling experiment¹⁴⁸. This number of photons is within reach, for instance, using several gated GaAs QDs together with current photonic technologies¹⁹. For measurement-based quantum computing, once few-photon cluster states are generated by individual QDs^{167,168}, projective entangling gates allow the small clusters to be “fused” into large-scale computational resources¹⁴⁸. High remote-interference visibility points to a high-fidelity entangling operation. From a quantum communication perspective, highly indistinguishable photons forge a coherent link between remote QDs, a route to the realisation of device-independent QKD with high key rates¹⁵³. Moreover, GaAs QDs can be brought into exact resonance with rubidium transitions, allowing the storage of QD photons in a rubidium-based quantum memory⁵².

6.6 Methods

We describe the efforts involved in finding two QDs with near-perfect frequency and decay-rate overlap. To assess this, we deliberately fix QD1 as one of the candidates in one cryostat (cryo1) and look for another candidate in the second cryostat (cryo2). Two parameters are critical for the search – the X^- emission frequency and its radiative lifetime. Employing spatially resolved photoluminescence mapping¹⁷ (PL-map), we establish the connection between QD emission frequency and QD spatial location in a $25 \times 25 \mu\text{m}^2$ region. A PL-map takes usually 5 – 6 hours to record and contains ~ 200 QDs, with all QD positions and emission frequency logged in a coordinate system. Among the QDs in one PL-map, we typically find 3 – 6 QDs whose X^- frequency is close to QD1. The position information allows us to move to these selected QDs one by one and investigate their linewidths, lifetimes and frequency tuning ranges, similar to the measurements in Appendix Sec. A.1. The lifetimes of QDs in our sample are similar: based on the lifetime measurements of ten randomly chosen QDs, the coefficient of variation is only $C_v(\tau) = 0.2$. Thanks to this small spread in lifetime and the near-lifetime-limited optical linewidths, screening a QD suitable in both lifetime and frequency is not demanding (e.g. it took two PL-maps to find QD2). This screening process can be further simplified in future if lifetime tuning is in place, e.g. by coupling to a microcavity^{7,9,11}. Narrowing the QD emission ensemble during growth³² and adding a large-range frequency-tuning capability via external strain^{64,72} can also speed up the process.

Experimental results of one-QD HOM are visible in Fig. 6.1(c, d) and Appendix Fig. A.6, A.7. In these measurements, photons from a single QD are filtered by a broad-band grating-based filter (22 GHz) and then sent into a Mach-Zehnder Interferometer. After the interferometer, the photons are counted by two superconducting nanowire single-photon detectors (SNSPDs) and analysed by a time-to-digital converter. The bin size of the time-to-digital converter is set to 100 ps. The data, e.g. as shown in Fig. 6.1(c), is integrated for 320 minutes with a count rate of 2 kHz per detector (HOM \parallel). Summing up the coincidence counts for each peak using a 13 ns time-window [HOM \parallel , Fig. 6.1(c)], we have 20 counts for the central peak and 942 counts on average for the side peaks except for the first ones. For HOM \perp , the experiment is integrated until the side peaks have similar counts compared to HOM \parallel . We collect on average 1038 counts for the side peaks and 536 counts for the central peaks. The raw remote-QD HOM visibility (for QD2) is calculated by $\mathcal{V}_{\text{raw}}^{13 \text{ ns}} = 1 - (\frac{20}{942}) / (\frac{536}{1038}) = 95.8\%$.

To determine the true overlap \mathcal{V} of the two single-photon states produced by the QDs, we account for the finite $g^{(2)}(0)$ and for imperfections in the setup (the imperfect classical interference visibility and the small imbalance in the “50:50” beamsplitter). For the finite $g^{(2)}(0)$ value (likely caused by a re-excitation process^{79,169}), we assume that the two photons in the occasionally created $|2\rangle$ -state are distinguishable¹¹.

For one-QD HOM measurements, we follow the calculations in Ref. 158 and arrive at:

$$\mathcal{V} = \frac{1}{(1 - \epsilon)^2} \left(\frac{R^2 + T^2}{2RT} \right) \left[1 + 2 \cdot g^{(2)}(0) \right] \mathcal{V}_{\text{raw}}. \quad (6.2)$$

Here, R and T are the reflection and transmission coefficients of the beamsplitter, and $(1 - \epsilon)$ is the classical visibility of the interferometer. For the one-QD HOM setup, $R = 0.490$ and $T = 0.510$; the classical visibility $(1 - \epsilon)$ is 0.998 for $\mathcal{D} = 13$ ns, and 0.995 for $\mathcal{D} = 1.01$ μs .

Experimental results of two-QD HOM are shown in Fig. 6.2(b) and in Appendix Fig. A.10. Here, single-photons from independent QDs are adjusted to the same intensity and then simply sent to a 50:50 beamsplitter (see Appendix Sec. A.3). The bin size of the time-to-digital converter is set to 100 ps. The data shown in Fig. 6.2(b) is integrated for 145 minutes with a count-rate of on average 4 kHz per detector (HOM \parallel). In total, we collect 89 coincidence counts in the central peak (no post-selection), and on average 1832 counts for the side-peaks. For HOM \perp , we have a similar count-rate. We integrate until the side-peaks reaches a similar intensity of the HOM \parallel case. In total, we collect 942 coincidence counts in the central peak and 1768 counts on the side. The raw two-QD HOM visibility (for QD1/QD2) is thus calculated by $\mathcal{V}_{\text{raw}}^{\text{remote}} = 1 - (\frac{89}{1832}) / (\frac{942}{1768}) = 90.9\%$.

To calculate the true two-QD HOM visibilities, the major difference compared to the one-QD HOM is the absence of the Mach-Zehnder interferometer in the optical setup. The first beamsplitter in the Mach-Zehnder interferometer gives rise to the factor of two in front of the $g^{(2)}(0)$ in Eq. 6.2. Moreover, for the two-QD HOM, the $g^{(2)}(0)$ s of both QDs are taken into account.

We outline the derivation for the true remote-QD HOM visibility \mathcal{V} in the Appendix. We arrive at:

$$\mathcal{V} = \frac{1}{(1 - \epsilon)^2} \left(\frac{R^2 + T^2}{2RT} \right) \left[1 + \frac{1}{2} \left(g_{\text{QD}_1}^{(2)}(0) + g_{\text{QD}_2}^{(2)}(0) \right) \right] \mathcal{V}_{\text{raw}}, \quad (6.3)$$

with i, j denoting the two QDs. For the two-QD HOM setup, $R = 0.498$ and $T = 0.502$; the classical visibility $(1 - \epsilon) = 0.996$.

To model the HOM interference between the photons generated by remote QDs, we adopt the analytical treatment developed in Ref. 164. The result for the HOM visibility (see Appendix for derivation) is:

$$\mathcal{V} = \frac{2(\gamma + \Xi\pi)}{(\gamma + \Xi\pi)^2 + 4\pi^2\Delta^2} \cdot \frac{e^{-|\delta t|/\tau_e}}{(\tau_i + \tau_j)}. \quad (6.4)$$

Here, δt and Δ represent the temporal delay and spectral detuning, respectively, of one wave-packet with respect to the other. $\tau_{i,j}$ stands for the radiative lifetime of the two QDs, and τ_e is the lifetime of the “early” photon ($e = i$ or j). γ is the overall phase relaxation-rate, $\gamma = \gamma_i + \gamma_j$, where $\gamma_{i,j} = 1/(2\tau_{i,j}) + \Gamma_{i,j}^*$. $\Gamma_{i,j}^*$ and Ξ are included to model the effects of phonon-induced pure dephasing and spectral fluctuation processes, respectively. In Eq. 6.4, we assume the total spectral fluctuations of the two QDs follow a Lorentzian distribution in frequency with a full-width-at-half-maximum of Ξ . Assuming identical QDs, $\Gamma_{i,j}^* = \pi\Delta\nu_H$, $\Xi = 2\Delta\nu_S$, with $\Delta\nu_H$ and $\Delta\nu_S$ representing the homogeneous and inhomogeneous linewidth broadening of each QD, respectively. In the case of $\delta t = 0$ and $\Delta = 0$, Eq. 6.4 simplifies to Eq. 6.1.

Utilising Eq. 6.4, we estimate the effects of both pure dephasing and spectral fluctuations on the remote-QD HOM experiments – we determine $\Gamma_{i,j}^* = 34 \pm 25$ MHz and $\Xi = 2 \times (34 \pm 15)$ MHz (Appendix Sec. A.3.B). In the time domain, the exciton dephasing rate corresponds to a T_2 -like time of 29 ± 21 ns; the spectral fluctuations correspond to a T_2^* -like time of 9.1 ± 3.9 ns.

We evaluate the temporal post-selection effect – reducing the evaluation time window effectively increase the $\mathcal{V}^{\text{remote}}$ at an expense of the photon count-rate [see Fig. 6.4(c,d)]. In our case, reducing the window to $T_{\text{bin}} = 3/\Gamma$ in the remote-QD HOM analysis, the measured visibility is lifted to $\mathcal{V}_{\text{filter}}^{\text{remote}} \sim 97\%$. Here, $1/\Gamma$ represents the average lifetime of the two QDs.

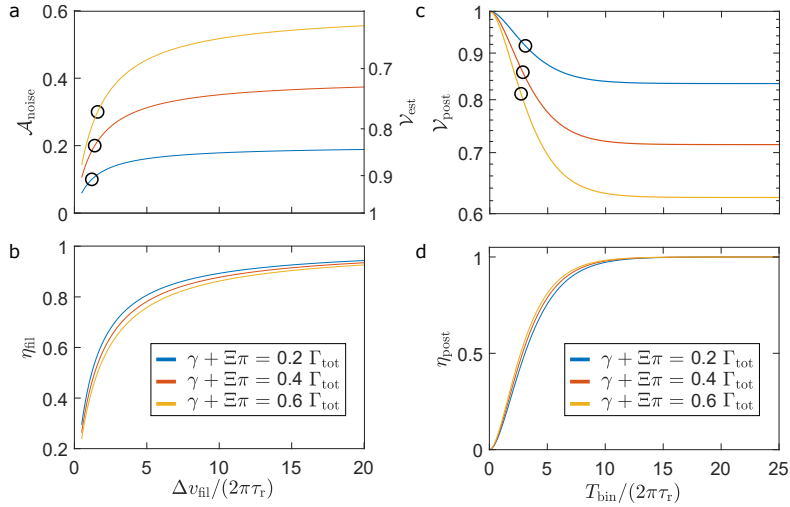


Fig. 6.4. **The effects of spectral filtering and temporal post-selection on two-photon interference from remote quantum dots.** (a) The effect of spectral filtering as a function of the filter bandwidth Δv_{fil} . We assume that the transmission function of the spectral filter has a Lorentzian profile (e.g. for an etalon). Δv_{fil} is normalised by the QD's radiative rate $1/(2\pi\tau_r)$ (assuming identical QDs). $\mathcal{A}_{\text{noise}}$ is an indicator of the spectral filtering effect. It is defined as the ratio between the noise-related linewidth broadening and the QD's intrinsic linewidth. Here, the noise includes both spectral fluctuation and exciton dephasing, leading to Lorentzian linewidth broadening. Both the intrinsic and the noise part of the QD spectrum experience spectral filtering effect, but their ratio $\mathcal{A}_{\text{noise}}$ decreases as the filter narrows. However, this filtering effect becomes only apparent when the filter is narrow, e.g. $\Delta v_{\text{fil}}(2\pi\tau_r) < 5$. Different coloured lines represent different levels of noise, characterised by $\gamma + \Xi\pi$. For example, the blue curve represents the case when total noise in the two QDs are 20% of the total radiative rate. On the right y-axis, we plot the estimated remote-QD HOM visibility, \mathcal{V}_{est} . Here, this visibility is only an estimated value based on Eq. 6.2. (b) The effect of spectral filtering on the photon counts. η_{fil} represents the percentage of photons exiting a spectral filter compared to the photons before filtering. Here, the peak transmission of the filter is set to unity and the filter is centred at the QD resonance. We find that when $\Delta v_{\text{fil}}(2\pi\tau_r) < 5$ the photon counts are strongly reduced. Taking $\eta_{\text{fil}} = 0.5$ as a limit, we plot the corresponding filtering effect on remote-HOM visibility in black circles in (a). Scarifying more than 50% efficiency makes little sense for creating a large number of single-photons – in that case, an individual QD source simply outperforms multiple QDs. (c) The effect of temporal post-selection on remote-QD HOM interference as a function of the evaluation time-window T_{bin} . Performing temporal post-selection with a narrow T_{bin} leads to an increase in remote-QD HOM visibility $\mathcal{V}_{\text{post}}$ at the expense of coincidence count-rates. Here, the colour lines also represent the different noise conditions. (d) The effect of temporal post-selection on coincidence counts. η_{fil} is defined as the ratio between the total coincidence events after temporal post-selection compared to the no post-selection case. Taking $\eta_{\text{fil}} = 0.5$ as a limit, we determine how much $\mathcal{V}_{\text{post}}$ benefits from the temporal post-selection. This is seen as the black circles in (c).

Chapter 7

Conclusions and Outlook

This thesis describes the development of low-noise GaAs QDs and their applications towards practical single-photon sources. The ultra-low noise in GaAs QDs is made possible with the help of a working *n-i-p* diode structure. The design of the diode structure is shown in Chapter 3. Compared to standard GaAs QDs in the bulk, the diode structure allows deterministic control of the QD's charge states. Separate charge plateaus of X^{1+} , X^0 and X^{1-} can be created by an external gate voltage. Near-lifetime-limited linewidths are resolved in resonance fluorescence. Blinking is absent in the emission. Both the near-optimal linewidth and elimination of blinking are consequences of the low level of noise.

Direct evidence of the noise in the diode structure is the characterisation of the photon indistinguishability. The photons from individual GaAs QDs exhibit a high level of indistinguishability. Interestingly, the indistinguishability remains near-unity even if the GaAs QD photons are created with a temporal separation of $1 \mu\text{s}$. The environment of the low-noise GaAs QDs is static over a long timescale.

The low-noise GaAs QDs can be connected via single photons. When interfering the photons created by separate GaAs QDs in a Hong-Ou-Mandel experiment, a visibility of 93% is realised (see Chapter 6). The near-unity visibility is a leap compared to the previous experiments on InGaAs QDs and GaAs QDs. The high visibility paves the way to employing multiple GaAs QDs as single-photon sources for advanced photonic applications. As a proof-of-principle experiment, a controlled-not gate using photons from two separate sources is realised, where high process fidelity as well as entangling ability are demonstrated.

The ultra-low noise in GaAs QDs is ideal for many relevant fundamental studies. In Chapter 4, the radiative Auger process in GaAs QDs is investigated. It was discovered that the radiative Auger process not only takes place in the QD emission but can also be optically addressed. The radiative Auger and the fundamental transitions form a Λ -system, which might open up the possibility of carrying out Terahertz spectroscopy

on single quantum emitters. In Chapter 5, electron-nuclear spin interactions are experimentally studied. In a two-laser experiment, nuclear spins are shown to modify the coherent population trapping condition in the GaAs quantum-dot system depending on either the blue-Zeeman or the red-Zeeman transition is addressed. A detailed theoretical model is still under investigation.

As a brief outlook, some future directions are outlined as follows.

For practical applications, an immediate step forward is to improve the GaAs QD source's collection efficiency. This can be achieved by coupling the low-noise GaAs QDs to a single optical mode in photonic nanostructures. Fortunately, most of the nanophotonics engineering techniques developed for InGaAs QDs can be adopted to GaAs QDs. For example, designing a diode structure in a nano-membrane enables the integration of GaAs QDs with on-chip nanobeam-waveguides and photonic crystal cavities¹⁴⁸. A suitable heterostructure together with a curved top-mirror allows the low-noise GaAs QDs to couple to a tunable micro-cavity¹¹.

Coupling the GaAs QD to a single-optical mode not only leads to an increase in collection efficiency but also improves the photon indistinguishability thanks to the Purcell effect⁹. Assuming the present noise level can be maintained, a moderate Purcell enhancement of $F_p = 10$ could boost the single-QD and separate-QD indistinguishability to well above 99.5% and above 99.0%, respectively. A boost in collection efficiency also points to the storage of high-quality single-photons from low-noise GaAs QDs to a rubidium vapour quantum memory. Based on the current signal-to-noise level of the rubidium memory⁵², a single-shot storage experiment requires an end-to-end source efficiency of $\sim 25\%$. Such efficiency is achievable with proper photonic engineering.

Long electron-spin relaxation time can open up the possibility to study spin qubits in low-noise GaAs QDs. An interesting experiment is to measure the electron and hole-spin coherence time in the low-noise GaAs QDs. To control the electron-spin, the method proposed by Bodey et al.²³ can be adopted. The challenges here are the tiny electron g -factor – high magnetic field might be required. The quadrupolar interaction could be induced by adding uniaxial strain to the QDs, e.g. using the strain-amplification device described in Chapter 2. If the coherence time is long, an intermediate step could point to the creation of a 1D cluster state via spin-rotations²⁶ and entangling remote-QD spins.

Furthermore, the low-noise GaAs QDs are a promising platform for the generation of blinking-free entangled photon-pairs¹⁷⁰. The challenges here lie in controlling the fine-structure splitting and improving the collection efficiency.

Appendix A

Details on

“Quantum Interference of Identical Photons from Remote Quantum Dots”

In this Appendix, we provide additional information regarding the experiments described in Chapter 6.

A.1 Heterostructure Design and Characterisation

QD1 and QD2 are located in two separate pieces of a wafer grown by molecular beam epitaxy⁴ (MBE). The heterostructure consists of an *n-i-p* diode³⁷ that is designed for operation at cryogenic temperatures. The GaAs quantum dots (QDs) are grown on an intrinsic $\text{Al}_{0.33}\text{Ga}_{0.67}\text{As}$ matrix using a local droplet etching technique^{13,14}. For the *n*- and *p*-doped layers, $\text{Al}_{0.15}\text{Ga}_{0.85}\text{As}$ instead of $\text{Al}_{0.33}\text{Ga}_{0.67}\text{As}$ is used to avoid the formation of DX centres⁹¹. The detailed heterostructure design and growth parameters are identical to those of Ref. 37.

The *n-i-p* diode enables deterministic control of the QD charge by Coulomb blockade³. An example is shown in Fig. A.1(a) for QD2. The photoluminescence undergoes abrupt jumps, i.e. the charge states appear one after another as the gate voltage increases. The three excitons which can be resonantly excited are labelled: the positive trion X^+ , the neutral exciton X^0 and the negative trion X^- . The heterostructure design also allows large-range frequency tuning within one charge plateau via the quantum-confined Stark effect. The tuning range R is typically above 200 GHz, much larger than the QD linewidths. This is exploited in the resonance fluorescence charge plateaus on X^- of both QD1 and QD2 [Fig. A.1(b,c)], where the precise adjustments of the two external gate voltages V_g bring the two QDs into resonance. Compared to the full-width-at-half-maximum of the emission ensemble, $W = 11$ nm or equivalently 5.4 THz, the Stark

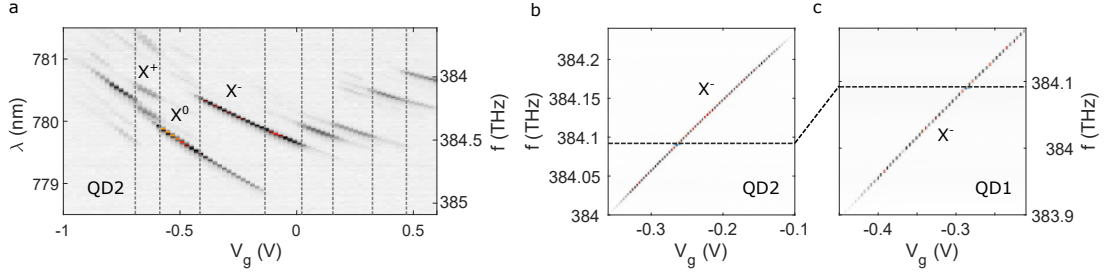


Fig. A.1. **Photoluminescence and resonance fluorescence charge plateaus** (a) Photoluminescence from QD2 as a function of the externally applied gate voltage, V_g . (b) Resonance fluorescence on X^- from QD2. Resonance fluorescence is mapped out by scanning both the laser frequency and the gate voltage. The signal is collected using a polarisation-based dark-field microscope. The dashed line indicates the frequency at which all the experiments on QD2 are performed. (c) Resonance fluorescence on X^- from QD1. The dashed line represents the same frequency as in (b).

tuning range covers $R/W > 3.6\%$, much larger than the typical tuning capability of InGaAs QDs. This large-range frequency tuning spares the tedious searching process for frequency-matched emitters.

The GaAs QDs in the $n-i-p$ diode system exhibit very little noise under continuous-wave (CW) excitation. This is revealed by their near-lifetime-limited optical linewidths. In Fig. A.2, we show lifetime- and linewidth-measurements for QD 1, 2, 3 and their associated data-fittings (QD3 is on the same wafer piece as QD2). The extracted decay rates for the three QDs are $\Gamma_1 = 3.75$ GHz, $\Gamma_2 = 3.91$ GHz and $\Gamma_3 = 3.54$ GHz, respectively. This corresponds to lifetime-limited optical linewidths of $\Gamma_1/2\pi = 597$ MHz, $\Gamma_2/2\pi = 623$ MHz and $\Gamma_3/2\pi = 564$ MHz. The measured linewidths for QD 1 – 3 are just 8.4%, 9.6%, and 14.0% above the lifetime limit. The narrow linewidths are a general feature of the GaAs QD diode system – similarly-narrow linewidths (linewidths less than 20% above the transform limit) are easy to find³⁷. In addition, the GaAs QDs in the diode system are free from blinking. Blinking, random telegraph noise in the intensity of QD emission, results in a bunching in an auto-correlation measurement. In our system, no bunching is observed, indicating that the blinking is eliminated³⁷.

Photons from GaAs QDs are collected by an aspheric lens ($NA = 0.71$) and a dark-field microscope. The dark-field microscope relies on a cross-polarisation scheme⁷⁵ to separate the QD photons from the excitation laser. There is an intrinsic loss of 50%. The microscope has an overall efficiency of 15% - 20%. The collection efficiency of the setup is characterised under resonant pulsed excitation. The QD photons are counted by an avalanche photodiode ($\sim 70\%$ detection efficiency at 780 nm). The connection loss to the avalanche photodiode (APD) is around 1 dB. At the APD, we detect 150 kHz - 200 kHz

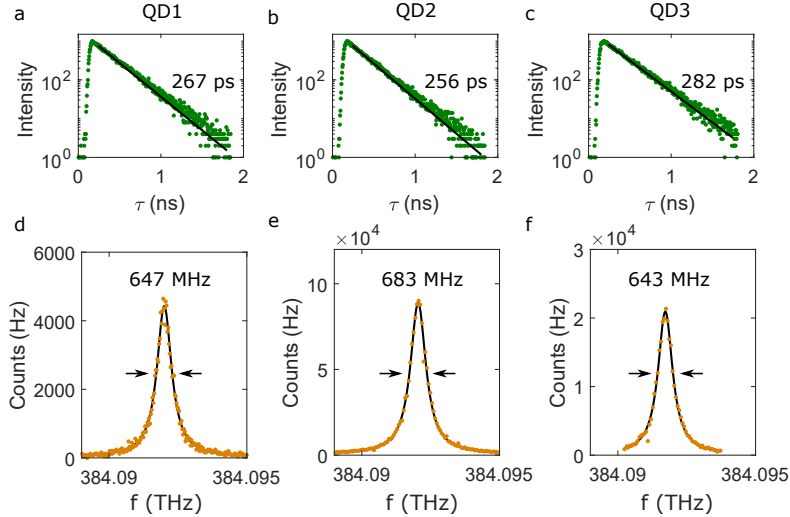


Fig. A.2. **Lifetimes and linewidths of X^- in three quantum dots.** (a-c) Time-resolved resonance fluorescence of QD 1 - 3 under resonant picosecond pulsed excitation. The resonance fluorescence intensity of each QD follows an exponential decay. From the fits (black curves), the radiative decay rates are extracted as $\Gamma_1 = 3.75$ GHz, $\Gamma_2 = 3.91$ GHz and $\Gamma_3 = 3.54$ GHz. The corresponding lifetimes are displayed next to the exponential fits. The radiative lifetimes of GaAs QDs are typically¹³ 250 ps. In our sample, the average lifetime is around 300 ps – there is no sign of any Purcell enhancement. (d-f) Resonance fluorescence spectrum obtained by slowly scanning a narrow-bandwidth continuous-wave (CW) laser across the X^- . The typical measurement time is 5 - 10 minutes – the linewidth probes the noise over a huge frequency bandwidth. Nonetheless, the measured linewidths (values are displayed next to the fits) are very close to the lifetime limits.

photons out of a 76.3 MHz repetition rate. This corresponds to a collection efficiency of 0.3% – 0.4% from emitter to detector. Taking into account the setup imperfections, the single-photons are collected by the first lens with an efficiency of $\sim 2.3\%$.

A.2 Hong-Ou-Mandel Interference from Single GaAs Quantum Dots

In the Hong-Ou-Mandel (HOM) as well as the associated Hanbury Brown-Twiss experiments, QD photons pass through a 22 GHz-bandwidth grating-based filter. The grating (WasatchPhotonics, 1650 l/cm at 781 nm) has an efficiency of $\sim 80\%$. As the picosecond pulsed laser is spectrally broad (~ 150 GHz), the 22 GHz-bandwidth filter helps remove back-scattered laser light in the detection channel¹⁸. It is also essential to filter out the weak phonon sideband (which constitutes 4% of the emission; the full width at half maximum is ~ 0.6 nm or 240 GHz, see Fig. A.4) and the even weaker radiative

Auger emission³⁸ (~ 3 THz away from the resonance fluorescence). The filter has little impact on the spectral (or temporal) profile of the resonance fluorescence photons (see Fig. A.3), since the grating's bandwidth is ~ 40 times larger than the QDs' linewidth. Therefore, the grating filter induces negligible spectral filtering effects to the zero-phonon line emission.

The one-QD HOM experiments are performed using the Mach-Zehnder interferometer sketched in Fig. A.5. The photons are split equally into two arms and overlap on a fibre-based 50:50 beamsplitter. The photons travelling through the long arm experience a delay \mathcal{D} compared to the shorter arm. In our experiments, we finely adjust the movable delay so that the delayed photon matches temporally with the \mathcal{N} th successively emitted photon. For $\mathcal{N} = 1$, $\mathcal{D} = 13$ ns; for $\mathcal{N} = 77$, $\mathcal{D} = 1.01$ μ s. To characterise the HOM visibility, photons in the two arms are prepared in the same (HOM \parallel) and in the opposite polarisation (HOM \perp). A fibre-based polarisation controller is used to maximise (minimise) the classical interference visibility of the two arms when they are co-polarised (cross-polarised). For $\mathcal{D} = 13$ ns, the classical interference visibility is 99.8% (co-polarised) and 1.0% (cross-polarised); for $\mathcal{D} = 1.01$ μ s, the contrast is slightly reduced to 99.5%/1.5% by the 200-metre fibre. At the two output ports of the beamsplitter, quantum interference of the QD photons is recorded using two superconducting nanowire single-photon detectors (SNSPDs) and a photon-counting hardware (Time Tagger Ultra, Swabian Instruments).

The raw HOM data of QD1 and QD2 are presented in Fig. A.6 and Fig. A.7 for the 13 ns and 1.01 μ s delay, respectively. For the 13 ns case (1.01 μ s case), the intensity of the 1st (77th) side peaks is 75% compared to the other side peaks. This is a result of the route probability in the Mach-Zehnder interferometer. Since the QD creates single photons, a photon arrived at the first 50:50 beamsplitter is either transmitted, making its way to the short path of the interferometer, or reflected to the long arm. Thus, for two photons to be counted coincidentally, there exist four probabilities: (i) both the two photons enter the long path, (ii) both enter the short path, (iii) the early photon enters the short path and the late photon in the long path, and (iv) the early in the long and the late in the short path. Depending on the route, the Mach-Zehnder interferometer induces different temporal delays to the photon pairs. To be specific, for (i,ii) there is no added delay, for (iii) a delay of $\mathcal{D} = \mathcal{N}T_{\text{period}}$ is induced, and for (iv) $-\mathcal{D}$ is induced. For all the side peaks except for the \mathcal{N}^{th} ones, all four probabilities contribute to the coincidence counts. For the \mathcal{N}^{th} side peaks, three out of four probabilities are accounted for. The missing probability is due to the fact that the two photons can not be emitted at the same time. (If there are two photons arriving at the first beamsplitter at the same

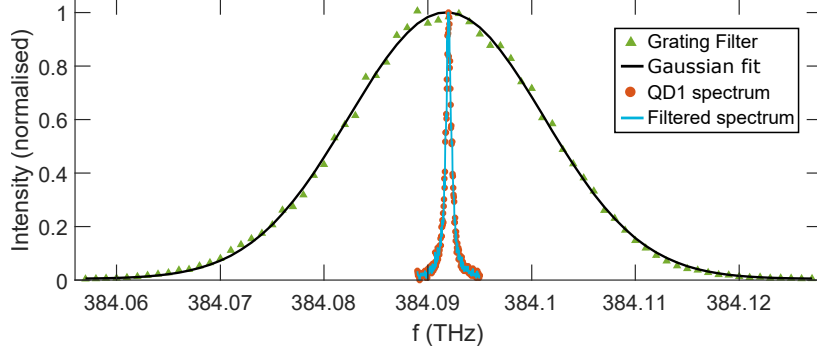


Fig. A.3. **The grating filter and its effect on quantum dot linewidths.** Green triangles represent the frequency dependence of the grating setup. The grating is aligned such that the first-order diffraction is focused by an achromatic lens ($f = 50$ mm) into a single-mode optical fibre. The grating filter has a bandwidth of 22.1 GHz (full-width-at-half-maximum) and follows a Gaussian profile (black curve) and is centred around the QDs' spectrum. The red circles show the measured QD1 resonance fluorescence spectrum without passing through the grating, while the blue solid curve represents the expected spectrum with the grating filter in place. The perfect overlap between the red circles and the blue line confirms that the grating filter has little impact on the QD lineshape.

time, then adding or subtracting a delay \mathcal{D} leads to coincidence counts at the \mathcal{N}^{th} side peaks.) This is the reason why the 1st and the 77th side peaks are only 75% intensity in Fig. A.6 and Fig. A.7.

The raw visibility of the HOM interference is calculated as the ratio of the normalised area underneath the central peaks for the co- and cross-polarised measurements, $\mathcal{V}_{\text{raw}} = 1 - \frac{A_{\parallel}}{A_{\perp}}$. For the area calculation, we take into account the whole pulse period, i.e. $T_{\text{bin}} = 13$ ns. This binning size is ~ 50 times larger than the QD's lifetime – no temporal post-selection is introduced.

Experimental imperfections as well as the finite value of $g^{(2)}(0)$ influence the measured HOM visibility \mathcal{V}_{raw} . The second-order correlation functions $g^{(2)}(0)$ of the two QDs are measured in Hanbury Brown-Twiss measurements^{72,95}. For this, we block one arm of the Mach-Zehnder interferometer and send the QD photons through the symmetric beamsplitter. The results are shown in Fig. A.8. We extract the $g^{(2)}(0)$ from the normalised central peak intensity: $g^{(2)}(0) = (1.3 \pm 0.2)\%$ for QD1 and $g^{(2)}(0) = (1.0 \pm 0.1)\%$ for QD2. Following Eq. 6.2, we arrive at $\mathcal{V}^{13\text{ns}} = (97.8 \pm 1.8)\%$ and $\mathcal{V}^{1\mu\text{s}} = (99.0^{+1.0}_{-1.8})\%$ for QD1, and $\mathcal{V}^{13\text{ns}} = (98.2 \pm 1.3)\%$, $\mathcal{V}^{1\mu\text{s}} = (98.7^{+1.3}_{-2.0})\%$ for QD2.

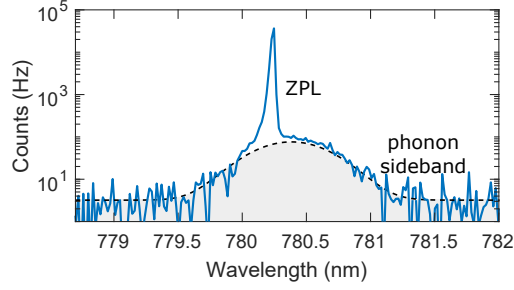


Fig. A.4. **The zero-phonon line and the phonon sideband in resonance fluorescence.** The resonance fluorescence is spectrally resolved with a spectrometer on tuning a CW laser into resonance with the QD2 X^- . The black dashed curve represents a guide to the eye for the phonon sideband. The zero-phonon line (ZPL) contributes 96% to the resonance fluorescence spectrum.

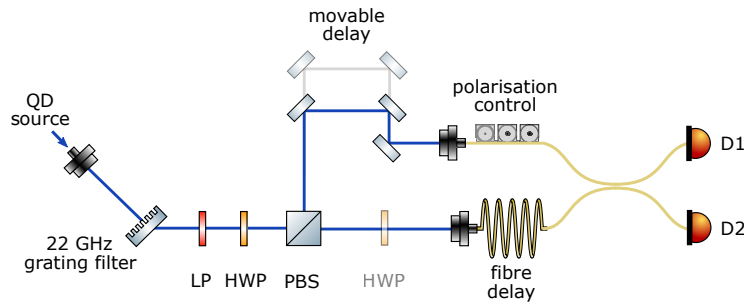


Fig. A.5. **Interferometry setup for one-QD Hong-Ou-Mandel experiments.** The QD photons are passed through a 22 GHz-bandwidth grating filter and sent to an unbalanced Mach-Zehnder interferometer. The interferometer has a “long” arm with an exchangeable fibre delay, and a “short” arm on a manual delay line. A linear polariser (LP), a half-wave plate (HWP), and a polarising beamsplitter (PBS) are used to balance the power in the two arms. The inserted fibre is 2-metre long for 13 ns ($\mathcal{N} = 1$) delay and 200-metre long for $1.01 \mu\text{s}$ delay ($\mathcal{N} = 77$). The photons travelling through the two arms impinge on a fibre-based 50:50 beamsplitter. The temporal overlap of the two arms is carefully adjusted by the movable delay line. A HWP in the long arm is employed on changing from the co-polarised configuration to the cross-polarised configuration. The photons in the two outputs are counted using two superconducting nanowire single-photon detectors (D_1 and D_2) and a streaming time-to-digital converter.

A.3 Hong-Ou-Mandel Interference from Two Remote Quantum Dots

To test the indistinguishability of photons from remote GaAs QDs, we employ the setup in Fig. A.9. We synchronise the excitation of the two QDs so that the two photons from the distant QDs arrive simultaneously at a 50:50 fibre-based beamsplitter. The synchronisation is achieved with a precision of ± 4 ps by both a movable delay line and an exchangeable fibre delay in the excitation paths. Back-reflected laser light is

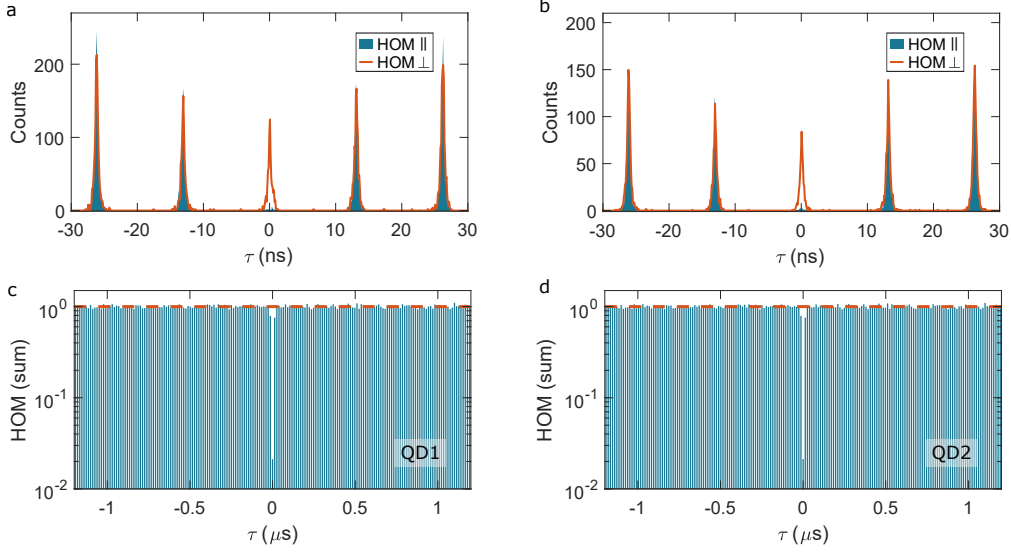


Fig. A.6. **Hong-Ou-Mandel interference between 13 ns-delayed photons from individual GaAs quantum dots.** (a,b) Time-resolved HOM interference in co-polarised (cyan) and cross-polarised (red) configurations for QD1 (a) and QD2 (b). The raw HOM visibility is extracted by calculating the ratio between the central peak areas in the two configurations. The area comprises the sum of all coincidence events in one pulse period around the zeroth peak, i.e. from $\tau = -6.5$ ns to $\tau = +6.5$ ns and is normalised by that of the side peaks. (c,d) The normalised HOM interference in co-polarised configuration for the two QDs. Each bar represents the sum of coincidence events around the peak at the corresponding τ using the full pulse period as the time binning window, $T_{\text{bin}} = 13$ ns. The intensities of the bars are normalised at very long delay. The normalised HOM bars are flat showing an elimination of blinking. The intensity of the first bars ($i = \pm 1$) drops to 75% due to route probability, indicating that the quantum interference is measured between the consecutively emitted photons ($\mathcal{N} = 1$).

rejected using a dark-field microscope⁷⁵ on each cryostat. Single photons from the two QDs pass through a half-wave plate (HWP) and a polarising beamsplitter (PBS) in the two separate collection paths – where the photon fluxes from both QDs are matched. 22 GHz-bandwidth grating filters are inserted before the SNSPDs to improve the laser suppression and to remove the phonon sideband and radiative Auger emissions³⁸.

The HOM interference of remote-QD photons is shown in Fig. A.10. The raw HOM visibilities for photons generated between QD1 and QD2 (90.8%) and between QD1 and QD3 (90.6%) are very similar. In analogy to the one-QD HOM, experimental imperfections and the finite $g^{(2)}(0)$ are accounted for in order to determine the true overlap \mathcal{V} from the raw HOM visibility \mathcal{V}_{raw} .

We outline the derivation of the relationship between \mathcal{V}_{raw} and \mathcal{V} . Considering two photons incident on a beamsplitter ($\tilde{B}S$) from the two input ports “ i ” and “ j ”, the

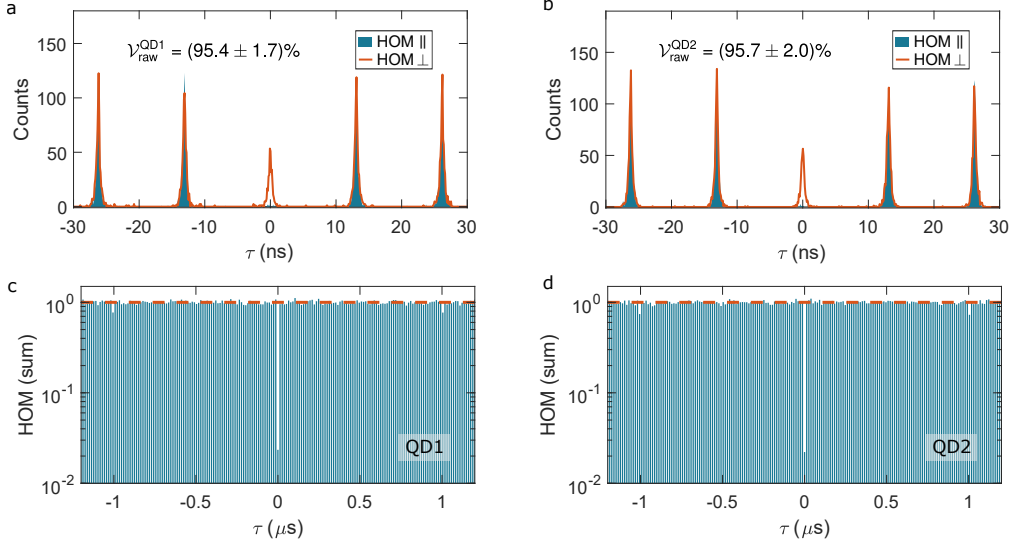


Fig. A.7. **Hong-Ou-Mandel interference between 1.01 μs -delayed photons from individual GaAs quantum dots.** (a,b) The time-resolved HOM interference in co-polarised (cyan) and cross-polarised (red) configurations for QD1 and QD2. (c,d) The normalised HOM interference in the co-polarised configuration for the two QDs. The time bin is $T_{\text{bin}} = 13$ ns for every bar. The normalised HOM bars are flat out to a microsecond. The intensity of the 77th bars ($i = \pm 77$) drops to 75% due to route probability, indicating that the quantum interference is measured between the photons emitted 77 pulse periods apart ($\mathcal{N} = 77$).

output after the beamsplitter in ports “ k ” and “ l ” can be calculated via:

$$|\text{out}\rangle = \tilde{BS} |1_i, 1_j\rangle = t^2 |1_l, 1_k\rangle - r^2 |1_l, 1_k\rangle + i\sqrt{2}rt \left(|2_l, 0_k\rangle + |0_l, 2_k\rangle \right), \quad (\text{A.1})$$

where $t^2 = T$ ($r^2 = R$) is the transmission (reflection) coefficient of the beamsplitter. The visibility of two-photon quantum interference for an ideal input $|1_i, 1_j\rangle$ is hence given by

$$\mathcal{V}_Q = (t^2 - r^2)^2 = 1 - 4RT. \quad (\text{A.2})$$

Here, we make use of the relation $T^2 + R^2 = 1$ and assume the two input photons are completely indistinguishable. When the two input photons are distinguishable, all quantum effects disappear, and we arrive at the classical visibility:

$$\mathcal{V}_C = |t^2|^2 + |r^2|^2 = 1 - 2RT. \quad (\text{A.3})$$

The visibility in the case of quantum interference can be further expressed as:

$$\mathcal{V}_Q = \mathcal{V}_C - (1 - \epsilon)^2 \mathcal{V}(2RT). \quad (\text{A.4})$$

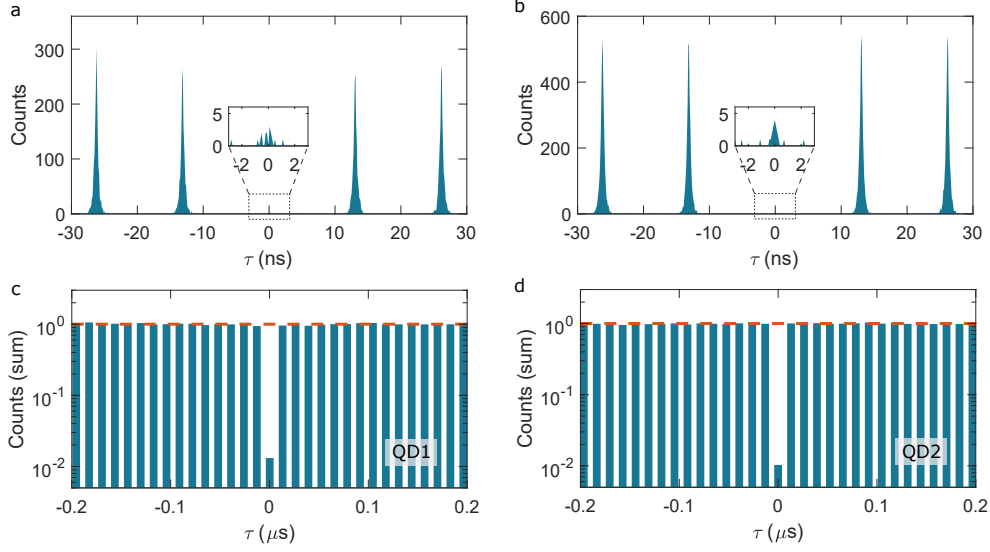


Fig. A.8. **Hanbury Brown-Twiss measurements on QD1 and QD2.** (a,b) Time-resolved auto-correlation of QD1 (a) and QD2 (b). The central peak in each plot is enlarged and displayed as an inset. The ratio between the central peak intensity and the average intensity of the side peaks defines $g^{(2)}(0)$. These ratios are more clearly visible in (c,d), where coincidence counts in the time-resolved measurements are summed up peak by peak and normalised at long delays. The time bin is a whole pulse period. The central peak for both QDs reduces to $\sim 1\%$ indicating a high single-photon purity. The small but finite $g^{(2)}(0)$ comes likely from a re-excitation process.

Here, we introduce imperfections in the polarisation overlap of the photons from the two QDs, quantified by the classical interference visibility $(1 - \epsilon)$. \mathcal{V} represents the true two-photon overlap of the $|1_i, 1_j\rangle$ state.

Due to the finite $g^{(2)}(0)$ in the QD emission, the input states on the beamsplitter contain small multi-photon components with probabilities $P_n^{\text{QD}_m}$,

$$|\psi_{\text{in}}^{\text{QD}_m}\rangle = P_0^{\text{QD}_m} |0\rangle + P_1^{\text{QD}_m} |1\rangle + P_2^{\text{QD}_m} |2\rangle + \dots \quad (\text{A.5})$$

where $m = i, j$ denotes the emitters at the two input ports and $n = 0, 1, 2, \dots$ represents the number of photons created by the π -pulse excitation. As the excitation pulse width is very short compared to the QD lifetime, the probability of creating the two-photon component by the π -pulse is much smaller than that of creating a single-photon state¹⁶⁹, i.e. $P_2^{\text{QD}_m} \ll P_1^{\text{QD}_m}$. We can relate $P_1^{\text{QD}_m}$ and $P_2^{\text{QD}_m}$ to the second-order correlation function $g^{(2)}(0)$ via:

$$g_{\text{QD}_m}^{(2)} \simeq \frac{2 \cdot P_2^{\text{QD}_m}}{(P_1^{\text{QD}_m})^2}. \quad (\text{A.6})$$

Using this relation, the HOM probabilities for the $|1_i, 1_j\rangle$ and $|0_i, 2_j\rangle, |2_i, 0_j\rangle$ input states are expressed as:

$$\text{HOM}_{11} = P_1^{\text{QD}_i} P_1^{\text{QD}_j} (T - R)^2 \quad (\text{A.7})$$

$$\text{HOM}_{20,02} = \frac{1}{2} \left[g_{\text{QD}_i}^{(2)} \left(P_1^{\text{QD}_i} \right)^2 + g_{\text{QD}_j}^{(2)} \left(P_1^{\text{QD}_j} \right)^2 \right] (2RT). \quad (\text{A.8})$$

Substituting Eq. A.4 into HOM_{11} and assuming a slight imbalance in the two input photon-fluxes, i.e. $P_1^{\text{QD}_i} \approx P_1^{\text{QD}_j} + \eta$, the overall \mathcal{V}_Q probability is given by $\mathcal{V}_Q = \text{HOM}_{11} + \text{HOM}_{20,02}$ with:

$$\text{HOM}_{11} = P_1^{\text{QD}_i} (P_1^{\text{QD}_i} + \eta) [1 - 2RT - 2RT(1 - \epsilon)^2 \mathcal{V}], \quad (\text{A.9})$$

$$\text{HOM}_{20,02} = P_1^{\text{QD}_i} \cdot \frac{1}{2} \left[(g_{\text{QD}_i}^{(2)} + g_{\text{QD}_j}^{(2)}) (P_1^{\text{QD}_i} + \eta) + (g_{\text{QD}_i}^{(2)} - g_{\text{QD}_j}^{(2)}) \eta \right] (2RT). \quad (\text{A.10})$$

The last term in $\text{HOM}_{20,02}$ vanishes since the difference in $g_{\text{QD}_i}^{(2)}$ and $g_{\text{QD}_j}^{(2)}$ is typically small, i.e. $(g_{\text{QD}_i}^{(2)} - g_{\text{QD}_j}^{(2)}) \eta \sim 0$. Setting $\mathcal{V} = 0$ in the \mathcal{V}_Q expression, we arrive at the overall \mathcal{V}_C probability – if taking the small 2-photon component into consideration. Hence, we can extract the corrected visibility \mathcal{V} from the raw visibility using $\mathcal{V}_{\text{raw}} = (\mathcal{V}_C - \mathcal{V}_Q) / \mathcal{V}_C$. The result reads:

$$\mathcal{V} = \frac{1}{(1 - \epsilon)^2} \frac{R^2 + T^2}{2RT} \left[1 + \frac{1}{2} \left(g_{\text{QD}_i}^{(2)}(0) + g_{\text{QD}_j}^{(2)}(0) \right) \right] \mathcal{V}_{\text{raw}}. \quad (\text{A.11})$$

From Eq. A.11, we extract the true indistinguishability of the two-QD photons: $\mathcal{V}^{\text{QD1}/2} = (93.0 \pm 0.8)\%$ for the photons from QD1/QD2, and $\mathcal{V}^{\text{QD1}/3} = (92.7 \pm 1.6)\%$ for the photons from QD1/QD3. Here, the reflection and transmission coefficients of the beamsplitter in two-QD HOM experiments are $R = 0.498$ and $T = 0.502$; the classical visibility $(1 - \epsilon) = 0.996$. We re-calibrate the $g^{(2)}(0)$ values for the two-QD HOM setup, and use these values for correcting the two-QD HOM visibilities. We arrive at $g^{(2)}(0) = (2.05 \pm 0.27)\%$ for QD1, and $g^{(2)}(0) = (0.92 \pm 0.11)\%$ for QD2.

A.3.1 Theoretical Modelling of Two-QD HOM Visibility

If two single-photons enter a symmetric beamsplitter from the two input arms i and j , the probability that both input photons leave the beamsplitter through different output ports and become detected at times t_0 and $t_0 + \tau$ is given by¹⁷¹:

$$\mathcal{P}(t_0, \tau) = \frac{1}{4} |\zeta_i(t_0 + \tau) \zeta_j(t_0) - \zeta_j(t_0 + \tau) \zeta_i(t_0)|^2. \quad (\text{A.12})$$

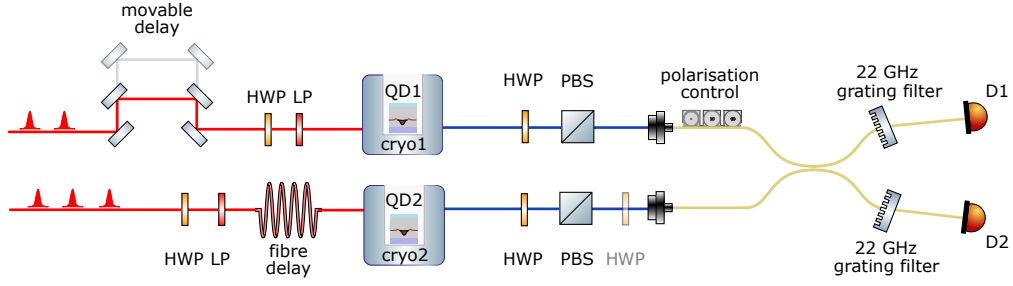


Fig. A.9. **Optical setup for Hong-Ou-Mandel experiments using two remote quantum dots.** The two GaAs QDs are located in two distant cryostats separated by 20-metre long fibres. Two separate excitation paths containing a movable delay on the QD1 side and an exchangeable fibre delay on the QD2 side are shown in red. The excitation pulses are synchronised. The excitation power can be separately adjusted (to the corresponding π -pulse power for each QD) using the combination of a HWP and a LP in each arm. Single photons from the two QDs (in blue) are sent to a fibre-based 50:50 beamsplitter. The HWP and the PBS on each of the collection paths set the polarisation of the QD photons to the co-polarised configuration. To distinguish the photons, we either insert another HWP to one of the collection paths (for the QD1-QD2 HOM measurement) or delay one photon temporally by half of the repetition period (by adding an additional fibre-delay in the excitation, e.g. for the QD1-QD3 HOM measurement). 22 GHz-bandwidth grating-based filters are inserted in both of the collection paths before the detectors.

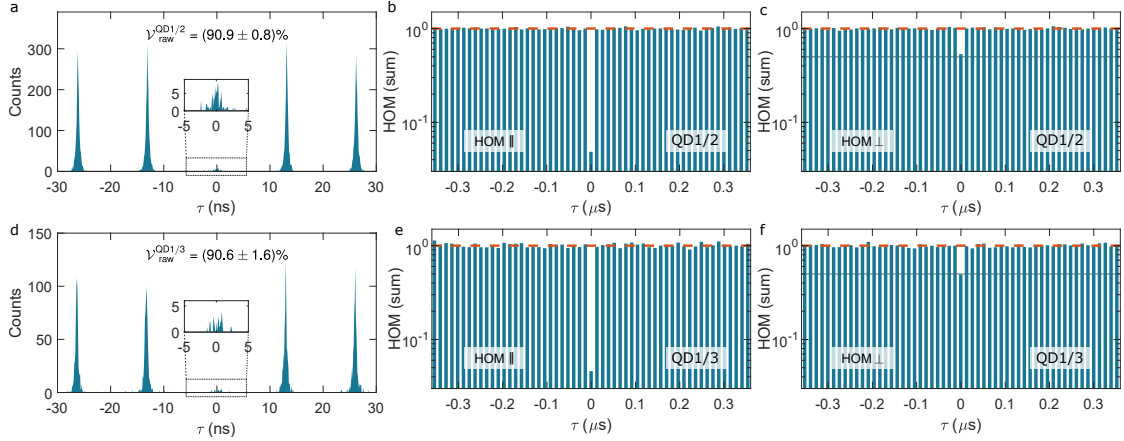


Fig. A.10. **Hong-Ou-Mandel interference between photons from remote quantum dots.** (a-c) Two-QD HOM experiments between photons from QD1 and QD2. The time-resolved two-QD HOM (in the co-polarised configuration) is plotted in (a), with the inset showing the zoom of the HOM central peak. Every peak in (a) is summed and normalised using a time bin of $T_{\text{bin}} = 13$ ns and shown as a bar chart in (b). In (c) we show a similar bar chart but for the cross-polarised case. The grey line beneath the bars represents the expected 50% level for distinguishable photons. Comparing the heights of the central bars ($\tau = 0$) in (b) and (c), we extract the raw HOM visibility for QD1 and QD2, $\mathcal{V}_{\text{raw}}^{\text{QD1/2}} = (90.8 \pm 0.8)\%$. (d-f) Two-QD HOM experiments using photons from QD1 and QD3. Similar to (a-c), $\mathcal{V}_{\text{raw}}^{\text{QD1/3}} = (90.6 \pm 1.6)\%$ for QD1 and QD3.

Here, $\zeta_{i,j}$ stands for the single-photon wave-functions from the two input arms. In our case, we describe the QD photons using a one-sided exponential decay,

$$\zeta_{i,j}(t) = \frac{1}{\sqrt{\tau_{i,j}}} H(t \pm \delta t/2) \cdot \exp\left\{-\frac{t \pm \delta t/2}{2\tau_{i,j}} - i[2\pi\nu_{i,j}t + \phi_{i,j}(t)]\right\}, \quad (\text{A.13})$$

with $\tau_{i,j}$ the radiative lifetime of the two QDs, $\nu_{i,j}$ the resonant frequency of the emitted photons. δt is the difference in the two photons' arrival time at the beamsplitter. If the two photons from remote QDs arrive simultaneously, $\delta t = 0$. The Heaviside-function $H(t)$ makes sure that no photon exists prior to the excitation process. The time-dependent phase term $\phi_{i,j}(t)$ is included to model the fast dephasing process.

Since the HOM measurements take usually several hours, the time-resolved HOM interference, $\mathcal{G}^{(2)}(\tau)$, can be calculated by integrating $\mathcal{P}(t_0, \tau)$ over a long time period^{164,171}:

$$\mathcal{G}^{(2)}(\tau) = \int_{-\infty}^{\infty} \langle\langle \mathcal{P}(t_0, \tau) \rangle\rangle dt_0, \quad (\text{A.14})$$

with $\langle\langle \dots \rangle\rangle$ denoting the statistical averaging.

$\mathcal{G}^{(2)}(\tau)$ is sensitive to both fast pure-dephasing and slow spectral fluctuations. Pure dephasing results in random fluctuations of the phase $\phi_{i,j}$. It is quantified by the dephasing rate $\Gamma_{i,j}^*$, leading to a modification in the overall dephasing rate $\gamma = \gamma_i + \gamma_j$ with $\gamma_{i,j} = 1/(2\tau_{i,j}) + \Gamma_{i,j}^*$ (here, i and j denote the two QDs). Spectral fluctuation can arise from noise (both spin noise and charge noise) in the semiconductor. It results in occasional frequency shifts in between the photon emission events, causing inhomogeneous broadening. The inhomogeneous broadening is often modelled with either a Gaussian^{67,172} or a Lorentzian^{70,98} distribution function. In the following, we discuss both the Gaussian- and Lorentzian-shaped spectral fluctuation and its influence on the two-photon interference.

- The noise results in a ‘‘Gaussian’’ spectral fluctuation:

In this case, the inhomogeneous broadening is described with a Gaussian probability distribution

$$p_G(\nu) = \frac{1}{\sqrt{2\pi}\sigma} \exp\left[-\frac{1}{2}\left(\frac{\nu - \nu_0}{\sigma}\right)^2\right], \quad (\text{A.15})$$

where $\sigma_{i,j}$ donates the standard deviation of the spectral fluctuation for each QD (subscripts are omitted in Eq. A. 15). $\sigma_{i,j}$ is related to the full-width-at-half-maximum (FWHM) of the Gaussian fluctuation $\sigma'_{i,j}$ via $\sigma'_{i,j} = 2\sqrt{2\ln 2} \sigma_{i,j}$. For the overall effects on the two photons, we introduce the parameter Σ , where $\Sigma^2 = \sigma_i^2 + \sigma_j^2$. Following Ref.

164, we obtain the expression for $\mathcal{G}^{(2)}(\tau)$:

$$\begin{aligned} \mathcal{G}^{(2)}(\tau) = & \frac{1}{4(\tau_i + \tau_j)} \cdot \left[H(\tau + \delta t) \cdot \exp\left(-\frac{\tau + \delta t}{\tau_i}\right) + H(-\tau - \delta t) \cdot \exp\left(\frac{\tau + \delta t}{\tau_j}\right) \right. \\ & + H(\tau - \delta t) \cdot \exp\left(-\frac{\tau - \delta t}{\tau_j}\right) + H(-\tau + \delta t) \cdot \exp\left(\frac{\tau - \delta t}{\tau_i}\right) \\ & \left. - 2 \cdot \exp\left(-\frac{\delta t}{2T_-} - \frac{|\delta t|}{2T_+} - \gamma|\tau| - 2\pi^2\Sigma^2\tau^2\right) \cdot \cos(2\pi\Delta\tau) \right]. \end{aligned} \quad (\text{A.16})$$

Here, $1/T_{\pm} = 1/t_i \pm 1/t_j$, δt represents the temporal delay of the two wave-packets and $\Delta = \nu_i - \nu_j$ their relative spectral detuning. $\mathcal{G}^{(2)}(\tau)$ describes the delay dependence of the central peak in the two-QD HOM experiment. The $\Gamma_{i,j}^*$ and Σ terms in Eq. A.16 represent the effects of fast dephasing and spectral fluctuations, respectively.

The overall probability of joint detection \mathcal{P} at the two output ports is calculated by integrating $\mathcal{G}^{(2)}$ over τ , $\mathcal{P} = \int_{-\infty}^{\infty} \mathcal{G}^{(2)}(\tau) d\tau$. The results can be expressed as¹⁶⁴:

$$\mathcal{P} = \frac{1}{2} \cdot \left(1 - \frac{\text{Re}[w(z)]}{\sqrt{2\pi}\Sigma(\tau_i + \tau_j)} \cdot e^{-|\delta t|/\tau_e} \right), \quad (\text{A.17})$$

where $z = (2\pi\Delta + i\gamma)/(2\pi\sqrt{2}\Sigma)$, and τ_e stands for the lifetime of the ‘‘early’’ photon. $\text{Re}[w(z)]$ is the real part of the Faddeeva function $w(z)$, which represents a Voigt profile¹⁷³. The Voigt dependence (versus Δ) is a result of the convolution between a Lorentzian function and a Gaussian function, which in turn comes from the Fourier transforms of the γ (exponential) and Σ (Gaussian) terms in Eq. A.16. \mathcal{P} is related to the two-QD HOM visibility via $\mathcal{V}_{\text{calc}} = 1 - 2\mathcal{P}$. Here, for the value of $\mathcal{V}_{\text{calc}}$, the effects of fast dephasing processes and spectral fluctuations are modelled, but experimental imperfections are not taken into account.

- The noise results in a ‘‘Lorentzian’’ spectral fluctuation:

$$p_L(\nu) = \frac{1}{\pi} \frac{\xi/2}{(\nu - \nu_0)^2 + (\xi/2)^2}, \quad (\text{A.18})$$

with $\xi_{i,j}$ being the FWHM of the Lorentzian inhomogeneous broadening in the frequency domain for each QD. We introduce the parameter Ξ accounting for the overall spectral fluctuations: $\Xi = \xi_i + \xi_j$. When assuming the spectral fluctuations of the two QDs are on the same level, $\xi_{i,j}$ becomes $\Delta\nu_S$ in the descriptions in Chapter 6, i.e. $\xi_i = \xi_j = \Delta\nu_S$.

The Lorentzian distribution function modifies the expression of $\mathcal{G}^{(2)}(\tau)$ to:

$$\begin{aligned} \mathcal{G}^{(2)}(\tau) = & \frac{1}{4(\tau_i + \tau_j)} \cdot \left[H(\tau + \delta t) \cdot \exp\left(-\frac{\tau + \delta t}{\tau_i}\right) + H(-\tau - \delta t) \cdot \exp\left(\frac{\tau + \delta t}{\tau_j}\right) \right. \\ & + H(\tau - \delta t) \cdot \exp\left(-\frac{\tau - \delta t}{\tau_j}\right) + H(-\tau + \delta t) \cdot \exp\left(\frac{\tau - \delta t}{\tau_i}\right) \\ & \left. - 2 \cdot \exp\left(-\frac{\delta t}{2T_-} - \frac{|\delta t|}{2T_+} - \gamma|\tau| - \Xi\pi|\tau|\right) \cdot \cos(2\pi\Delta\tau) \right]. \end{aligned} \quad (\text{A.19})$$

Here, instead of a Gaussian term we arrive at an exponential function $\exp(-\Xi\pi|\tau|)$ in the third line. This simplifies the expression for the joint detection probability \mathcal{P} to:

$$\mathcal{P} = \frac{1}{2} \left(1 - \frac{2(\gamma + \Xi\pi)}{(\gamma + \Xi\pi)^2 + 4\pi^2\Delta^2} \cdot \frac{e^{-|\delta t|/\tau_e}}{(\tau_i + \tau_j)} \right). \quad (\text{A.20})$$

Now, \mathcal{P} has a Lorentzian dependence on the detuning Δ . It is related to the two-QD HOM visibility via $\mathcal{V}_{\text{calc}} = 1 - 2\mathcal{P}$. For a perfect overlap of the two-photon wave-packets, i.e. $\tau_i = \tau_j = \tau_r$, $\delta t = 0$, $\Delta = 0$, the two-QD HOM visibility becomes:

$$\mathcal{V}_{\text{calc}} = \frac{1}{1 + (\Gamma_{\text{sum}}^* + \pi\Xi) \cdot \tau_r}, \quad (\text{A.21})$$

where $\Gamma_{\text{sum}}^* = \Gamma_i^* + \Gamma_j^*$. In Eq. A.21, Γ_{sum}^* and $\pi\Xi$ represent the half-width-at-half-maximum of the overall homogeneous and inhomogeneous broadening in angular frequency, respectively.

Neglecting the spectral fluctuation and assuming $\Gamma_j^* = \Gamma_i^*$, Eq. A.21 simplifies to the well-known expression for the one-QD HOM visibility $\mathcal{V} = T_c/2\tau$, with T_c defined as $1/\gamma_i$.

A.3.2 Limitations on Two-QD HOM Visibilities

In an idealised situation, i.e. when there is no noise in both QD-environments, the effects of spectral fluctuations ($\Sigma = 0$ or $\Xi = 0$) and pure dephasing ($\Gamma_{i,j}^* = 0$) vanish. In this ideal case, we calculate the two-QD HOM visibility using Eq. A.20 as a function of both the temporal delay δt and spectral detuning Δ of the two wave-packets. The results are shown in Fig. 6.2. In the calculations, the radiative decay rates of two QDs are taken from the exponential fits in Fig. A. 2. When the two remotely created photons suffer no delay nor detuning, i.e. $\Delta = 0$ and $\delta t = 0$, we expect the visibility to be $\mathcal{V} = 99.95\%$ despite a slight difference (4.3%) in the decay rates of the two QDs. The dependence of

the two-QD HOM visibility on the lifetime difference between the two QDs is depicted in Fig. A.11(a). The two-QD HOM visibility stays at a high level, e.g. close to 99% even when there is a 20% difference in the two-QD decay rates. Therefore, the difference in the decay rates is not the major limiting factor for the two-QD HOM experiment.

The measured visibility of the two-QD two-photon interference, $\mathcal{V} = (93.0 \pm 0.8)\%$, is around 7% less than the idealised expectation. We analyse these results in terms of noise, either in the semiconductor or in the apparatus.

Assuming the visibility of the one-QD HOM experiment is primarily limited by the fast dephasing processes, we use it to determine the fast dephasing rates in the QD systems. The visibilities of the 13 ns one-QD HOM measurements are $\mathcal{V}^{13\text{ns}} = (97.8 \pm 1.8)\%$ for QD1 and $\mathcal{V}^{13\text{ns}} = (98.2 \pm 1.3)\%$ for QD2, respectively, i.e. both $\sim 2\%$ lower than the idealised expectation. In the calculation of the one-QD HOM visibility, we employ Eq. A.21 assuming that the two photons have the same decay rate $\tau_i = \tau_j$ and perfect overlaps $\Delta = 0$, $\delta t = 0$. In the meantime, we ignore the influence of the slow spectral fluctuation process, $\Xi = 0$. We estimate how large the dephasing term needs to be in order to reach a visibility of 98%. From the calculations, this corresponds to $\Gamma^* = 34 \pm 25$ MHz for each QD (assuming $\Gamma_{\text{QD1}}^* \sim \Gamma_{\text{QD2}}^* = \Gamma^*$). The corresponding time is $1/\Gamma^* = 29 \pm 21$ ns: this is the time over which the exciton retains its phase in the absence of radiative decay. Here, the errors account for the uncertainty of the one-QD HOM visibility in the experiment. The dependence of the two-QD HOM visibility on the average dephasing rate Γ^* is shown in Fig. A.11(b). The small dephasing rates of 34 MHz in both QD systems reduce the two-QD HOM visibility also to 98%.

Experimental imperfections such as the imbalance of the beamsplitter and the non-unity classical interference visibility have been accounted for in the estimation of the true two-QD HOM visibility \mathcal{V} . The remaining experimental imperfections are usually negligible for one-QD HOM experiments but might still influence the two-QD HOM. For example, two independent voltage sources are employed for frequency tuning the two QDs. These two voltage sources need to be stable over the measurement time-scale (in our case, several hours) in order to maintain the two QDs in the same frequency. Although the mutual stability of the two voltage sources (LNHR DAC, Basel Precision Instruments) is high, we estimate a drift between the two voltage sources of $\sim \pm 20$ μV . Translating to frequency, this drift corresponds to an instability of 30 MHz (or $\sim 5\%$ of the QD linewidth), which leads to a reduction in HOM visibility of $\sim 0.3\%$ (estimated with the theoretical model). Besides, the dark counts from the SNSPDs also limit the measured visibility to a certain extent. We estimate a reduction of $\sim 0.5\%$ in the two-QD HOM visibility attributed to the dark counts. Nonetheless, experimental imperfections

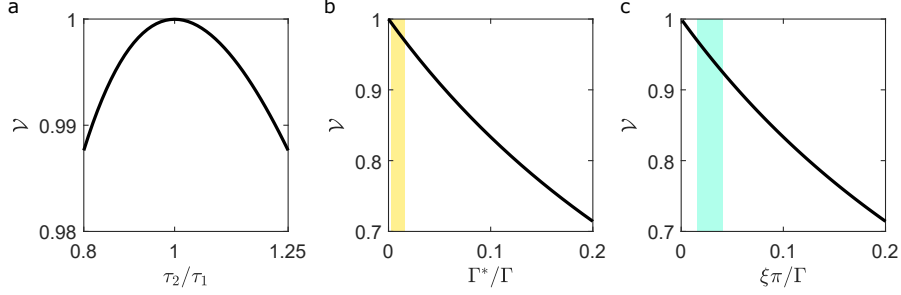


Fig. A.11. **Theoretical expectations of the two-QD Hong-Ou-Mandel visibility.** The two-QD HOM visibility is calculated using Eq. A.20. All parameters are in the ideal limit ($\tau_1 = \tau_2$, $\Gamma_1^* = 0$, $\Gamma_2^* = 0$, $\sigma_1 = 0$, $\sigma_2 = 0$, $\delta t = 0$, $\Delta = 0$) except (a) the two QDs have different lifetimes ($\tau_1 \neq \tau_2$); (b) the two QDs suffer from pure dephasing processes parameterised by Γ^* (normalised to the radiative decay rate Γ , $\Gamma^* = \Gamma_1^*/2 + \Gamma_2^*/2$); (c) environmental noise results in a Lorentzian-shaped spectral fluctuation (parameterised by the half-width-at-half-maximum of the inhomogeneous broadening $\xi\pi$ in angular frequency, and normalised by Γ , $\xi = \xi_1/2 + \xi_2/2$). The lifetime difference of the QDs plays only a minor role in the HOM visibility compared to the dephasing and spectral fluctuation processes. The coloured regions in (b) and (c) represent the estimated effects of the fast dephasing and slow spectral fluctuation in our QDs, respectively. The width of the coloured regions represents the error margin of the estimated Γ^* and ξ .

are thought to have a minor influence on the measurements of \mathcal{V} .

The remaining difference between the experimental two-QD HOM visibility and the ideal value is attributed to noise in the semiconductor. The noise results in spectral fluctuations. The noise spectrum of InGaAs QDs^{70,98} has a Lorentzian spectral distribution, and we assume the same for GaAs QDs. With Eq. A.20, we calculate the two-QD HOM visibility as a function of the spectral fluctuation parameter Ξ , where Ξ stands for the FWHM of the overall inhomogeneous broadening of both QDs in frequency, $\Xi = \xi_1 + \xi_2$. In the ideal case ($\Gamma^* = 0$, $\tau_1 = \tau_2$, $\delta t = 0$, $\Delta = 0$), the effect of spectral fluctuations is shown in Fig. A.11(c). In practice, the QDs also suffer from the impact of fast dephasing. Adding the dephasing rate $\Gamma^* = 34 \pm 25$ MHz, we estimate the spectral fluctuations in our systems to be $\Xi = 2 \times (34 \pm 15)$ MHz – this level of spectral fluctuation brings the calculated two-QD HOM visibility to the experimental result. In other words, the slow fluctuation of each QD results in on average a Lorentzian broadening of $\Delta\nu_S = 34 \pm 15$ MHz. This corresponds to a dephasing time $T_2^* = 1/(\pi\Delta\nu_S) = 9.1 \pm 3.9$ ns.

The HOM results on the dephasing should be compatible with the measured spectral linewidths. For QD1 and QD2, the average spectral linewidth broadening is measured to be 55 ± 26 MHz; for QD1 and QD3, this value is 64 ± 31 MHz (from Lorentzian fits, see Fig. A.2). Subtracting the contribution of homogeneous broadening $\Delta\nu_H = \Gamma^*/\pi =$

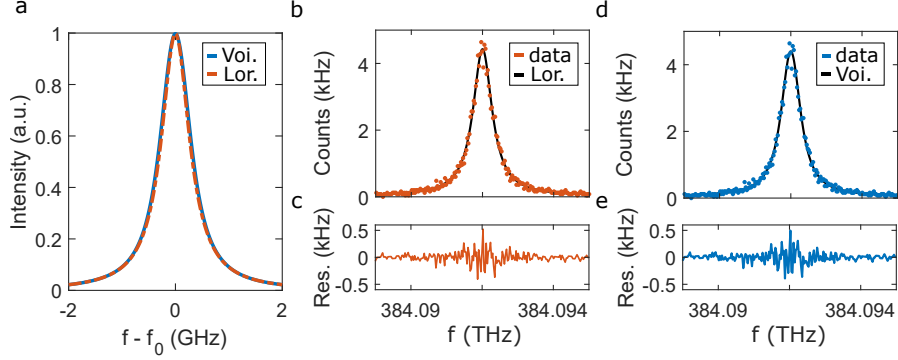


Fig. A.12. **A comparison of Voigt and Lorentzian lineshapes.** (a) Calculation of Voigt and Lorentzian lineshapes based on the experimental parameters. Red curve: Lorentzian profile calculated with a total broadening of $\Delta\nu_H + \Delta\nu_S = 45$ MHz plus the natural linewidth of $[1/(2\pi\tau_1) = 597$ MHz] (that is, in total, a FWHM of 642 MHz). Cyan curve: Voigt profile calculated with a Gaussian contribution (standard deviation $\sigma_{\text{avg}} = 95$ MHz) and a Lorentzian contribution [with FWHM of $\Delta\nu_H + 1/(2\pi\tau_1) = 608$ MHz]. The difference between the two lineshapes is hardly visible. (b,c) The Lorentzian fit to the QD1 spectrum and the residuals. The total Lorentzian broadening above the lifetime-limit is 50 ± 17 MHz. (d,e) The Voigt fit to the QD1 spectrum and the residuals. Here, we fixed the Lorentzian contribution to 608 MHz (FWHM). This yields a Gaussian contribution of $\sigma_{\text{fit}} = 70 \pm 43$ MHz. The Lorentzian function fits the data slightly better than the Voigt function.

11 ± 8 MHz, we extract the inhomogeneous broadening $\Delta\nu_S^{\text{exp}} = 43 \pm 27$ MHz for QD1 and QD2 pair, and $\Delta\nu_S^{\text{exp}} = 53 \pm 32$ MHz for QD1 and QD3 pair. These results are compatible with the two-QD HOM analysis.

We also present the analysis with a spectral fluctuation described by a Gaussian probability distribution. In this case, we rely on Eq. A.17. Together with the dephasing rate $\Gamma^* = 34 \pm 25$ MHz, we estimate a spectral fluctuation of $\Sigma = \sqrt{2} \times 95 \pm 27$ MHz – on average, the standard derivation of the spectral fluctuation is $\sigma = 95 \pm 27$ MHz for each QD. The Gaussian contribution turns the QD spectrum into a Voigt profile. However, as σ is rather small compared to $1/(2\pi\tau_r)$ (the minimal Lorentzian width set by the radiative lifetime), the Voigt lineshape resembles the Lorentzian one [Fig. A.12(a)]. A comparison between the Lorentzian and Voigt fits to the QD1 spectrum are shown in Fig. A.12(b-e). The Gaussian width parameter ($\sigma_{\text{fit}} = 70 \pm 43$ MHz) extracted from the Voigt fit is compatible with the σ determined from the two-QD HOM visibility. However, the Lorentzian function fits the data slightly better than the Gaussian function.

A.3.3 Effect of Temporal Post-Selection

Equation A.19 allows the dependence of the two-QD HOM visibility on the width of time-window T_{bin} to be simulated. In the data analysis process, the HOM visibilities

are calculated in a rigorous way: for every HOM peak, the coincidence events in a whole pulse repetition period are considered, i.e. $T_{\text{bin}} = T_{\text{period}}$. Narrowing the time-window T_{bin} [see Fig. A.13(a)] leads to temporal post-selections, as a consequence resulting in an increase in the apparent HOM visibility. In Fig. A.13(b) we show the theoretical calculation of the HOM values on varying T_{bin} . Here we take into account the exciton dephasing and the noise in the semiconductor via $\Gamma^* = 34$ MHz and $\Xi = 2 \times 34$ MHz. As T_{bin} approaches T_{period} we find $\mathcal{V}_{\text{calc}} = 93\%$, equivalent to the results from Eq. A.20 (a consequence of $T_{\text{bin}} \gg \tau_{1,2}$). As T_{bin} decreases, we observe first almost no change in $\mathcal{V}_{\text{calc}}$ until $T_{\text{bin}} \sim 20 \tau_r$. Reducing T_{bin} further results in a sharp increase in the calculated visibility. For example, at $T_{\text{bin}} = 2 \tau_r$ we find $\mathcal{V}_{\text{calc}} = 98\%$. In this case, more than 50% of the coincidence counts are rejected by post-selection.

We also perform the analysis on the experimental results of the two-QD HOM measurement as a function of T_{bin} . An example is shown in Fig. A.13(c) for the two-QD HOM using QD1 and QD2. Similar to the theoretical prediction, we see a decrease in \mathcal{V}_{exp} as T_{bin} increases. The dependence of the two-QD HOM visibility on the width of time window T_{bin} matches the theoretical result rather well.

A.3.4 Effect of Purcell Enhancement

Thanks to the low noise behaviour in our GaAs QDs system, the visibility of one-QD and two-QD HOMs are close to perfect even without any Purcell enhancement.

Eq. A.21 allows an estimation of the effect of Purcell enhancement on the one-QD and two-QD HOM visibility to be made. The Purcell effect reduces the radiative lifetime of the QD, τ_r , by the Purcell factor F_P . This leads to an additional increase in one-QD and two-QD HOM visibilities. For single-QD photons, with only moderate Purcell enhancement, e.g. $F_P = 5$, the lifetime is shortened to $\tau_r \sim 50$ ps and the indistinguishability can be boosted above 99.5%. For the photons from remote QDs, a Purcell enhancement of $F_P = 10$ in each system is enough to increase the two-QD HOM visibility to above 99% provided that the present noise-level is preserved (assuming a Lorentzian noise spectrum; for a Gaussian noise spectrum the two-QD HOM visibility exceeds 99% for $F_P \sim 6$). Such a moderate Purcell enhancement has been realised in various nano-engineered platforms, such as integrated photonic-crystal cavities⁹ and open microcavities^{7,11,174}.

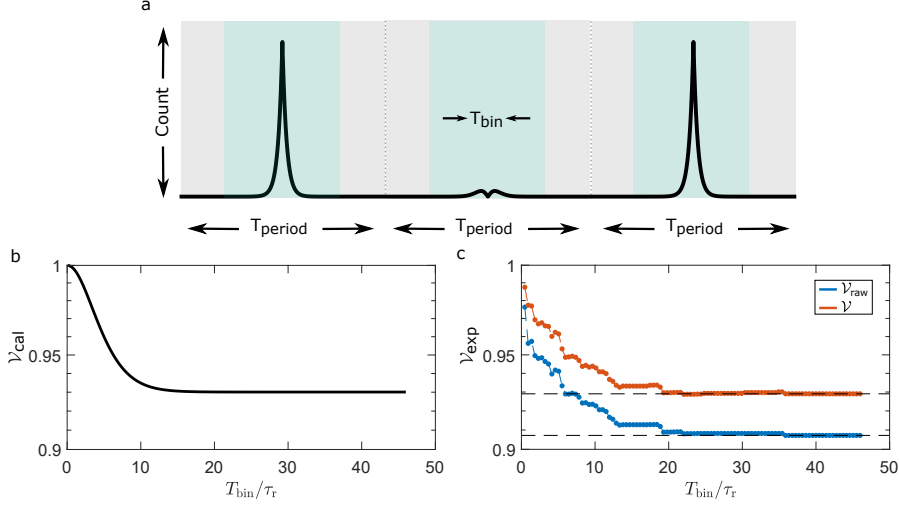


Fig. A.13. **Hong-Ou-Mandel visibility as a function of temporal binning size.** (a) A sketch showing the time-binning window in the HOM data analysis. The pulsed excitation laser has a repetition period of $T_{\text{period}} = 13$ ns. Every T_{period} contains one HOM peak, and the time-binning window is centred around each HOM peak. In (b, c) we reduce the width of this time-window T_{bin} from T_{period} to close to zero, and calculate/extract the predicted/measured HOM visibility for the remote-QD two-photon interference. In (b), we apply the time-binning window to a predicted delay dependence two-photon interference $\mathcal{G}^{(2)}(\tau)$. This $\mathcal{G}^{(2)}(\tau)$ is calculated using Eq. A.19, with parameters $\Gamma_1 = 3.75$ GHz, $\Gamma_2 = 3.91$ GHz, $\Gamma^* = 34$ MHz, $\Xi = 2 \times 34$ MHz, $\delta t = 0$ and $\Delta = 0$. The calculated two-QD HOM visibility drops to 93% at $T_{\text{bin}} = 20 \tau_r$ and levels off. In (c), the measured two-QD HOM visibility (QD1 and QD2, $\delta t = 0$, $\Delta = 0$) is shown as a function of the normalised time bin. The visibility is artificially increased to $\mathcal{V} \sim 98\%$ when the bin width is comparable to the QD lifetime. At large time-binning windows ($T_{\text{bin}} = T_{\text{period}}$), we determine the real two-QD HOM visibility, $\mathcal{V} = 93\%$: in this limit, no temporal post-processing is included.

A.4 Optical Controlled-Not Circuit with Remote-Quantum-Dot Photons

We performed a proof-of-principle demonstration of an optical controlled-not (CNOT) circuit utilising the ultra-high photon coherence between two remote QDs. The CNOT gate is equivalent to a controlled phase gate up to single-qubit operations. In our experiment, the CNOT functionality is realised based on two-photon interference in linear optics^{18,165,175,176}. The optical setup consists of a combination of three partially polarising beamsplitters (PPBSs) working as a controlled phase gate and two half-wave plates (HWPs) as two Hadamard gates [Fig. A.14(a)].

The controlled phase (CZ) gate performs a π -phase shift conditioned by the two-qubit

state $|11\rangle$, i.e.

$$a|00\rangle + b|01\rangle + c|10\rangle + d|11\rangle \xrightarrow{\text{CZ}} a|00\rangle + b|01\rangle + c|10\rangle - d|11\rangle.$$

In the experiment, we define $|H\rangle = |0\rangle$, $|V\rangle = |1\rangle$. The π -phase shift is implemented via quantum interference at the central PPBS (PPBS₀). The central PPBS exhibits perfect transmission for horizontal polarisation and 1/3 transmission for vertical polarisation. For the $|VV\rangle$ inputs from the two ports i and j , if the two photons are indistinguishable, the central PPBS results in a total amplitude of $-1/3$ for the $|VV\rangle$:

$$t_V^i \cdot t_V^j + (ir_V^i \cdot ir_V^j) = \sqrt{\frac{1}{3}}\sqrt{\frac{1}{3}} - \sqrt{\frac{2}{3}}\sqrt{\frac{2}{3}} = -\frac{1}{3}. \quad (\text{A.22})$$

Here, t and r are the amplitude transmission and reflection coefficients of the central PPBS, respectively. For the other three input states, i.e. $|HH\rangle$, $|HV\rangle$ and $|VH\rangle$, the central PPBS does not introduce any quantum interference. The amplitudes in the coincidence measurements are attenuated to 1/3 by the PPBSs on the two output arms [see Fig. A.14(a); PPBS₁ and PPBS₂ each reduce the transmission of H -polarised light to 1/3]. For example, the $|HH\rangle$ output reads $(t_H^i t_H^j) \cdot (t_H^1 t_H^2) = \frac{1}{3}$, where $t_H^{1,2} = \sqrt{\frac{1}{3}}$ is the transmission amplitude of PPBS₁ and PPBS₂. Therefore, a CZ operation can be realised with an amplitude of 1/3 using the arrangement of three PPBSs in Fig. A.14(a), i.e. a success probability of 1/9.

A.4.1 Alignment of Controlled-Not Setup

In reality, the PPBSs (Asahi Spectra) do not have perfect performance, e.g. the transmission (reflection) is not precisely 1/3 (2/3). The performance of PPBSs depends on the incident angle. To achieve optimal performance, we align the CNOT setup with the aim to fulfil the following three criteria^{165,177}:

1. the reflectivity of PPBS₀ for H -polarisation should be zero,

$$r_H^i = 0 = r_H^j; \quad (\text{A.23})$$

2. the product of the reflection amplitudes of PPBS₀ should be twice its transmission amplitudes,

$$\frac{r_V^i \cdot r_V^j}{t_V^i \cdot t_V^j} = 2; \quad (\text{A.24})$$

3. the attenuation of PPBS₁ and PPBS₂ should balance the amplitudes of H - and V -polarised light,

$$t_H^i \cdot t_H^1 = t_V^i \cdot t_V^1, \quad (\text{A.25})$$

$$t_H^j \cdot t_H^2 = t_V^j \cdot t_V^2. \quad (\text{A.26})$$

In the experiment, the three conditions are mostly met:

1. $r_H^i = 0.0008$, $r_H^j = 0.0031$;
2. $t_V^i = \sqrt{0.3306}$, $t_V^j = \sqrt{0.3355}$, $r_V^i = \sqrt{0.6389}$, $r_V^j = \sqrt{0.6645}$, such that

$$\frac{r_V^i \cdot r_V^j}{t_V^i \cdot t_V^j} = 1.96;$$

3. $t_H^1 = \sqrt{0.3237}$, $t_V^1 = \sqrt{0.9548}$, $t_H^2 = \sqrt{0.3236}$, $t_V^2 = \sqrt{0.9904}$, such that,

$$t_H^i \cdot t_H^1 = 1.0039 \cdot t_V^i \cdot t_V^1,$$

$$t_H^j \cdot t_H^2 = 0.9839 \cdot t_V^j \cdot t_V^2.$$

A.4.2 Operations of Controlled-Not Gate

We test the gate performance in both the computation basis $|H\rangle/|V\rangle$ and the $|+\rangle/|-\rangle$ basis, where $|\pm\rangle = 1/\sqrt{2}(|H\rangle \pm |V\rangle)$. The input states are prepared using two half-wave plates [see Fig. 6.3(a)]. For every input state, the output states are measured simultaneously with four coincidence measurements. The coincidence events of each central peak in the four measurements are summed using $T_{\text{bin}} = 13$ ns. The sum represents the count rates for each input-output relation. The coincidence count rates are converted to probabilities by normalising them with the overall coincidence counts of all four coincidence measurements. The probabilities are plotted in Fig. 6.3(b, c) and the numbers are shown in Fig. A.14(b, c) for the two measurement bases.

We take the measurements in the $|H\rangle/|V\rangle$ basis as an example and analyse the limiting factors for each input state. For $|HH\rangle$ input, the signal in the $|HV\rangle$ and $|VV\rangle$ outputs arises probably because of imperfections in the PPBSs as well as the imprecision of the half-wave plate rotation; for the $|VH\rangle$ output, the non-zero values of $g^{(2)}(0)$ play a major role, together with the PPBS and HWP imperfections. The undesired outputs for the $|HV\rangle$ input state have similar origins. For $|VH\rangle$ and $|VV\rangle$ inputs, quantum interference between remote-QD photons plays a major role in the flip of the target

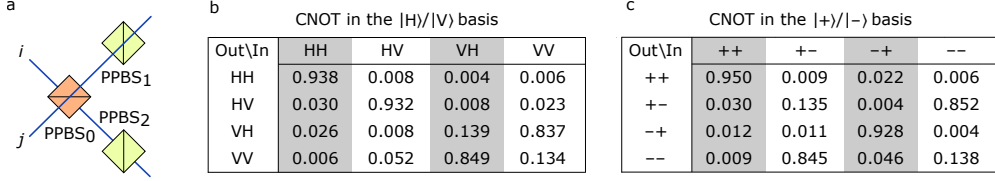


Fig. A.14. **A Sketch of the controlled-phase gate and truth tables for the controlled-not gate measured in two complementary bases.** (a) The central partially polarising beamsplitter (PPBS₀) transmits H -polarised light while reflects partially V -polarised light. The other two PPBSs are flipped by 90° so that all V -polarised components are transmitted and H -polarised components are attenuated by $2/3$. (b, c) Truth tables of the CNOT process in the $|H\rangle/|V\rangle$, and $|+\rangle/|-\rangle$ bases. The same results are visualised in Fig. 6.3(b, c).

qubit. Take the $|VV\rangle$ input as an example: measuring the $|VV\rangle$ output probability is in principle the same as a two-QD HOM experiment in which the count-rates of both QDs are reduced to $1/3$. The unflipped $|VV\rangle$ output arises mostly from the $\sim 7\%$ imperfection in the two-QD HOM visibility [$\mathcal{V}_{\text{rm}}^{\text{QD}1/2} = 93.0\%$]. The finite $|HH\rangle$ and $|HV\rangle$ outputs arise again due to the setup imperfections.

The fidelity of the CNOT gate, defined as the averaged probability of obtaining the expected output states, is calculated as^{178,179},

$$\mathcal{F}_{ZZ} = \frac{1}{4} \left[P(HH|HH) + P(HV|HV) + P(VH|VV) + P(VV|VH) \right],$$

$$\mathcal{F}_{XX} = \frac{1}{4} \left[P(++|++) + P(+−|−−) + P(−+|−+) + P(−−|+−) \right].$$

Here $P(I_1 I_2 | O_1 O_2)$ represents the input-output probabilities of the CNOT operation. Substituting the probabilities from experimental results [Fig. A.14(b, c)] into the equations, we obtain $\mathcal{F}_{ZZ} = (88.90 \pm 5.34)\%$, and $\mathcal{F}_{XX} = (89.34 \pm 5.29)\%$.

A.5 Density Matrix Reconstruction of Bell State

The CNOT gate produces the Bell state $|\Psi^-\rangle$ when the input state is prepared as $|-\rangle_c |V\rangle_t$. The Bell state is analysed by quantum state tomography consisting of 9×4 coincidence measurements in a combination of $|H\rangle, |V\rangle, |+\rangle, |-\rangle, |R\rangle, |L\rangle$, where $|L\rangle = (|H\rangle + i|V\rangle)/\sqrt{2}$ and $|R\rangle = (|H\rangle - i|V\rangle)/\sqrt{2}$. As before, the coincidence count-rates of each measurement are calculated as the area under the central peak with $T_{\text{bin}} = 13$ ns. The 36 projection bases $|\psi_\nu\rangle$ as well as their corresponding probabilities s_ν are depicted in Fig. A.15. The density matrix $\hat{\rho}$ is reconstructed based on the results of the 36 measurements using maximum likelihood estimation as detailed in Ref. 166,180.

From the reconstructed $\hat{\rho}$ we calculate the entanglement fidelity, which measures the overlaps between the experimentally generated state and the ideal state (density matrix $\hat{\rho}_{\text{ideal}}$),

$$\mathcal{F}(\hat{\rho}_{\text{ideal}}, \hat{\rho}) = \left(\text{Tr} \left[\sqrt{\sqrt{\hat{\rho}_{\text{ideal}}} \hat{\rho} \sqrt{\hat{\rho}_{\text{ideal}}}} \right] \right)^2.$$

Furthermore, the concurrence, as well as the linear entropy of the entanglement, are determined. The concurrence is an entanglement monotone characterising the coherence properties of a quantum state. It is defined as:

$$C(\hat{\rho}) = \max(0, \lambda_1 - \lambda_2 - \lambda_3 - \lambda_4), \quad (\text{A.27})$$

where $\lambda_1 \dots \lambda_4$ represent the eigenvalues of the product of the state ρ and its spin-flipped counterpart $\tilde{\rho}$. Among them, λ_1 is the maximal eigenvalue. The spin-flip operation on the state ρ reads: $\tilde{\rho} = (\sigma_y \otimes \sigma_y) \rho^* (\sigma_y \otimes \sigma_y)$.

The linear entropy S_L quantifies the degree of mixture in quantum states. S_L ranges from zero for pure states to one for completely mixed states.

$$S_L(\hat{\rho}) = \frac{4}{3} [1 - \text{Tr}(\hat{\rho}^2)]. \quad (\text{A.28})$$

Substituting the reconstructed density matrix $\hat{\rho}$ into Eq. (27-29), we obtain $\mathcal{F} = (85.02 \pm 0.97)\%$, $C = (74.67 \pm 1.93)\%$ and $S_L = (34.04 \pm 1.94)\%$, indicating a high level of entanglement and purity. The error margins are deduced from Monte-Carlo simulations assuming errors in the coincidence counts stemming from Poissonian statistics¹⁸⁰. The entanglement of two streams of coherent single-photons constitutes a first step in utilising multiple QDs for complex quantum algorithms^{151,181}. The deviation from the ideal $|\Psi^-\rangle$ state likely originates from both the wave-plates and the remaining imperfections in the remote-QD multi-photon source. The CNOT process and the created photon-photon entanglement should benefit from a boost of the two-QD HOM visibility when Purcell enhancement is introduced to the remote GaAs QDs system. Employing on-chip integrated photonic circuits can further reduce the setup imperfections.

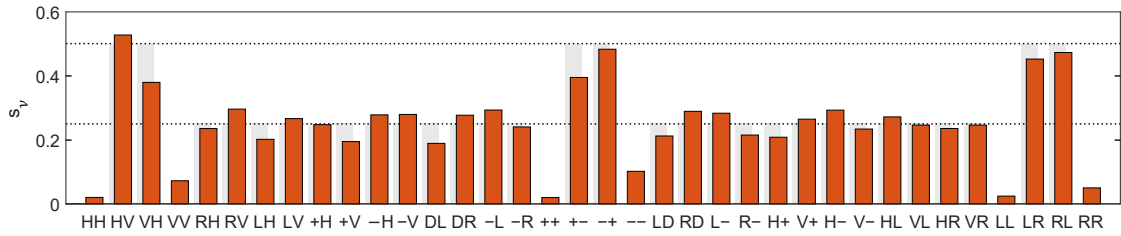


Fig. A.15. **Projection outcomes of $|\Psi^-\rangle$ in quantum state tomography.** The probabilities S_ν are calculated by adding up the coincidence counts in the central peak and normalising the sum to the overall counts in each set of four coincidence measurements. The two dashed lines indicate the $S_\nu = 0.25$ and $S_\nu = 0.5$ levels. The light grey background represents the projection probabilities for the ideal $|\Psi^-\rangle$ state.

Acknowledgments

First and foremost, I am grateful to my advisor Prof. Richard Warburton. Thank you Richard for offering me this great opportunity to perform research independently in a world-class quantum optics lab. Richard has been always an enthusiastic supporter of our research work. He inspired, encouraged and motivated me throughout my PhD career in Basel. I would like to thank my second advisor Prof. Philipp Treutlein. Philipp has initialised the project of storing quantum dot photons in a rubidium memory together with Richard. He motivated us to improve the quantum dot's quality. The discussions we had were always very fruitful. I would also like to thank Prof. Chaoyang Lu from the University of Science and Technology of China for accepting to be my PhD examiner. Chaoyang is a talented researcher in China. Thank you, Chaoyang, for spending time reading my thesis and for your valuable feedback.

I would like to thank all the colleagues who worked with me on the GaAs quantum dots project. First, many thanks to my predecessor, Dr. Jan-Philipp Jahn, for handing over his knowledge/expertise on the GaAs quantum dots. I would like to thank Dr. Matthias C. Löbl. Matthias and I had discussions frequently at my early PhD stage. He was always knowledgeable and offered his help during the preparation of the low-noise quantum dot paper. I would like to express my gratitude to Dr. Alisa Javadi. Alisa was my co-supervisor back in Copenhagen where I did my Master study. We met again in Basel when he became a post-doc here. I always learn a lot when discussing with Alisa, and he is always offering to help. I truly appreciate the time when we worked together. Furthermore, I would like to my lab-mates Giang Nam Nguyen and Clemens Spinnler who spent countless hours with me in the lab. We built optics, we discussed and figured out various problems, we pushed the project forward together – it is my pleasure to work with you as a team!

My sincere thanks go to the entire Nano-Photonics group. I appreciate the friendly and supporting work-space in the group and the beers/coffees/foods we enjoyed together. For this, besides the people mentioned above, I am grateful to Natasha Tomm,

Nadia Antoniadis, Mark Hogg, Willy Stehl, Lukas Sponfeldner, Nadine Leisgang, Viktoria Yurgens, Yannik Fontana, Andrea Corazza, Sigurd Flôgan, Marcel Erbe, Simon Geyer, Jonas Roch, Ben Patrick, Immo Söllner, Tomek Jakubczyk, Daniel Riedel and Daniel Najer.

I cannot appreciate enough our collaborators in Bochum. Many thanks to Dr. Arne Ludwig, Prof. Andreas D. Wieck, Dr. Julian Ritzmann and Hans-Georg Babin. I appreciate not only the excellent semiconductor quantum dot wafer that was fabricated in Bochum, but also their knowledge and enthusiasm of semiconductor physics. I am very grateful to Arne for allowing me to visit Bochum twice. I have learned a lot during my time in Bochum; the visit was the start of the low-noise GaAs project. Furthermore, my thanks go to our collaborators in Copenhagen, including Prof. Peter Lodahl, Prof. Leonardo Midolo, Dr. Ravitej Uppu, and many more. We discussed physics regularly in our bi-weekly meetings, and I am very grateful for all your help and the discussions.

I would like to thank the rubidium memory team in Prof. Treutlein's Quantum Optics Lab. Thank you, Gianni Buser and Roberto Mottola, for introducing the rubidium quantum memory experiment to me. The memory side has been improved steadily throughout my PhD period. I hope our combined experiment will be successful. I would also like to mention the Innovative Training Network "4photon" under Marie Curie Actions which funded my PhD study. Especially, I would like to thank all the early-stage researchers and professors within the network for our annual meetings and the training/support in the network.

Finally, a warm thanks to all my family and friends. To my mom, Runlian Wang, sincerely thank you for being there for me even from a long distance, for always supporting me and for believing in me at every moment of my life. I am grateful to my girlfriend Tianmeng Zhou, my father, my grandparents, my uncles and aunts. Thank you all for your continuous support. Without your support, I could not have accomplished any of the above on my own.

Bibliography

- [1] Kagan, C. R., Lifshitz, E., Sargent, E. H. & Talapin, D. V. Building devices from colloidal quantum dots. *Science* **353** (2016).
- [2] Van der Wiel, W. G. *et al.* Electron transport through double quantum dots. *Rev. Mod. Phys.* **75**, 1 (2002).
- [3] Warburton, R. J. Single spins in self-assembled quantum dots. *Nat. Mater.* **12**, 483 (2013).
- [4] Nguyen, G. *et al.* Influence of molecular beam effusion cell quality on optical and electrical properties of quantum dots and quantum wells. *J. Cryst. Growth* **550**, 125884 (2020).
- [5] Eaglesham, D. & Cerullo, M. Dislocation-free Stranski-Krastanow growth of Ge on Si (100). *Phys. Rev. Lett.* **64**, 1943 (1990).
- [6] Leonard, D., Krishnamurthy, M., Reaves, C., DenBaars, S. P. & Petroff, P. M. Direct formation of quantum-sized dots from uniform coherent islands of InGaAs on GaAs surfaces. *Appl. Phys. Lett.* **63**, 3203–3205 (1993).
- [7] Senellart, P., Solomon, G. & White, A. High-performance semiconductor quantum-dot single-photon sources. *Nat. Nanotechnol.* **12**, 1026 (2017).
- [8] Thyrrestrup, H. *et al.* Quantum optics with near-lifetime-limited quantum-dot transitions in a nanophotonic waveguide. *Nano Lett.* **18**, 1801–1806 (2018).
- [9] Liu, F. *et al.* High Purcell factor generation of indistinguishable on-chip single photons. *Nat. Nanotechnol.* **13**, 835–840 (2018).
- [10] Wang, H. *et al.* Towards optimal single-photon sources from polarized microcavities. *Nat. Photonics* **13**, 770–775 (2019).
- [11] Tomm, N. *et al.* A bright and fast source of coherent single photons. *Nat. Nanotechnol.* **16**, 399–403 (2021).

- [12] Koguchi, N., Takahashi, S. & Chikyow, T. New MBE growth method for InSb quantum well boxes. *J. Cryst. Growth* **111**, 688–692 (1991).
- [13] Gurioli, M., Wang, Z., Rastelli, A., Kuroda, T. & Sanguinetti, S. Droplet epitaxy of semiconductor nanostructures for quantum photonic devices. *Nat. Mater.* **18**, 799–810 (2019).
- [14] Heyn, C. *et al.* Highly uniform and strain-free GaAs quantum dots fabricated by filling of self-assembled nanoholes. *Appl. Phys. Lett.* **94**, 183113 (2009).
- [15] Huo, Y. H., Rastelli, A. & Schmidt, O. G. Ultra-small excitonic fine structure splitting in highly symmetric quantum dots on GaAs (001) substrate. *Appl. Phys. Lett.* **102**, 152105 (2013).
- [16] Basso Basset, F. *et al.* High-yield fabrication of entangled photon emitters for hybrid quantum networking using high-temperature droplet epitaxy. *Nano Lett.* **18**, 505–512 (2018).
- [17] Löbl, M. C. *et al.* Correlations between optical properties and voronoi-cell area of quantum dots. *Phys. Rev. B* **100**, 155402 (2019).
- [18] He, Y.-M. *et al.* On-demand semiconductor single-photon source with near-unity indistinguishability. *Nat. Nanotechnol.* **8**, 213–217 (2013).
- [19] Wang, H. *et al.* Boson sampling with 20 input photons and a 60-mode interferometer in a 10^{14} -dimensional Hilbert space. *Phys. Rev. Lett.* **123**, 250503 (2019).
- [20] Loredó, J. C. *et al.* Boson sampling with single-photon Fock states from a bright solid-state source. *Phys. Rev. Lett.* **118**, 130503 (2017).
- [21] Heindel, T. *et al.* Quantum key distribution using quantum dot single-photon emitting diodes in the red and near infrared spectral range. *New J. Phys.* **14**, 083001 (2012).
- [22] Yin, H.-L. *et al.* Measurement-device-independent quantum key distribution over a 404 km optical fiber. *Phys. Rev. Lett.* **117**, 190501 (2016).
- [23] Bodey, J. H. *et al.* Optical spin locking of a solid-state qubit. *npj Quantum Inf.* **5** (2019).
- [24] Stockill, R. *et al.* Quantum dot spin coherence governed by a strained nuclear environment. *Nat. Commun.* **7**, 12745 (2016).

- [25] Éthier-Majcher, G. *et al.* Improving a solid-state qubit through an engineered mesoscopic environment. *Phys. Rev. Lett.* **119**, 130503 (2017).
- [26] Tiurev, K. *et al.* High-fidelity multiphoton-entangled cluster state with solid-state quantum emitters in photonic nanostructures. *Phys. Rev. A* **105**, L030601 (2022).
- [27] Stockill, R. *et al.* Phase-tuned entangled state generation between distant spin qubits. *Phys. Rev. Lett.* **119**, 010503 (2017).
- [28] Javadi, A. *et al.* Single-photon non-linear optics with a quantum dot in a waveguide. *Nat. Commun.* **6**, 1–5 (2015).
- [29] Lodahl, P. *et al.* Chiral quantum optics. *Nature* **541**, 473–480 (2017).
- [30] Carter, S. G. *et al.* Spin-mechanical coupling of an InAs quantum dot embedded in a mechanical resonator. *Phys. Rev. Lett.* **121**, 246801 (2018).
- [31] Munsch, M. *et al.* Resonant driving of a single photon emitter embedded in a mechanical oscillator. *Nat. Commun.* **8**, 76 (2017).
- [32] Keil, R. *et al.* Solid-state ensemble of highly entangled photon sources at rubidium atomic transitions. *Nat. Commun.* **8**, 15501 (2017).
- [33] Huber, D. *et al.* Strain-tunable GaAs quantum dot: A nearly dephasing-free source of entangled photon pairs on demand. *Phys. Rev. Lett.* **121**, 033902 (2018).
- [34] Plumhof, J. D., Trotta, R., Rastelli, A. & Schmidt, O. G. Experimental methods of post-growth tuning of the excitonic fine structure splitting in semiconductor quantum dots. *Nanoscale Res. Lett.* **7**, 1–11 (2012).
- [35] Rakher, M. T., Warburton, R. J. & Treutlein, P. Prospects for storage and retrieval of a quantum-dot single photon in an ultracold ^{87}Rb ensemble. *Phys. Rev. A* **88**, 053834 (2013).
- [36] Zhai, L. *et al.* Quantum interference of identical photons from remote GaAs quantum dots. *Nat. Nanotechnol.* **17**, 829–833 (2022).
- [37] Zhai, L. *et al.* Low-noise GaAs quantum dots for quantum photonics. *Nat. Commun.* **11**, 4745 (2020).
- [38] Löbl, M. C. *et al.* Radiative Auger process in the single-photon limit. *Nat. Nanotechnol.* **15**, 558–562 (2020).

- [39] Spinnler, C. *et al.* Optically driving the radiative auger transition. *Nat. Commun.* **12**, 6575 (2021).
- [40] Urbaszek, B. *et al.* Nuclear spin physics in quantum dots: An optical investigation. *Rev. Mod. Phys.* **85**, 79–133 (2013).
- [41] Högele, A. *et al.* Dynamic nuclear spin polarization in the resonant laser excitation of an InGaAs quantum dot. *Phys. Rev. Lett.* **108**, 197403 (2012).
- [42] Latta, C. *et al.* Confluence of resonant laser excitation and bidirectional quantum-dot nuclear-spin polarization. *Nat. Phys.* **5**, 758–763 (2009).
- [43] Lodahl, P., Mahmoodian, S. & Stobbe, S. Interfacing single photons and single quantum dots with photonic nanostructures. *Rev. Mod. Phys.* **87**, 347–400 (2015).
- [44] Schöll, E. *et al.* Resonance fluorescence of GaAs quantum dots with near-unity photon indistinguishability. *Nano Lett.* **19**, 2404–2410 (2019).
- [45] Zhai, L. & Javadi, A. Harmonizing single photons with a laser pulse. *Nat. Nanotechnol.* **17**, 436–437 (2022).
- [46] Rastelli, A. *et al.* Hierarchical self-assembly of GaAs/AlGaAs quantum dots. *Phys. Rev. Lett.* **92**, 166104 (2004).
- [47] Atkinson, P., Zallo, E. & Schmidt, O. G. Independent wavelength and density control of uniform GaAs/AlGaAs quantum dots grown by infilling self-assembled nanoholes. *J. Appl. Phys.* **112**, 054303 (2012).
- [48] Jahn, J.-P. *et al.* An artificial rb atom in a semiconductor with lifetime-limited linewidth. *Phys. Rev. B* **92**, 245439 (2015).
- [49] Basso Basset, F. *et al.* Entanglement swapping with photons generated on demand by a quantum dot. *Phys. Rev. Lett.* **123**, 160501 (2019).
- [50] Béguin, L. *et al.* On-demand semiconductor source of 780-nm single photons with controlled temporal wave packets. *Phys. Rev. B* **97**, 205304 (2018).
- [51] Akopian, N., Wang, L., Rastelli, A., Schmidt, O. G. & Zwiller, V. Hybrid semiconductor-atomic interface: slowing down single photons from a quantum dot. *Nat. Photonics* **5**, 230–233 (2011).
- [52] Wolters, J. *et al.* Simple atomic quantum memory suitable for semiconductor quantum dot single photons. *Phys. Rev. Lett.* **119**, 060502 (2017).

- [53] Patel, R. B. *et al.* Two-photon interference of the emission from electrically tunable remote quantum dots. *Nat. Photonics* **4**, 632 (2010).
- [54] Warburton, R. J. *et al.* Optical emission from a charge-tunable quantum ring. *Nature* **405**, 926–929 (2000).
- [55] Bouet, L. *et al.* Charge tuning in [111] grown GaAs droplet quantum dots. *Appl. Phys. Lett.* **105**, 082111 (2014).
- [56] Langer, F., Plischke, D., Kamp, M. & Höfling, S. Single photon emission of a charge-tunable GaAs/Al_{0.25}Ga_{0.75}As droplet quantum dot device. *Appl. Phys. Lett.* **105**, 081111 (2014).
- [57] Seidl, S. *et al.* Effect of uniaxial stress on excitons in a self-assembled quantum dot. *Appl. Phys. Lett.* **88**, 203113 (2006).
- [58] Zhang, J. *et al.* Single photons on-demand from light-hole excitons in strain-engineered quantum dots. *Nano Lett.* **15**, 422–427 (2014).
- [59] Zhang, J. *et al.* High yield and ultrafast sources of electrically triggered entangled-photon pairs based on strain-tunable quantum dots. *Nat. Commun.* **6**, 10067 (2015).
- [60] Martín-Sánchez, J. *et al.* Reversible control of in-plane elastic stress tensor in nanomembranes. *Adv. Opt. Mater.* **4**, 682–687 (2016).
- [61] Trotta, R. *et al.* Wavelength-tunable sources of entangled photons interfaced with atomic vapours. *Nat. Commun.* **7**, 10375 (2016).
- [62] Yuan, X. *et al.* Uniaxial stress flips the natural quantization axis of a quantum dot for integrated quantum photonics. *Nat. Commun.* **9**, 3058 (2018).
- [63] Kumar, S. *et al.* Strain-induced tuning of the emission wavelength of high quality GaAs/AlGaAs quantum dots in the spectral range of the ⁸⁷Rb D₂ lines. *Appl. Phys. Lett.* **99**, 161118 (2011).
- [64] Grim, J. Q. *et al.* Scalable in operando strain tuning in nanophotonic waveguides enabling three-quantum-dot superradiance. *Nat. Materials* **18**, 963–969 (2019).
- [65] Moczala-Dusanowska, M. *et al.* Strain-tunable single-photon source based on a quantum dot–micropillar system. *ACS Photonics* **6**, 2025–2031 (2019).

- [66] Tumanov, D. *et al.* Static strain tuning of quantum dots embedded in a photonic wire. *Appl. Phys. Lett.* **112**, 123102 (2018).
- [67] Wang, H. *et al.* Near-Transform-limited single photons from an efficient solid-state quantum emitter. *Phys. Rev. Lett.* **116**, 213601 (2016).
- [68] Thoma, A. *et al.* Exploring dephasing of a solid-state quantum emitter via time- and temperature-dependent Hong-Ou-Mandel experiments. *Phys. Rev. Lett.* **116**, 033601 (2016).
- [69] Pedersen, F. T. *et al.* Near transform-limited quantum dot linewidths in a broadband photonic crystal waveguide. *ACS Photonics* **7**, 2343–2349 (2020).
- [70] Kuhlmann, A. V. *et al.* Transform-limited single photons from a single quantum dot. *Nat. Commun.* **6**, 8204 (2015).
- [71] Babin, H. G. *et al.* Charge tunable GaAs quantum dots in a photonic n-i-p diode. *Nanomaterials* **11** (2021).
- [72] Zhai, L. *et al.* Large-range frequency tuning of a narrow-linewidth quantum emitter. *Appl. Phys. Lett.* **117**, 083106 (2020).
- [73] Wang, Z. M., Liang, B. L., Sablon, K. A. & Salamo, G. J. Nanoholes fabricated by self-assembled gallium nanodrill on GaAs(100). *Appl. Phys. Lett.* **90**, 113120 (2007).
- [74] Hicks, C. W., Barber, M. E., Edkins, S. D., Brodsky, D. O. & Mackenzie, A. P. Piezoelectric-based apparatus for strain tuning. *Rev. Sci. Instr.* **85**, 065003 (2014).
- [75] Kuhlmann, A. V. *et al.* A dark-field microscope for background-free detection of resonance fluorescence from single semiconductor quantum dots operating in a set-and-forget mode. *Rev. Sci. Instrum.* **84**, 073905 (2013).
- [76] Nguyen, H. S. *et al.* Optically gated resonant emission of single quantum dots. *Phys. Rev. Lett.* **108**, 057401 (2012).
- [77] Testelin, C., Bernardot, F., Eble, B. & Chamarro, M. Hole–spin dephasing time associated with hyperfine interaction in quantum dots. *Phys. Rev. B* **79**, 195440 (2009).
- [78] Van de Walle, C. G. Band lineups and deformation potentials in the model-solid theory. *Phys. Rev. B* **39**, 1871–1883 (1989).

- [79] Das, S. *et al.* A wave-function ansatz method for calculating field correlations and its application to the study of spectral filtering and quantum dynamics of multi-emitter systems. *arXiv:1912.08303* (2019).
- [80] Ding, X. *et al.* On-demand single photons with high extraction efficiency and near-unity indistinguishability from a resonantly driven quantum dot in a micropillar. *Phys. Rev. Lett.* **116**, 020401 (2016).
- [81] Liu, J. *et al.* A solid-state source of strongly entangled photon pairs with high brightness and indistinguishability. *Nat. Nanotechnol.* **14**, 586–593 (2019).
- [82] Gao, W. B., Fallahi, P., Togan, E., Miguel-Sanchez, J. & Imamoglu, A. Observation of entanglement between a quantum dot spin and a single photon. *Nature* **491**, 426–430 (2012).
- [83] Sangouard, N., Simon, C., de Riedmatten, H. & Gisin, N. Quantum repeaters based on atomic ensembles and linear optics. *Rev. Mod. Phys.* **83**, 33–80 (2011).
- [84] Basso Basset, F. *et al.* High-yield fabrication of entangled photon emitters for hybrid quantum networking using high-temperature droplet epitaxy. *Nano Lett.* **18**, 505–512 (2018).
- [85] Plumhof, J. D. *et al.* Experimental investigation and modeling of the fine structure splitting of neutral excitons in strain-free GaAs/Al_xGa_{1-x}As quantum dots. *Phys. Rev. B* **81**, 121309(R) (2010).
- [86] Ha, N. *et al.* Size-dependent line broadening in the emission spectra of single GaAs quantum dots: Impact of surface charge on spectral diffusion. *Phys. Rev. B* **92**, 075306 (2015).
- [87] Ulhaq, A. *et al.* Vanishing electron *g* factor and long-lived nuclear spin polarization in weakly strained nanohole-filled GaAs/AlGaAs quantum dots. *Phys. Rev. B* **93**, 165306 (2016).
- [88] Gangloff, D. *et al.* Quantum interface of an electron and a nuclear ensemble. *Science* **364**, 62–66 (2019).
- [89] Shulman, M. D. *et al.* Suppressing qubit dephasing using real-time hamiltonian estimation. *Nat. Commun.* **5**, 5156 (2014).
- [90] Schwartz, I. *et al.* Deterministic generation of a cluster state of entangled photons. *Science* **354**, 434–437 (2016).

- [91] Mooney, P. M. Deep donor levels (DX centers) in III-V semiconductors. *J. Appl. Phys* **67**, R1–R26 (1990).
- [92] Munoz, E. *et al.* Techniques to minimize DX center deleterious effects in III-V device performance. *J. Appl. Phys.* **73**, 4988–4997 (1993).
- [93] MacLeod, S. J. *et al.* Hybrid architecture for shallow accumulation mode Al-GaAs/GaAs heterostructures with epitaxial gates. *Appl. Phys. Lett.* **106**, 012105 (2015).
- [94] Böckler, C. *et al.* Electrically driven high-Q quantum dot-micropillar cavities. *Appl. Phys. Lett.* **92**, 091107 (2008).
- [95] Kiršanskė, G. *et al.* Indistinguishable and efficient single photons from a quantum dot in a planar nanobeam waveguide. *Phys. Rev. B* **96**, 165306 (2017).
- [96] Fry, P. W. *et al.* Inverted electron-hole alignment in InAs-GaAs self-assembled quantum dots. *Phys. Rev. Lett.* **84**, 733–736 (2000).
- [97] Madsen, K. H. *et al.* Measuring the effective phonon density of states of a quantum dot in cavity quantum electrodynamics. *Phys. Rev. B* **88**, 045316 (2013).
- [98] Kuhlmann, A. V. *et al.* Charge noise and spin noise in a semiconductor quantum device. *Nat. Phys.* **9**, 570–575 (2013).
- [99] Smith, J. M. *et al.* Voltage control of the spin dynamics of an exciton in a semiconductor quantum dot. *Phys. Rev. Lett.* **94**, 197402 (2005).
- [100] Matthiesen, C., Vamivakas, A. N. & Atatüre, M. Subnatural linewidth single photons from a quantum dot. *Phys. Rev. Lett.* **108**, 093602 (2012).
- [101] Lu, C.-Y. *et al.* Direct measurement of spin dynamics in InAs/GaAs quantum dots using time-resolved resonance fluorescence. *Phys. Rev. B* **81**, 035332 (2010).
- [102] Najer, D. *et al.* A gated quantum dot far in the strong-coupling regime of cavity-QED at optical frequencies. *Nature* **575**, 622–627 (2019).
- [103] Atatüre, M. *et al.* Quantum-dot spin-state preparation with near-unity fidelity. *Science* **312**, 551–553 (2006).
- [104] Javadi, A. *et al.* Spin–photon interface and spin-controlled photon switching in a nanobeam waveguide. *Nat. Nanotechnol.* **13**, 398 (2018).

- [105] Ludwig, A. *et al.* Ultra-low charge and spin noise in self-assembled quantum dots. *J. Cryst. Growth* **477**, 193–196 (2017).
- [106] Warburton, R. J. *et al.* Giant permanent dipole moments of excitons in semiconductor nanostructures. *Phys. Rev. B* **65**, 113303 (2002).
- [107] Loudon, R. *The quantum theory of light* (OUP Oxford, 2000).
- [108] Johansson, J. R., Nation, P. D. & Nori, F. Qutip 2: A python framework for the dynamics of open quantum systems. *Comput. Phys. Commun.* **184**, 1234–1240 (2013).
- [109] Flagg, E. B. *et al.* Resonantly driven coherent oscillations in a solid-state quantum emitter. *Nat. Phys.* **5**, 203 (2009).
- [110] Rezai, M., Wrachtrup, J. & Gerhardt, I. Detuning dependent Rabi oscillations of a single molecule. *New J. Phys.* **21**, 045005 (2019).
- [111] Dreiser, J. *et al.* Optical investigations of quantum dot spin dynamics as a function of external electric and magnetic fields. *Phys. Rev. B* **77**, 075317 (2008).
- [112] Bambynek, W. *et al.* X-ray fluorescence yields, Auger, and Coster-Kronig transition probabilities. *Rev. Mod. Phys.* **44**, 716–813 (1972).
- [113] Efros, A. L. & Rosen, M. Random telegraph signal in the photoluminescence intensity of a single quantum dot. *Phys. Rev. Lett.* **78**, 1110–1113 (1997).
- [114] Kurzmann, A., Ludwig, A., Wieck, A. D., Lorke, A. & Geller, M. Auger recombination in self-assembled quantum dots: Quenching and broadening of the charged exciton transition. *Nano Lett.* **16**, 3367–3372 (2016).
- [115] Vaxenburg, R., Lifshitz, E. & Efros, A. L. Suppression of Auger-stimulated efficiency droop in nitride-based light emitting diodes. *Appl. Phys. Lett.* **102**, 031120 (2013).
- [116] Bloch, F. Double electron transitions in X-ray spectra. *Phys. Rev.* **48**, 187 (1935).
- [117] Hawrylak, P. Resonant magnetoexcitons and the fermi-edge singularity in a magnetic field. *Phys. Rev. B* **44**, 11236–11240 (1991).
- [118] Llusar, J. & Climente, J. I. Nature and control of shakeup processes in colloidal nanoplatelets. *ACS Photonics* **7**, 3086–3095 (2020).

- [119] Åberg, T. & Utriainen, J. Evidence for a "radiative Auger effect" in X-ray photon emission. *Phys. Rev. Lett.* **22**, 1346–1348 (1969).
- [120] Dean, P. J., Cuthbert, J. D., Thomas, D. G. & Lynch, R. T. Two-electron transitions in the luminescence of excitons bound to neutral donors in gallium phosphide. *Phys. Rev. Lett.* **18**, 122–124 (1967).
- [121] Antolinez, F. V., Rabouw, F. T., Rossinelli, A. A., Cui, J. & Norris, D. J. Observation of electron shakeup in CdSe/CdS core/shell nanoplatelets. *Nano Lett.* **19**, 8495–8502 (2019).
- [122] Gawarecki, K. *et al.* Structural symmetry-breaking to explain radiative Auger transitions in self-assembled quantum dots (2022). arXiv:2208.12069.
- [123] Nash, K. J., Skolnick, M. S., Saker, M. K. & Bass, S. J. Many body shakeup in quantum well luminescence spectra. *Phys. Rev. Lett.* **70**, 3115–3118 (1993).
- [124] Skolnick, M. S. *et al.* Fermi sea shake-up in quantum well luminescence spectra. *Solid-State Electron.* **37**, 825–829 (1994).
- [125] Finkelstein, G., Shtrikman, H. & Bar-Joseph, I. Mechanism of shakeup processes in the photoluminescence of a two-dimensional electron gas at high magnetic fields. *Phys. Rev. B* **56**, 10326–10331 (1997).
- [126] Manfra, M. J., Goldberg, B. B., Pfeiffer, L. & West, K. Anderson-Fano resonance and shake-up processes in the magnetophotoluminescence of a two-dimensional electron system. *Phys. Rev. B* **57**, R9467–R9470 (1998).
- [127] Bryja, L. *et al.* Magneto-optical probing of weak disorder in a two-dimensional hole gas. *Phys. Rev. B* **75**, 035308 (2007).
- [128] Muller, A. *et al.* Resonance fluorescence from a coherently driven semiconductor quantum dot in a cavity. *Phys. Rev. Lett.* **99**, 187402 (2007).
- [129] Zibik, E. *et al.* Long lifetimes of quantum-dot intersublevel transitions in the terahertz range. *Nat. Mater.* **8**, 803–807 (2009).
- [130] Weis, S. *et al.* Optomechanically induced transparency. *Science* **330**, 1520–1523 (2010).
- [131] Safavi-Naeini, A. H. *et al.* Electromagnetically induced transparency and slow light with optomechanics. *Nature* **472**, 69–73 (2011).

- [132] Ulhaq, A. *et al.* Cascaded single-photon emission from the Mollow triplet sidebands of a quantum dot. *Nat. Photonics* **6**, 238–242 (2012).
- [133] Xu, X. *et al.* Coherent optical spectroscopy of a strongly driven quantum dot. *Science* **317**, 929–932 (2007).
- [134] Ramsay, A. J. *et al.* Phonon-induced Rabi-frequency renormalization of optically driven single InGaAs/GaAs quantum dots. *Phys. Rev. Lett.* **105**, 177402 (2010).
- [135] Fleischhauer, M., Imamoglu, A. & Marangos, J. P. Electromagnetically induced transparency: Optics in coherent media. *Rev. Mod. Phys.* **77**, 633–673 (2005).
- [136] Prechtel, J. H. *et al.* Decoupling a hole spin qubit from the nuclear spins. *Nat. Mater.* **15**, 981–986 (2016).
- [137] Press, D., Ladd, T. D., Zhang, B. & Yamamoto, Y. Complete quantum control of a single quantum dot spin using ultrafast optical pulses. *Nature* **456**, 218–221 (2008).
- [138] Barfuss, A. *et al.* Phase-controlled coherent dynamics of a single spin under closed-contour interaction. *Nat. Phys.* **14**, 1087–1091 (2018).
- [139] Chekhovich, E. A., da Silva, S. F. C. & Rastelli, A. Nuclear spin quantum register in an optically active semiconductor quantum dot. *Nat. Nanotechnol.* **15**, 999–1004 (2020).
- [140] Javadi, A. *et al.* Spin–photon interface and spin-controlled photon switching in a nanobeam waveguide. *Nat. Nanotechnol.* **13**, 398–403 (2018).
- [141] Yang, W. & Sham, L. J. Collective nuclear stabilization in single quantum dots by noncollinear hyperfine interaction. *Phys. Rev. B* **85**, 235319 (2012).
- [142] Xu, X. *et al.* Coherent population trapping of an electron spin in a single negatively charged quantum dot. *Nat. Phys.* **4**, 692–695 (2008).
- [143] Issler, M. *et al.* Nuclear spin cooling using overhauser-field selective coherent population trapping. *Phys. Rev. Lett.* **105** (2010).
- [144] Houel, J. *et al.* High resolution coherent population trapping on a single hole spin in a semiconductor quantum dot. *Phys. Rev. Lett.* **112** (2014).

- [145] Nutz, T., Barnes, E. & Economou, S. E. Solvable quantum model of dynamic nuclear polarization in optically driven quantum dots. *Phys. Rev. B* **99**, 035439 (2019).
- [146] Qiang, X. *et al.* Large-scale silicon quantum photonics implementing arbitrary two-qubit processing. *Nat. Photonics* **12**, 534–539 (2018).
- [147] Strauf, S. *et al.* High-frequency single-photon source with polarization control. *Nat. Photonics* **1**, 704–708 (2007).
- [148] Uppu, R., Midolo, L., Zhou, X., Carolan, J. & Lodahl, P. Quantum-dot-based deterministic photon–emitter interfaces for scalable photonic quantum technology. *Nat. Nanotechnol.* **16**, 1308–1317 (2021).
- [149] Reindl, M. *et al.* Phonon-assisted two-photon interference from remote quantum emitters. *Nano Lett.* **17**, 4090–4095 (2017).
- [150] Weber, J. H. *et al.* Two-photon interference in the telecom C-band after frequency conversion of photons from remote quantum emitters. *Nat. Nanotechnol.* **14**, 23–26 (2018).
- [151] Llewellyn, D. *et al.* Chip-to-chip quantum teleportation and multi-photon entanglement in silicon. *Nat. Phys.* **16**, 148–153 (2020).
- [152] Basset, F. B. *et al.* Quantum key distribution with entangled photons generated on demand by a quantum dot. *Sci. Adv.* **7**, eabe6379 (2021).
- [153] Kołodyński, J. *et al.* Device-independent quantum key distribution with single-photon sources. *Quantum* **4**, 260 (2020).
- [154] He, Y. *et al.* Indistinguishable tunable single photons emitted by spin-flip raman transitions in InGaAs quantum dots. *Phys. Rev. Lett.* **111**, 237403 (2013).
- [155] Giesz, V. *et al.* Cavity-enhanced two-photon interference using remote quantum dot sources. *Phys. Rev. B* **92**, 161302 (2015).
- [156] Zopf, M. *et al.* Frequency feedback for two-photon interference from separate quantum dots. *Phys. Rev. B* **98**, 161302 (2018).
- [157] You, X. *et al.* Quantum interference between independent solid-state single-photon sources separated by 300 km fiber (2021). arXiv:[2106.15545](https://arxiv.org/abs/2106.15545).

- [158] Santori, C., Fattal, D., Vučković, J., Solomon, G. S. & Yamamoto, Y. Indistinguishable photons from a single-photon device. *Nature* **419**, 594–597 (2002).
- [159] Maunz, P. *et al.* Quantum interference of photon pairs from two remote trapped atomic ions. *Nat. Phys.* **3**, 538–541 (2007).
- [160] Stephenson, L. J. *et al.* High-rate, high-fidelity entanglement of qubits across an elementary quantum network. *Phys. Rev. Lett.* **124**, 110501 (2020).
- [161] Beugnon, J. *et al.* Quantum interference between two single photons emitted by independently trapped atoms. *Nature* **440**, 779–782 (2006).
- [162] Bernien, H. *et al.* Heralded entanglement between solid-state qubits separated by three metres. *Nature* **497**, 86–90 (2013).
- [163] Humphreys, P. C. *et al.* Deterministic delivery of remote entanglement on a quantum network. *Nature* **558**, 268–273 (2018).
- [164] Kambs, B. & Becher, C. Limitations on the indistinguishability of photons from remote solid state sources. *New J. Phys.* **20**, 115003 (2018).
- [165] Kiesel, N., Schmid, C., Weber, U., Ursin, R. & Weinfurter, H. Linear optics controlled-phase gate made simple. *Phys. Rev. Lett.* **95**, 210505 (2005).
- [166] James, D. F. V., Kwiat, P. G., Munro, W. J. & White, A. G. Measurement of qubits. *Phys. Rev. A* **64**, 052312 (2001).
- [167] Istrati, D. *et al.* Sequential generation of linear cluster states from a single photon emitter. *Nat. Commun.* **11** (2020).
- [168] Cogan, D., Su, Z.-E., Kenneth, O. & Gershoni, D. A deterministic source of indistinguishable photons in a cluster state. arXiv:[2110.05908](https://arxiv.org/abs/2110.05908)(2021).
- [169] Fischer, K. A. *et al.* Signatures of two-photon pulses from a quantum two-level system. *Nat. Phys.* **13**, 649–654 (2017).
- [170] Schimpf, C., Manna, S., Da Silva, S. F. C., Aigner, M. & Rastelli, A. Entanglement-based quantum key distribution with a blinking-free quantum dot operated at a temperature up to 20 k. *Adv. Photonics* **3**, 065001 (2021).
- [171] Legero, T., Wilk, T., Kuhn, A. & Rempe, G. Time-resolved two-photon quantum interference. *Appl. Phys. B* **77**, 797 (2003).

- [172] Sun, Z., Delteil, A., Faelt, S. & Imamoglu, A. Measurement of spin coherence using Raman scattering. *Phys. Rev. B* **93**, 241302 (2016).
- [173] Abrarov, S. & Quine, B. Efficient algorithmic implementation of the Voigt/complex error function based on exponential series approximation. *Appl. Math. Comput.* **218**, 1894–1902 (2011).
- [174] Flågan, S., Maletinsky, P., Warburton, R. J. & Riedel, D. Microcavity platform for widely tunable optical double resonance. *Optica* **9**, 1197 (2022).
- [175] Crespi, A. *et al.* Integrated photonic quantum gates for polarization qubits. *Nat. Commun.* **2**, 1 (2011).
- [176] Langford, N. K. *et al.* Demonstration of a simple entangling optical gate and its use in Bell-state analysis. *Phys. Rev. Lett.* **95**, 210504 (2005).
- [177] Kiesel, N. *Experiments on multiphoton entanglement*. Ph.D. thesis, Ludwig Maximilian University of Munich (2007).
- [178] Li, J.-P. *et al.* Heralded nondestructive quantum entangling gate with single-photon sources. *Phys. Rev. Lett.* **126**, 140501 (2021).
- [179] Hofmann, H. F. Complementary classical fidelities as an efficient criterion for the evaluation of experimentally realized quantum operations. *Phys. Rev. Lett.* **94**, 160504 (2005).
- [180] Altepeter, J., Jeffrey, E. & Kwiat, P. Photonic state tomography. *Advances In Atomic, Molecular, and Optical Physics*, 105–159 (Academic Press, 2005).
- [181] Adcock, J. C., Vigliar, C., Santagati, R., Silverstone, J. W. & Thompson, M. G. Programmable four-photon graph states on a silicon chip. *Nat. Commun.* **10**, 3528 (2019).